

2007

# Outlet Glacier Dynamics in East Greenland and East Antarctica

Leigh Asher Stearns

Follow this and additional works at: <http://digitalcommons.library.umaine.edu/etd>



Part of the [Glaciology Commons](#)

---

## Recommended Citation

Stearns, Leigh Asher, "Outlet Glacier Dynamics in East Greenland and East Antarctica" (2007). *Electronic Theses and Dissertations*. 104.  
<http://digitalcommons.library.umaine.edu/etd/104>

---

This Open-Access Dissertation is brought to you for free and open access by DigitalCommons@UMaine. It has been accepted for inclusion in Electronic Theses and Dissertations by an authorized administrator of DigitalCommons@UMaine.

**OUTLET GLACIER DYNAMICS IN EAST GREENLAND AND EAST  
ANTARCTICA**

By

Leigh Asher Stearns

B.A. Carleton College, 1999

M.S. Geological Sciences, The Ohio State University, 2002

**A THESIS**

Submitted in Partial Fulfillment of the

Requirements for the Degree of

Doctor of Philosophy

(in Earth Sciences)

The Graduate School

The University of Maine

December, 2007

**Advisory Committee:**

Gordon S. Hamilton, Associate Professor, Climate Change Institute, Advisor

Roger LeB. Hooke, Professor, Department of Earth Sciences

Peter O. Koons, Professor, Department of Earth Sciences

Paul A. Mayewski, Director, Climate Change Institute

Theodore A. Scambos, Senior Researcher, National Snow and Ice Data Center

© 2007 Leigh Asher Stearns  
All Rights Reserved

## **LIBRARY RIGHTS STATEMENT**

In presenting this thesis in partial fulfillment of the requirements for an advanced degree at The University of Maine, I agree that the Library shall make it freely available for inspection. I further agree that permission for "fair use" copying of this thesis for scholarly purposes may be granted by the Librarian. It is understood that any copying or publication of this thesis for financial gain shall not be allowed without my written permission.

Signature:

Date:

# **OUTLET GLACIER DYNAMICS IN EAST GREENLAND AND EAST ANTARCTICA**

By Leigh Asher Stearns

Thesis Advisor: Dr G. S. Hamilton

An Abstract of the Thesis Presented  
in Partial Fulfillment of the Requirements for the  
Degree of Doctor of Philosophy  
(in Earth Sciences)  
December, 2007

Ice mass from the interior of Greenland and Antarctica is transported to the ocean by numerous large, fast-flowing outlet glaciers. Changes in the flow configuration of these outlet glaciers modulate ice sheet mass balance and sea level. Several recent studies have highlighted rapid increases in glacier speed in both Greenland and Antarctica, implying that the near-term contribution to sea level from ice sheets is under-estimated by current models. Here, the mass balance and force budget of several large outlet glaciers in East Greenland and East Antarctica are investigated using remote-sensing and field-based measurements.

Recent estimates show that Greenland's contribution to sea level more than doubled in the past decade, and that the majority of this additional mass loss is due to changes in the dynamics of a few large outlet glaciers. Our measurements indicate that up to ~10% of global sea level rise over the period 2001 – 2006 was contributed by just two glaciers, Helheim and Kangerdlugssuaq, in Southeast Greenland. We also find a latitudinal pattern of glacier behavior in East Greenland, where large and rapid changes are taking place south of 70°N while glaciers north of 70°N are stable.

The East Antarctic Ice Sheet is Earth's largest source of freshwater and has the potential to raise sea level by 57 m. The dynamics of outlet glaciers draining the ice sheet

through the Transantarctic Mountains are largely unknown, but the glaciers are often assumed to be stable. In this study we investigate the dynamics of four large East Antarctic outlet glaciers. Together, these glaciers drain  $\sim 1,500,000$  km $^2$ , or 12% by area of the entire Antarctic Ice Sheet. Mass balance calculations show modest imbalances for some glaciers, and a large imbalance for Byrd Glacier. Observations indicate a possible recent increase in flow speed, but this is insufficient to explain the large imbalance. We argue that catchment-wide estimates of accumulation rate contain large errors.

This research provides new insights into the dynamic character of ice sheet outlet glaciers. In addition to quantifying recent changes, it also provides baseline data against which future behavior can be assessed.

## **ACKNOWLEDGEMENTS**

My graduate research has been funded through Dr. Hamilton's NASA grant NNG04-GK39G (2002–2004), a NSF GK-12 teaching fellowship (2004–2005), and a NASA Earth Systems Science Fellowship (NNG05-GQ3H) (2005–2007). Acknowledgements for each chapter are detailed below.

### **Chapter 2: A Comparison of High-Rate GPS and Satellite Remote Sensing Measurements on Helheim Glacier, East Greenland**

Field data collection and processing was completed with Jim Davis, Pedro Elósegui, Morten Langer, and Meredith Nettles. Funding for field logistics was provided by NASA (NNG04-GK39G to GSH), the Gary Comer Science and Education Foundation (awarded to MN), the Spanish Ministry of Education and Science (PE), and the Dan and Betty Churchill Exploration Fund (awarded to LAS).

### **Chapter 3: Recent Dynamics of Four Large East Antarctic Outlet Glaciers**

This work was supported by NASA's Cryospheric Sciences Program through NNG04-GK39G (GSH), and NASA's Earth Systems Science Fellowship (LAS). We would like to thank Charles Swithinbank for providing raw data and maps from his 1961 Antarctic field season. Baerbel Lucchitta and Terry Hughes provided us with Landsat TM4 scenes of Byrd Glacier. Willem van de Berg generously shared his modeled surface mass balance data with us for this study.

## **Chapter 4: Multi-Decadal Record of Ice Dynamics on Daugaard Jensen Glacier, East Greenland, from Satellite Imagery and Terrestrial Measurements**

Radar data used in this study was obtained through the University of Kansas (<https://www.cresis.ku.edu/research/data/>). The digital elevation model was supplied by the US National Snow and Ice Data Center <http://nsidc.org/data/nsidc-0092.html>. This work was funded by NASA's Cryospheric Sciences program through NNG04-GK39G to GSH. Niels Reeh was a co-author on this paper.

## **Chapter 5: Rapid Volume Loss from Two East Greenland Outlet Glaciers Quantified using Repeat Stereo Satellite Imagery**

We thank Etienne Berthier and two anonymous reviewers for comments which improved this paper. Data analysis was supported by a NASA Earth Systems Science Graduate Fellowship (to LAS) and NNG04-GK39G from NASA's Cryospheric Sciences Program (to GSH).

I am indebted to the multitude of advisors and mentors that have encouraged and supported me over the years. During my Master's degree at The Ohio State University, Ian Whillans and Kees van der Veen answered my novice questions with thought-provoking answers, patience, and good humor. Gordon Hamilton, my mentor throughout the 7 years of my graduate career, has become a great friend and field companion. It is always terrific to work with someone who loves his job. I am grateful to all my committee members for their encouragement, and for posing interesting, and difficult, questions about my research. I have been similarly blessed with helpful, diligent, fun, and incredibly smart office-mates and fellow graduate students.

## TABLE OF CONTENTS

<b>ACKNOWLEDGEMENTS .....</b>	iii
<b>LIST OF TABLES .....</b>	x
<b>LIST OF FIGURES .....</b>	xi

## Chapter

<b>1</b>	<b>INTRODUCTION . . . . .</b>	<b>1</b>
1.1	Ice Sheets and Sea Level Rise . . . . .	1
1.2	Glacier Dynamics . . . . .	4
1.2.1	Tidewater Glacier Dynamics . . . . .	4
1.2.2	Ice Shelf Buttressing of Glacier Flow . . . . .	6
1.3	Dissertation Aims and Objectives . . . . .	7
1.4	Dissertation Outline . . . . .	8
1.4.1	Chapter 2: A Comparison of High-Rate GPS and Satellite Remote Sensing Measurements on Helheim Glacier, East Greenland . .	8
1.4.2	Chapter 3: Recent Dynamics of Four Large East Antarctic Outlet Glaciers . . . . .	8
1.4.3	Chapter 4: Multi-Decadal Record of Ice Dynamics on Daugaard Jensen Glacier, East Greenland, from Satellite Imagery and Terrestrial Measurements . . . . .	8
1.4.4	Chapter 5: Rapid Volume Loss from Two East Greenland Outlet Glaciers Quantified using Repeat Stereo Satellite Imagery . . . . .	9
1.4.5	Chapter 6: Concluding Remarks . . . . .	9

<b>2 A COMPARISON OF HIGH-RATE GPS AND SATELLITE REMOTE SENSING MEASUREMENTS ON HELHEIM GLACIER, EAST GREENLAND . . . . .</b>	10
2.1 Introduction . . . . .	10
2.2 Data . . . . .	12
2.2.1 Ground-based GPS surveys . . . . .	12
2.2.2 Satellite Remote Sensing . . . . .	12
2.2.2.1 ASTER-derived DEMs . . . . .	14
2.2.2.2 ASTER-derived Velocity Data . . . . .	16
2.3 Results . . . . .	18
2.3.1 Elevation . . . . .	18
2.3.2 Velocity . . . . .	20
2.4 Discussion and Conclusion . . . . .	22
<b>3 RECENT DYNAMICS OF FOUR LARGE EAST ANTARCTIC OUTLET GLACIERS . . . . .</b>	24
3.1 Introduction . . . . .	24
3.2 Data . . . . .	25
3.2.1 Velocity . . . . .	25
3.2.2 Elevation Data . . . . .	26
3.2.3 Bed Topography . . . . .	27
3.2.4 Accumulation Rates . . . . .	28
3.3 Spatial and Temporal Changes in Ice Velocity and Surface Elevation . . . . .	28
3.3.1 David Glacier . . . . .	29
3.3.2 Mulock Glacier . . . . .	32
3.3.3 Byrd Glacier . . . . .	35

3.3.4	Nimrod Glacier .....	38
3.4	Force Budget .....	41
3.4.1	Theory .....	41
3.4.2	Application .....	43
3.4.3	Errors .....	44
3.5	Spatial and Temporal Changes in Force Balance .....	45
3.5.1	David Glacier .....	45
3.5.2	Mulock Glacier .....	46
3.5.3	Byrd Glacier .....	49
3.5.4	Nimrod Glacier .....	53
3.5.5	Discussion .....	55
3.6	Mass Balance .....	56
3.6.1	Application .....	56
3.6.2	Results .....	57
3.6.3	Discussion .....	57
3.7	Conclusions .....	60
<b>4</b>	<b>MULTI-DECadal RECORD OF ICE DYNAMICS ON DAUGAARD JENSEN GLACIER, EAST GREENLAND, FROM SATELLITE IMAGERY AND TER- RESTRIAL MEASUREMENTS .....</b>	<b>61</b>
4.1	Introduction .....	61
4.2	Data .....	63
4.2.1	Calving Front Positions: 1950 – 2007 .....	63
4.2.2	Glacier Velocities: 1968 – 2005 .....	64
4.3	Estimating Mass Balance .....	68

4.4	Force Balance Distribution .....	70
4.5	Discussion .....	73
4.6	Conclusions .....	74
<b>5</b>	<b>RAPID VOLUME LOSS FROM TWO EAST GREENLAND OUTLET GLACIERS QUANTIFIED USING REPEAT STEREO SATELLITE IMAGERY .....</b>	<b>76</b>
5.1	Introduction .....	76
5.2	Data .....	76
5.2.1	Calving Front Position .....	76
5.2.2	Ice Velocity .....	77
5.2.2.1	Ground-based GPS Surveys .....	77
5.2.2.2	Feature Tracking .....	78
5.2.3	DEM Extraction Method and Errors .....	79
5.3	Observed Changes .....	80
5.3.1	Calving Front .....	80
5.3.2	Ice Velocity .....	81
5.3.3	Surface Elevation .....	83
5.3.4	Volume Change .....	85
5.4	Interpretation .....	88
5.5	Conclusion .....	90
<b>6</b>	<b>CONCLUSIONS .....</b>	<b>92</b>
6.1	Summary .....	92
6.2	Implications and Recommendations for Future Work .....	94
	<b>REFERENCES .....</b>	<b>96</b>

**APPENDIX – SATELLITE IMAGE DETAILS .....** 108

**BIOGRAPHY OF THE AUTHOR .....** 113

## LIST OF TABLES

Table 2.1	Summary of errors for absolute and relative DEMs of different post-spacings. ....	20
Table 3.1	Velocity pairs used for the force balance study in section 3.5. ....	44
Table 3.2	Origin and rotation angles of glaciers used in the force balance analysis. ....	44
Table 3.3	1 $\sigma$ uncertainties for variables used in the force balance calculation. ....	45
Table 3.4	Mass balance results using accumulation estimates from <i>Van de Berg et al.</i> (2006). ....	57
Table 3.5	Catchment-wide accumulation rates derived from three surface mass balance compilations. ....	58
Table 4.1	Quantities used to estimate mass balance for Daugaard Jensen and Graah glaciers. ....	69
Table 5.1	Quantities used to solve equation 5.1. ....	89
Table A.1	Images used in Chapter 2. ....	109
Table A.2	Images used in Chapter 3. ....	110
Table A.3	Images used in Chapter 4. ....	111
Table A.4	Images used in Chapter 5. ....	112

## LIST OF FIGURES

Figure 2.1	A DEM of Helheim Glacier, derived from an ASTER image taken on August 30, 2006. ....	13
Figure 2.2	The acquisition of an ASTER stereo scene. ....	14
Figure 2.3	Two ASTER scenes of Helheim Glacier illustrating the IMCORR technique. ....	16
Figure 2.4	Elevation results from GPS and two ASTER-derived DEMS. ....	19
Figure 2.5	The influence of different IMCORR grid spacings on derived velocities. ....	21
Figure 2.6	Velocity results from GPS and ASTER-derived velocity measurements. ....	22
Figure 2.7	The velocity vectors of GPS (red) and ASTER-derived (black) data. ....	23
Figure 3.1	Catchment boundaries for East Antarctic outlet glaciers studied in this paper, overlaid on a portion of the Radarsat mosaic. ....	25
Figure 3.2	David Glacier: (A) satellite image, (B) surface topography, and (C) ice velocity. ....	30
Figure 3.3	David Glacier ice velocity and surface elevation changes. ....	31
Figure 3.4	Mulock Glacier: (A) satellite image, (B) surface topography, (C) ice thickness, and (D) ice velocity. ....	33
Figure 3.5	Mulock Glacier ice velocity and surface elevation changes. ....	34
Figure 3.6	Byrd Glacier: (A) satellite image, (B) surface topography, (C) ice thickness, and (D) ice velocity. ....	36
Figure 3.7	Byrd Glacier ice velocity and surface elevation changes. ....	37
Figure 3.8	Nimrod Glacier: (A) satellite image, (B) surface topography, (C) ice thickness, and (D) ice velocity. ....	39

Figure 3.9	Nimrod Glaciers ice velocity and surface elevation changes.....	40
Figure 3.10	David Glacier. Components of the force balance equation derived from 2001 velocities and plotted at 1 km spacing. ....	46
Figure 3.11	Mulock Glacier: Components of the force balance equation 3.6, gridded to 1 km.....	48
Figure 3.12	Byrd Glacier: Components of the force balance equation 3.6, grid- ded to 1 km.....	50
Figure 3.13	Individual forces for Byrd Glacier along an 80 km profile (flowing from left to right), for four velocity epochs.....	51
Figure 3.14	Calculated frictional melt rates ( $\text{m yr}^{-1}$ ) for Byrd Glacier, overlain with velocity contours (each contour = $100 \text{ m yr}^{-1}$ ). ....	53
Figure 3.15	Components of the force balance equation, along an 80 km profile (flowing from left to right) for Nimrod Glacier, using velocity data from 2001. ....	54
Figure 4.1	Map of the study area and nearby automatic weather stations from <i>Box (2002)</i> . ....	62
Figure 4.2	Terminus positions for Daugaard Jensen Glacier, Charcot Glacier, and Graah Glacier. ....	65
Figure 4.3	Contoured ice velocity for Daugaard Jensen Glacier from feature tracking and GPS measurements. ....	68
Figure 4.4	Contoured ice velocity for Charcot and Graah glaciers from feature tracking and GPS measurements. ....	69
Figure 4.5	Components of the force balance equation of Daugaard Jensen Glacier, gridded to 1 km. ....	71

Figure 4.6	Along-flow components of force balance, derived from 2003 velocities and plotted at 1 km spacing.....	72
Figure 5.1	Calving front positions for Kangerdlugssuaq Glacier and Helheim Glacier determined from aerial photographs and satellite imagery.....	81
Figure 5.2	Velocity results for Kangerdlugssuaq Glacier.....	82
Figure 5.3	Velocity results for Helheim Glacier.....	83
Figure 5.4	Elevation changes along Kangerdlugssuaq Glacier.....	85
Figure 5.5	Elevation changes along Helheim Glacier.....	86
Figure 5.6	Surface lowering over Kangerdlugssuaq and Helheim glaciers.....	87

# Chapter 1

## INTRODUCTION

### 1.1 Ice Sheets and Sea Level Rise

Sea level rise from enhanced ice sheet discharge is one of the largest and most immediate potential consequences of climate warming. Total collapse of the Greenland and Antarctic ice sheets would raise eustatic sea level by 63.9 m (*Bindoff et al.*, 2007). However, the societal and economic effects of even a modest rise in sea level would be disastrous, considering that 600 million people live in low elevation coastal zones, defined as being within 10 vertical meters of sea level (*McGranahan et al.*, 2007). Sea level rise over the last century, due to thermal expansion of the ocean, enhanced river discharge and diminishing glaciers, permafrost, and aquifers, was  $1.7 \pm 0.5 \text{ mm yr}^{-1}$  (*Bindoff et al.*, 2007). The rate of sea level rise increased to  $3.1 \pm 0.7 \text{ mm yr}^{-1}$  in the past decade (*Cazenave and Nerem*, 2004), and is projected to increase to  $\sim 4 \text{ mm yr}^{-1}$  by 2090 under current emissions scenarios (*Bindoff et al.*, 2007). Because ice sheets are the largest potential source of future sea level rise, there is great need to understand their dynamics in a changing climate.

Current sea level rise predictions are based solely on the balance between snow accumulation and surface/basal melting and do not include a dynamic response of outlet glaciers to climate warming (*Alley et al.*, 2005; *Bindoff et al.*, 2007). Until recently, conventional glaciological theory (e.g., *Alley and Whillans*, 1991) was that large ice sheets respond slowly (timescales of  $>10^3$  years) to changes in external forcings (such as temperature, precipitation and sea level). Recent observations of large climate-driven changes in ice sheet dynamics in parts of Greenland and Antarctica (e.g., *Joughin et al.*, 2003; *Rignot and Kanagaratnam*, 2006; *Scambos et al.*, 2004; *Shepherd et al.*, 2001) challenge this conventional wisdom and point to the need to include these effects in sea level predictions.

The Antarctic and Greenland ice sheets contain  $\sim 87\%$  of the earth's fresh water (*Van der Veen*, 1999). Mass is added to the ice sheets by precipitation, and lost by surface and basal melting, and iceberg calving. Recent studies report that Greenland lost between 93 – 227

Gt yr<sup>-1</sup> of ice in the past 5 years (*Chen et al.*, 2006; *Luthcke et al.*, 2006; *Ramillien et al.*, 2006; *Rignot and Kanagaratnam*, 2006; *Velicogna and Wahr*, 2006) which is more than twice the rate of loss during the previous decade (*Rignot and Kanagaratnam*, 2006). (For reference, 360 Gt is equivalent to 1 mm of global sea level rise.) The increased mass loss occurred predominantly in southeast Greenland, and is due to the acceleration of several large outlet glaciers between 2001 and 2005 (*Howat et al.*, 2005; *Rignot and Kanagaratnam*, 2006; *Stearns and Hamilton*, 2007). East Antarctic mass balance studies indicate  $-1$  to  $+67$  km<sup>3</sup> yr<sup>-1</sup> net change over the past decade (*Davis et al.*, 2005; *Ramillien et al.*, 2006; *Rignot and Thomas*, 2002; *Velicogna and Wahr*, 2006; *Wingham et al.*, 2006; *Zwally et al.*, 2005), with most of the growth being due to slightly increased precipitation at high elevations (*Davis et al.*, 2005). Large uncertainties are associated with most of the above mass balance estimates, which complicates the assessment of the sea level rise contribution from ice sheets. Moreover, rapid changes in the balance terms (*Rignot and Kanagaratnam*, 2006) further complicate sea level rise predictions.

Ice discharge through glaciers accounts for  $\sim$ 70% of the total mass loss from Greenland (*Rignot and Kanagaratnam*, 2006) and  $\sim$ 90% of the mass loss from Antarctica (*Rignot and Thomas*, 2002). Many of these outlet glaciers are undergoing rapid changes in dynamics with significant mass balance effects. In this study we quantify, for the first time, the current and historical flow dynamics of several key outlet glaciers in East Greenland and East Antarctica.

The mechanisms driving the large changes in Greenland glacier dynamics are not fully understood. Observations of thinning, retreat, and acceleration show a latitudinal response (*Rignot and Kanagaratnam*, 2006), in which glaciers south of 70°N have undergone large changes in flow dynamics, but glaciers north of 70°N have not (*Stearns et al.*, 2005a). The near-coincident timing of the changes observed on Kangerdlugssuaq and Helheim glaciers in East Greenland (*Stearns and Hamilton*, 2007), several smaller outlet glaciers in the south-east (*Rignot and Kanagaratnam*, 2006), and Jakobshavn Isbræ in the west (*Joughin et al.*, 2004), suggests a common trigger such as climate warming may be responsible. These observations highlight the sensitivity of large outlet glaciers to

climate-related perturbations and imply that current estimates for the predicted sea level contribution from the Greenland Ice Sheet need to be re-evaluated to account for rapid changes in ice dynamics.

Over the past 30 years, Arctic surface temperatures have increased  $0.5^{\circ}\text{C}$  per decade (Comiso, 2000). This warming has been accompanied by other changes: sea ice extent has decreased  $8.6 \pm 2.9\%$  (Serreze *et al.*, 2007) and northern hemisphere ocean temperatures have warmed by  $0.19 \pm 0.13^{\circ}\text{C}$  (Rayner *et al.*, 2006) in the past decade. In Greenland alone, surface observations indicate recent increases in temperature ( $\sim 1.5^{\circ}\text{C}$  per decade; Box *et al.*, 2006), seasonal ablation (16% per decade; Abdalati *et al.*, 2001), surface melt water runoff ( $\sim 19\%$  per decade; Box *et al.*, 2006; Hanna *et al.*, 2005), and net mass loss (140% from 2000 to 2005; Rignot and Kanagaratnam, 2006). Preliminary studies (Yang, 2007; Zwally *et al.*, 2002) hint at a potential correlation between increasing Greenland summer surface temperatures and glacier flow speeds. Current models (even those excluding the dynamic response of outlet glaciers) predict collapse of the Greenland Ice Sheet if surface temperatures increase by  $3^{\circ}\text{C}$  (Church *et al.*, 2001; Gregory *et al.*, 2004). When enhanced surface melt and subsequent glacier accelerations are included in models, the Greenland Ice Sheet becomes more sensitive to warming temperatures (Parizek and Alley, 2004).

Models suggest that the East Antarctic Ice Sheet (EAIS) will remain largely stable if warming is less than  $5^{\circ}\text{C}$  (e.g., Huybrechts and de Wolde, 1999), although, again, these models do not include the effects of rapid changes in ice flow or ocean warming. The pattern of observed surface temperature changes in EAIS is complicated (Comiso, 2000; Chapman and Walsh, 2007), with areas of cooling and warming. EAIS glacier catchment basins are in regions that have undergone  $\sim 0.1^{\circ}\text{C}$  warming per decade from 1958 – 2002 (Chapman and Walsh, 2007). While widespread melting and meltwater-induced flow accelerations are less likely than in Greenland, the warming temperatures might have a more subtle effect. The force balance of a glacier at or near flotation is very sensitive to thickness perturbations at the grounding line (Benn *et al.*, 2007; Pfeffer, 2007; Van der Veen, 2002), such as those caused by surface or ocean warming. Several East Antarctic outlet glaciers are thinning and accelerating at or near their grounding lines (Chapter 3), possibly due to

warming (*Gille*, 2002; *Levitus et al.*, 2005) and freshening (*Jacobs et al.*, 2002; *Jacobs*, 2006; *Rintoul*, 2007) of Ross Sea waters in the past decade. Oceanographic forcing might be playing a role in changing ice dynamics (*Payne et al.*, 2004).

## 1.2 Glacier Dynamics

Outlet glaciers draining the East Antarctic and Greenland ice sheets share many characteristics of size, topographic setting and geometry, which distinguish them from low-gradient ice streams (*Bentley*, 1987). There are also several notable differences. First, outlet glaciers of the Greenland Ice Sheet, unlike those in East Antarctica, are at low elevation and relatively low latitudes, which increases the potential for extensive surface melting. Second, most East Antarctic outlet glaciers are buttressed by ice shelves whereas Greenland glaciers terminate in tidewater fjords and have little or no floating tongues. Flow speeds of Greenland glaciers are also several times faster than East Antarctic glaciers. In a warmer climate, East Antarctic outlet glaciers might behave more like present-day Greenland glaciers, with extensive surface melt, no ice shelf and faster flow speeds. Here, we investigate the current changes taking place in both polar regions.

### 1.2.1 Tidewater Glacier Dynamics

Glaciers that terminate in fjords or the open ocean are very sensitive to changes in ocean dynamics (temperature, circulation and sea level), and other factors affecting terminus buoyancy conditions. Tidewater glaciers are subject to large changes in flow dynamics on short timescales ranging from days to decades, as a result of forcings as diverse as ocean tides (*Hamilton et al.*, submitted) and climate (*Shepherd et al.*, 2001; *Thomas et al.*, 2003); this variability makes it difficult to predict tidewater glacier response in a warming climate and so contributes one of the largest sources of uncertainty in current sea level models (*Bindoff et al.*, 2007; *Lemke et al.*, 2007).

Many tidewater glaciers go through cycles of slow terminus advance followed by rapid retreat (*Post*, 1975). These patterns are observed in tidewater glaciers in Alaska (e.g., Columbia Glacier, LeConte Glacier) (*Meier and Post*, 1987; *O’Neel et al.*, 2001), Patag-

onia (Aniya *et al.*, 1997; Rignot *et al.*, 2003), the Antarctic Peninsula (Pritchard and Vaughan, 2007), and Greenland (e.g., Jakobshavn Isbræ) (Joughin *et al.*, 2003; Sohn *et al.*, 1998). Erosion and sediment transport rates beneath fast-moving tidewater glaciers are large (e.g., Alley *et al.*, 2007; Motyka *et al.*, 2006), and a tidewater glacier gradually builds a terminal moraine shoal at its grounding lines. The glacier advances slowly, typically 20 – 40 m yr<sup>-1</sup>, as the moraine grows and migrates (Meier and Post, 1987; Nick *et al.*, 2007). Gradual advance continues until ice discharge exceeds accumulation, and the glacier is no longer in balance. An increase in ice discharge can be due to increased surface melting (over a longer glacier), increased calving, or a change in buoyancy conditions at the terminus (Nick *et al.*, 2007). At this point, the front of the glacier either remains stationary, or begins to retreat.

Tidewater glaciers are unique because of the direct interaction between land ice and the ocean. Consequently, their behavior is sensitive to changes at the ice-ocean interface, or processes at the calving front. The processes that control calving rates are disputed, with the central issue being whether flow acceleration causes glacier retreat, or whether glacier retreat causes flow acceleration (Benn *et al.*, 2007). Several studies using observations from Jakobshavn Isbræ (Hughes, 1986; Joughin *et al.*, 2004), Helheim Glacier (Howat *et al.*, 2005), and Columbia Glacier (Meier, 1997; Meier and Post, 1987), show that enhanced calving triggers a dynamic change in flow speed and ice thickness, which rapidly propagates up-glacier. Other studies on the same suite of glaciers (Thomas *et al.*, 2003; Luckman *et al.*, 2006; Van der Veen, 1996; Venteris, 1999) suggest that thinning precedes rapid retreat rates and that increased calving is simply a consequence of changes in glacier geometry. The retreat of several tidewater glaciers is preceded by long-term thinning, particularly towards the front of the glacier (Van der Veen, 2002). Thinning may be initiated by climate warming, or a dynamic adjustment of the glacier to flow acceleration. Columbia Glacier thinned and retreated rapidly following regional warming over the past few centuries (Pfeffer *et al.*, 2000). Thinning from regional warming also caused the retreat of several calving glaciers in southern South America (Aniya, 1999; Warren and Aniya, 1999). According to an inventory of calving glaciers in southern Patagonia, large thinning rates

( $>10$  m yr $^{-1}$ ) occur on glaciers that are retreating rapidly ( $>300$  m yr $^{-1}$ ), whereas glaciers that are not retreating (or are retreating slowly) exhibit small thinning rates (Aniya *et al.*, 1997; Naruse *et al.*, 1995).

### 1.2.2 Ice Shelf Buttressing of Glacier Flow

Perhaps the key difference between outlet glaciers in Greenland and those draining East Antarctica through the Transantarctic Mountains is that the latter drain into an ice shelf. The Ross Ice Shelf buffers the grounded ice of the EAIS outlet glaciers from stretching forces that would exist if the ice fronts were at the grounding line (Dupont, 2004). Ice shelf buttressing reduces the stretching force because the ice shelf undergoes lateral drag at its boundaries and basal drag at localized areas of grounding (e.g., Crary Ice Rise). A freely-floating (un-pinned and un-grounded) ice shelf would still provide a "back force", but it would be greatly reduced (MacAyeal, 1989; Thomas and MacAyeal, 1982).

The removal of an ice shelf in both observations (de Angelis and Skvarca, 2003; Rignot *et al.*, 2004; Rott *et al.*, 2002; Scambos *et al.*, 2004) and in model simulations (Dupont, 2004; Dupont and Alley, 2005) results in rapid acceleration and thinning of the glaciers that it once buttressed. On Pine Island Glacier, thinning and volume loss extended far inland ( $>200$  km) (Shepherd *et al.*, 2001) in response to weakening of the ice shelf and grounding line retreat (Payne *et al.*, 2004). Similarly, glaciers on the Antarctic Peninsula underwent rapid flow acceleration and thinning, following the break-up of the Larsen B Ice Shelf, which provided substantial buttressing (Scambos *et al.*, 2004; Rignot *et al.*, 2004). Increased extensional longitudinal stress gradients can quickly propagate up-flow, causing thinning, followed by grounding-line retreat and acceleration on decadal or shorter timescales (Dupont and Alley, 2005; Payne *et al.*, 2004).

The response of the Siple Coast ice streams in West Antarctica to changes in the Ross Ice Shelf has been studied intensively for the past few decades, motivated by evidence that the West Antarctic Ice Sheet collapsed relatively recently ( $\sim 120$  kya) (Scherer *et al.*, 1998), and by the observation that, as a marine based ice sheet, it is thought to be inherently unstable (Mercer, 1978; Thomas and Bentley, 1978; Weertman, 1974). Far less attention

has been paid to the effect of Ross Ice Shelf removal on EAIS outlet glaciers. However, recent modeling suggests that glaciers with high driving stresses, large basal drag and reduced side drag are more sensitive to changes in buttressing than other glaciers (*Dupont*, 2004). The steep gradient East Antarctic outlet glaciers have high driving stresses (~250 kPa), strong resistance from basal drag (~150 kPa) and minimal resistance from lateral drag (~50 kPa), and longitudinal compression (~50 kPa) (*Scofield et al.*, 1991; *Whillans et al.*, 1989), making them potentially sensitive to ice shelf changes.

Recent observations from the Antarctic Peninsula show that ice shelf stability is sensitive to melting caused by rapid surface and ocean warming (*Scambos et al.*, 2000; *Shepherd et al.*, 2001, 2004). Numerical models suggest that the Ross Ice Shelf is vulnerable to a 2 – 3°C surface temperature increase (*Humbert et al.*, 2005), which is plausible during this century due to climate warming (*Shindell and Schmidt*, 2004). Even a modest weakening of the Ross Ice Shelf due to surface or bottom melting could propagate significant mass balance effects inland via the EAIS outlet glaciers.

### 1.3 Dissertation Aims and Objectives

Uncertainties in the mass balance of polar ice sheets and the flow dynamics of their large outlet glaciers are among the largest sources of uncertainty in current sea level rise predictions. In this dissertation remote sensing techniques are used to quantify the current changes in flow behavior taking place in East Greenland and East Antarctica. These new data sets are used to address the following questions concerning outlet glaciers.

1. How have the flow speeds of the major outlet glaciers in East Greenland and East Antarctica changed over the time periods of observation?
2. What are the dominant controls on flow speed of these rock-walled glaciers?
3. What is the mass balance of these outlet glaciers and their catchments?
4. What is the contribution of these glaciers to sea level rise?

## **1.4 Dissertation Outline**

The body of the dissertation consists of 6 chapters: Chapter 1 is this introduction and Chapter 6 is the conclusion. Chapters 2 – 5 are written as individual papers, and are in various stages of peer-review or publication in scientific journals. These chapters each contain their own introduction, methods, discussion of results, and conclusion. There is one reference list, encompassing all the chapters, following Chapter 6.

### **1.4.1 Chapter 2: A Comparison of High-Rate GPS and Satellite Remote Sensing Measurements on Helheim Glacier, East Greenland**

We test the validity of the remote sensing procedures used throughout this dissertation by comparing satellite-derived estimates of ice velocity and elevation with ground-based GPS measurements. This is the first such study describing a direct comparison of remotely-sensed observations with terrestrial velocity measurements.

### **1.4.2 Chapter 3: Recent Dynamics of Four Large East Antarctic Outlet Glaciers**

This chapter describes the ice dynamic characteristics of East Antarctic outlet glaciers draining into the Ross Sea embayment. Results indicate that some East Antarctic outlet glaciers, long believed to be stable, are undergoing recent changes in ice dynamics. We also present mass balance estimates, and argue that unusually large imbalances are the result of erroneous accumulation rates.

### **1.4.3 Chapter 4: Multi-Decadal Record of Ice Dynamics on Daugaard Jensen Glacier, East Greenland, from Satellite Imagery and Terrestrial Measurements**

Here, we describe the procedures for constructing a long ice dynamics record for a major outlet glacier in East Greenland. The results indicate a several-decades long period of stable behavior. The chapter, originally published in *Annals of Glaciology*, vol. 42, 2005 (*Stearns et al.*, 2005a), has been modified to include updated velocities and terminus positions, and a force balance analysis.

#### **1.4.4 Chapter 5: Rapid Volume Loss from Two East Greenland Outlet Glaciers Quantified using Repeat Stereo Satellite Imagery**

This chapter describes recent surface elevation changes on two large glaciers in East Greenland, obtained by differencing ASTER-derived DEMs. The results indicate that between 2001 – 2006, these two glaciers accounted for >20% of the total mass lost from Greenland, and up to ~10% of the observed global sea level rise over the same period. This chapter was published in *Geophysical Research Letters*, vol. 34, 2007 (Stearns and Hamilton, 2007) and has been updated to include recent velocity data and calving front positions for both glaciers.

#### **1.4.5 Chapter 6: Concluding Remarks**

This chapter summarizes the dissertation results, and highlights the contribution of this research to our understanding of the interaction between polar glaciers, climate, and sea level. Also in this chapter are recommendations for future work and suggestions for how to improve catchment-wide mass balance analyses.

## Chapter 2

# A COMPARISON OF HIGH-RATE GPS AND SATELLITE REMOTE SENSING MEASUREMENTS ON HELHEIM GLACIER, EAST GREENLAND

### 2.1 Introduction

Satellite remote sensing has revolutionized polar glaciology by providing frequent coverage over large spatial regions that are difficult to access by field-based programs. Sequential observations extending over several decades offer the potential for longer-term studies than are usually possible with traditional field methods. The capability of satellite sensors to operate across a wide range of the electromagnetic spectra provides data necessary to understand new processes and monitor glacier behavior (*König et al.*, 2001).

Spaceborne measurements of surface elevation and flow speed are of particular relevance to studies of ice dynamics. Radar and laser altimetry is the most common method of obtaining surface elevations (e.g., *Johannessen et al.*, 2005; *Krabill et al.*, 2004; *Thomas et al.*, 2006; *Wingham et al.*, 2006), but elevations can also be extracted from optical imagery using photocalinometry (e.g., *Scambos and Fahnestock*, 1998) and stereo imaging (e.g., *Berthier et al.*, 2005; *Stearns and Hamilton*, 2007). Glacier velocities can be derived from interferometric analysis (e.g., *Joughin et al.*, 1999) or speckle tracking on radar images (e.g., *Wuite*, 2006), or from feature tracking on visible band images (e.g., *Howat et al.*, 2005; *Scambos et al.*, 1992; *Stearns et al.*, 2005a). Each technique has its advantages and limitations.

In this study, ice velocity is derived from optical satellite imagery by tracking the displacement of surface features in sequential images. Feature tracking can be performed at varying levels of complexity ranging from manual (e.g., *Lucchitta and Ferguson*, 1986), to semi-automatic (e.g., *Ferrigno et al.*, 1993), to automatic (e.g., *Scambos et al.*, 1992; *Whillans*

*and Tseng, 1995*), with each technique producing a progressively larger number of matches. Here, we assess the accuracy of a widely-used automatic feature tracking technique.

Validating, or ground-truthing, remote sensing data sets is necessary to verify that the information extracted from the satellite data accurately characterizes geophysical processes. In this study, we use ground-based GPS elevation and velocity measurements to assess the accuracy of ASTER-derived data products. ASTER (Advanced Spaceborne Thermal Emission and Reflection Radiometer) imagery has been used extensively in glaciology to map changes in glacier geometry (e.g., *de Angelis and Skvarca, 2003*), surface elevation and volume change (e.g., *Howat et al., 2005; Kääb et al., 2002; Paul et al., 2004; Stearns and Hamilton, 2007; Vignon et al., 2003*), and ice velocity (e.g., *Howat et al., 2005; Kääb et al., 2002; Stearns et al., 2005a*), although few of these studies have been validated with field measurements.

Collecting ground-truth data in the polar regions is logically challenging and expensive, and difficult to coordinate with satellite image acquisitions. Consequently, few ground-based measurements are available to directly validate satellite data. *Frezzotti et al. (1998)* compared GPS data with Landsat TM derived velocities in East Antarctica, but the data sets spanned different time periods, meaning a direct validation was not possible.

Helheim Glacier ( $66.5^{\circ}\text{N}$ ,  $38^{\circ}\text{W}$ ), located in East Greenland, has undergone rapid changes in ice dynamics in the past few years (e.g., *Howat et al., 2005; Luckman et al., 2006; Stearns and Hamilton, 2007*) including rapid flow acceleration (by  $\sim 40\%$  at the glacier front), thinning (up to  $60 \pm 13$  m in one year), and retreat ( $\sim 5$  km between 2003 – 2005) (*Stearns and Hamilton, 2007*). These events and changes were largely quantified using repeat ASTER images of Helheim Glacier.

GPS instruments were deployed on Helheim Glacier to collect high-rate velocity measurements during the 2006 summer. The ASTER sensor, on board the Terra satellite, obtained two usable images of Helheim Glacier while the GPS units were operating. This overlap provides a rare opportunity to compare satellite-derived ice velocity and surface elevation measurements with ground-based field data.

## 2.2 Data

### 2.2.1 Ground-based GPS surveys

We installed a network of 19 Global Positioning System (GPS) receivers on and around Helheim Glacier in late June, 2006. Sixteen receivers were installed on the glacier, in a configuration including stations both on the glacier centerline, and offset from the centerline (Figure 2.1). Three GPS receivers were installed at rock sites (sites 1 – 3) surrounding the on-ice network to help define a stable geodetic reference frame (Figure 2.1). Nine of the stations spanned an upglacier distance of  $\sim$ 20 km from a point  $\sim$ 15 km behind the calving front. The stations operated for  $\sim$ 60 days, and recorded data at a rate of 1 sample/5 seconds. In addition to the long-term GPS network, we deployed four receivers (sites 14 – 19), for 2 – 5 days each, at locations just behind the calving front.

The GPS data were processed using the GIPSY software package (*Lichten and Border*, 1987) and high-precision kinematic data processing methods (e.g., *Elósegui et al.*, 1996, 2006) to estimate the time-dependent positions of GPS sites on the glacier relative to the static antennas on nearby bedrock. Processing incorporated precise satellite orbits from the International GNSS Service (IGS), with no further orbit improvement.

In this study, we are only interested in the GPS data that overlap the satellite images: the period from August 25 to August 30, 2006. A second-order quadratic is fit to the position data to obtain daily velocities. A linear fit was applied to the sites at the calving front (sites 14 – 17), which were occupied for a shorter time interval. Uncertainties in velocity are less than  $0.1 \text{ m d}^{-1}$  (*Hamilton et al.*, submitted).

### 2.2.2 Satellite Remote Sensing

The Terra satellite, which carries the ASTER sensor, was launched in 1999 and travels in a circular, nearly polar orbit 705 km above the Earth's surface. The orbit is sun-synchronous, crossing the equator at 10:30 AM, and returning to the same orbit every 16 days (or 233 orbits) (*Yamaguchi et al.*, 1998). Across-track pointing capabilities of  $\pm 24^\circ$  in the visible and near infrared (VNIR) bands enable ASTER to image up to  $\sim 84^\circ\text{N/S}$ . Across-track pointing also allows for more frequent repeat coverage than the nominal

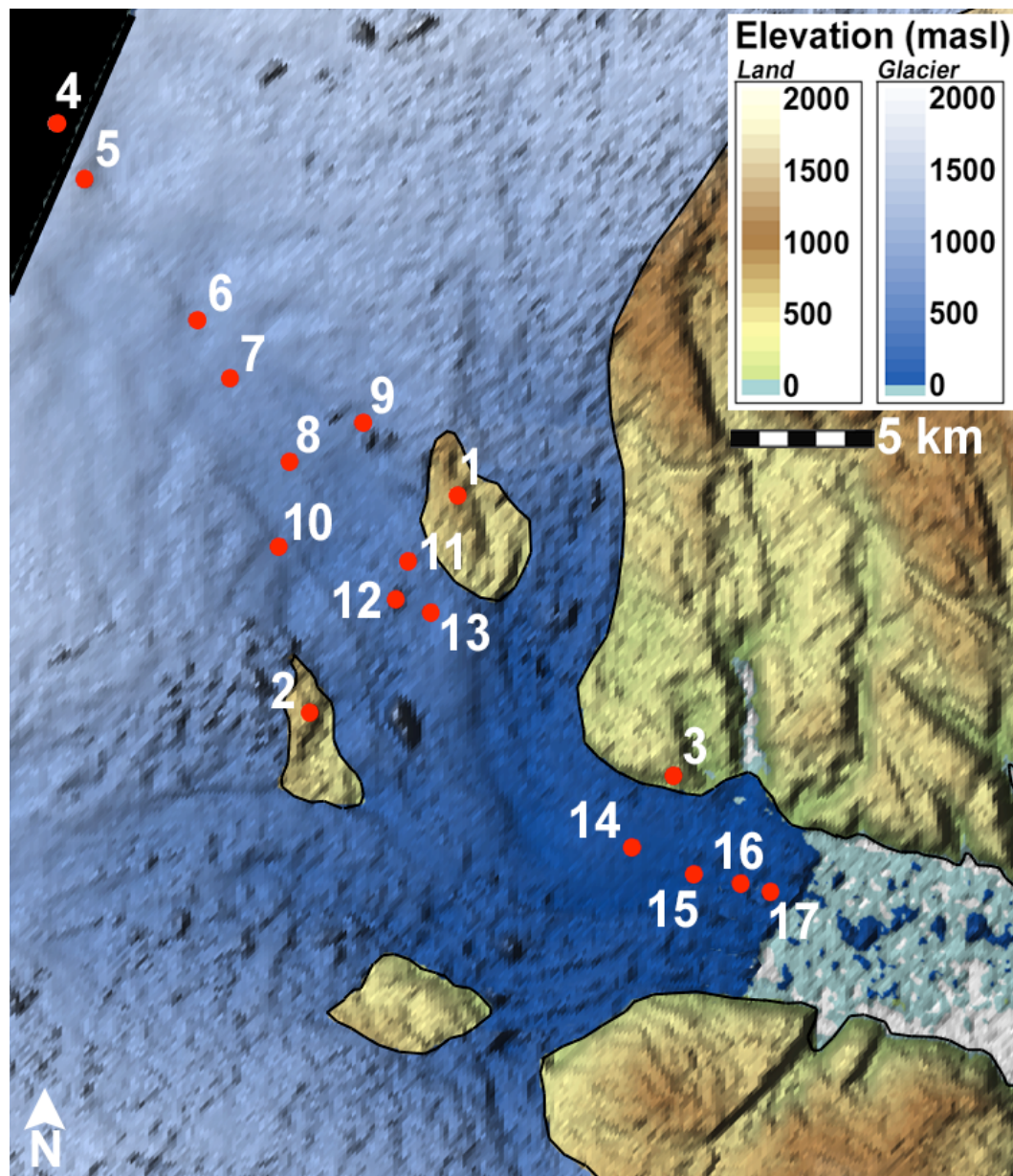


Figure 2.1. A DEM of Helheim Glacier, derived from an ASTER image taken on August 30, 2006. The red dots represent GPS instruments which operated between August 25 - 30, 2006.

16-day repeat orbit; for example, the images of Helheim Glacier were acquired 5 days apart, on August 25 and 30. ASTER collects images in 14 bands ranging from visible to thermal infrared wavelengths with high spatial, spectral, and radiometric resolution (*Fujisada et al.*, 2005). The VNIR band data used extensively in this thesis have a 15 m spatial resolution. Individual ASTER scenes are 60 km x 60 km.

### 2.2.2.1 ASTER-derived DEMs

The ASTER instrument acquires stereo imagery using a nadir (3N) and backward (3B) viewing telescope in the VNIR band 3 (*Yamaguchi et al.*, 1998). The backward-looking telescope points 27.6° off-nadir (Figure 2.2). Together, bands 3N and 3B can be used to produce a 30 m horizontal-resolution digital elevation model (DEM) of a 60 km x 60 km scene.

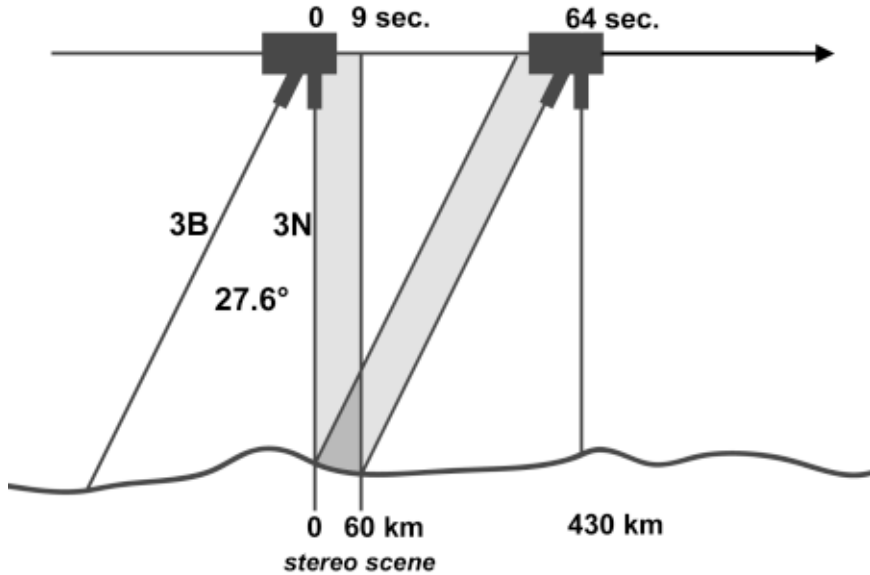


Figure 2.2. The acquisition of an ASTER stereo scene. The 3N (nadir band 3) scene and the corresponding 3B (backward-looking) scene are taken ~60 seconds apart. The width of the grey bands represent the 60 x 60 km ASTER image footprint (after Käab, 2002).

DEM generation from stereo satellite imagery is not a new technique (e.g., *Berthier et al.*, 2007; *Ehlers and Welch*, 1987; *Eldhuset et al.*, 2003; *Grabmeier et al.*, 1998; *Paul et al.*, 2004; *Toutin*, 2002a,b; *Zommer*, 2002). The advantage of ASTER stereo-imagery is that im-

ages with the necessary different viewing angles are acquired nearly simultaneously ( $\sim$ 60 seconds apart), rather than days or months apart as with SPOT (e.g., *Berthier et al.*, 2005) and other image types. This eliminates the problem of surface de-correlation (due to snowfall, melting, ice motion, etc.) inherent in the other techniques (*Toutin*, 2002b; *Kääb*, 2002).

Two DEMs were generated using ASTER images taken at mid-day on August 25 and August 30, 2006. Processing of the stereo bands to epipolar geometry, and parallax-matching was done automatically using commercial software developed by the Japanese ASTER Science Team and described by *Fujisada et al.* (2005). Products generated using identical procedures can be ordered from the NASA/USGS Land Processes Distributed Active Archive (LPDAAC) at <http://edcimmswww.cr.usgs.gov/pub/imswelcome>. The commercial software produces DEMs with a post-spacing of 30 m, which are subsequently interpolated to 15 m to match the resolution of the VNIR bands.

Geolocation of the ASTER DEMs is entirely on the basis of the satellite ephemeris information contained in the image header file, which is considered to be better than 50 m (*Fujisada et al.*, 2005). DEM uncertainties are a combination of systematic errors, and random errors due to satellite positioning, image acquisition geometry, and atmospheric conditions. We detect a systematic bias in the vertical of  $-17.79$  m between the two DEM scenes based on relative elevation differences of static bedrock surfaces. Once this bias is removed, calculated random errors contribute to a root mean square error of  $\pm 7.1$  m for the image pair, based on a comparison of elevation differences in static regions (*Stearns and Hamilton*, 2007). This error is consistent with *Fujisada et al.* (2005), who report a DEM vertical accuracy of 20 m with 95% confidence ( $2\sigma$ ). *Rivera et al.* (2005) reports an rms error of 17 m, based on a comparison of ASTER DEMs and photogrammetrically-produced DEMs. In a similar study, *Kääb* (2002) compared ASTER DEMs with DEMs produced by photogrammetry for mountain regions in the Swiss Alps and New Zealand. In such cases, uncertainties in absolute elevations can be quite large ( $\sim$ 60 m rms) because of rugged topography (*Kääb*, 2002). The uncertainties in relative elevations, important for surface elevation change and volume loss estimates, are usually much smaller. *Stevens*

*et al.* (2004) note that, in the absence of appreciable atmospheric water vapor, rms uncertainties for relative ASTER DEMs are less than 10 m for moderately rugged terrain.

### 2.2.2.2 ASTER-derived Velocity Data

Velocities are derived from automatic tracking of surface features on sequential ASTER images using a cross correlation technique implemented in the IMCORR software package (*Scambos et al.*, 1992). The software was originally developed for mapping displacements on low-slope ice streams in West Antarctica (e.g., *Bindschadler and Scambos*, 1991; *Scambos et al.*, 1992) from Landsat imagery, but has been adapted to steep, fast moving outlet glaciers and other image types (*Whillans and Tseng*, 1995; *Wuite*, 2006). IMCORR tracks the translational displacement of surface features (e.g., crevasses, seracs) in two co-registered and ortho-rectified images. The program uses a normalized cross-covariance correlation method to match the surface features in each image pair.

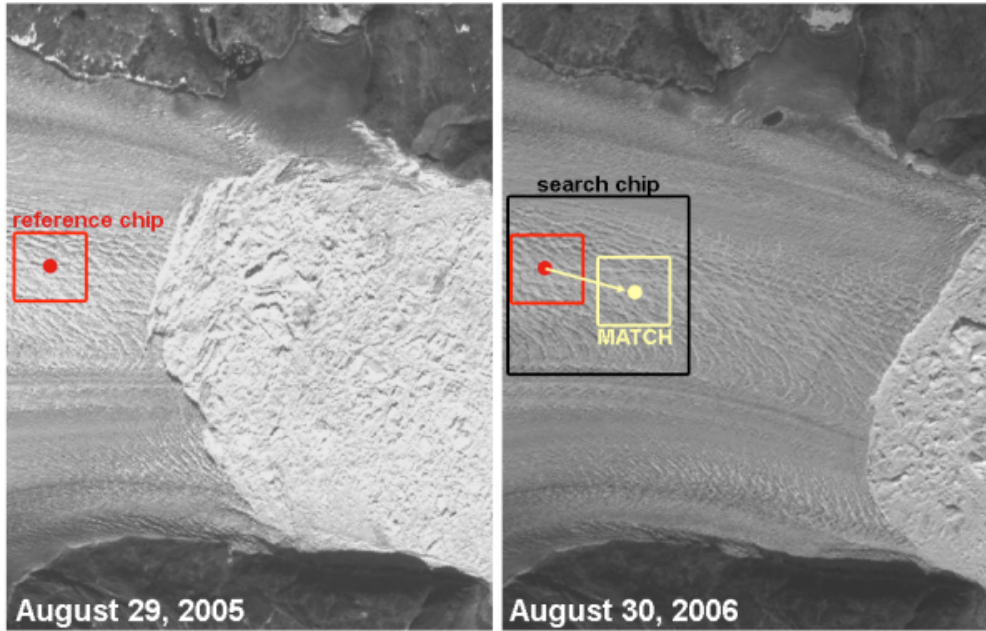


Figure 2.3. Two ASTER scenes of Helheim Glacier illustrating the IMCORR technique. A reference window in the 2005 scene is compared with a larger search window in the 2006 scene. Once a match is found, the displacement is calculated from the mid-point of the two chips. Boxes are enlarged in the figure, for clarity.

IMCORR uses small subscenes ("chips") from each image to track displacements. A "reference chip" from the older image moves in a grid-like pattern through a "search chip" in the newer image (Figure 2.3). If a match (correlation) is found, IMCORR calculates the correlation index and displacement. The reported match is the location with the maximum correlation value. The shape of the correlation function is an important indicator of measurement accuracy: the sharper the peak, the more accurate the match (*Wuite*, 2006). If no match is found, a null output is received.

IMCORR allows the user to control the size and offset of the chips to adjust for the time separation of the images, the speed of the glacier, the size of 'trackable' features, and the direction of flow. Because glacier flow speeds can range from centimeters to kilometers per year within a single image, the strength of the correlation will vary. Optimizing the correlation strength can be done by manually adjusting the chip sizes, or implementing an automatic adjustment in the code (*Wuite*, 2006).

Sequential images used for cross-correlation must be largely cloud free, and are required to have similar illumination characteristics (*Scambos et al.*, 1992). The ASTER instrument's across-track, off-nadir scene acquisition capability ( $\pm 24^\circ$ ) in the VNIR introduces an image geometry change that must be considered during scene selection. Over regions of rugged relief, such as in East Greenland, we find that the pointing angles of sequential images need to be within  $3^\circ$  to maintain similar geometric characteristics. If the pointing angle difference is greater than  $3^\circ$ , panoramic distortion inhibits cross-correlation. A further consideration is the time interval between sequential image acquisition. The time separation must be long enough for features to be displaced more than the measurement uncertainties, but not so long that features are distorted beyond recognition.

The measured displacements of surface features have several sources of uncertainty originating from image ortho-rectification, co-registration, and application of the feature matching technique. Ortho-rectification using the ASTER DEM translates the DEM errors onto the ortho-rectified image. *Kääb* (2002) reports a 10 m ground position error for rough terrain and a 3 m error for moderate terrain based on a similar analysis in the Swiss Alps.

Overall, resampling errors during ortho-projection translate to positional errors that are at the sub-pixel ( $<15$  m) level.

Uncertainties associated with the image cross-correlation technique are also smaller than the pixel size of 15 m. Matches with uncertainties larger than 1 pixel are discarded. The velocity errors scale with the time separation of the image pairs. In this study, because our two images are only 5 days apart, the cumulative velocity error is relatively large ( $\pm 4.24$  m d $^{-1}$ , or  $\sim 21\%$  of the total velocity).

## 2.3 Results

### 2.3.1 Elevation

The DEM software outputs elevations in the EGM96 geoid, at an interpolated post-spacing of 15 m. To permit a comparison with GPS ellipsoidal heights, the DEM heights were converted to the WGS-84 ellipsoid using parameters found at <http://earth-info.nga.mil/GandG/wgs84/gravitymod/egm96/intpt.html>. (The geoid–ellipsoid difference is  $\sim 50$  m at Helheim Glacier). The results of the comparison are shown in Figure 2.4A and Table 2.1. The August 30 DEM has a systematic bias of  $-17.79$  m, and consistently under-estimates the GPS elevations with an rms difference of 33.71 m. The rms difference between the August 25 DEM and the GPS elevations is 12.56 m. These comparisons are based on DEMs with 15 m post-spacings and the nominal pixel coordinates of each GPS site. GPS sites were installed on the peaks of nunataks (rock sites 1 – 3) and on relatively high locations on the ice (sites 4 – 17) to improve satellite visibility, which partly explains why the ASTER DEMs systematically under-estimate the GPS measurements. Some of the remaining difference might be due to image geolocation. The geolocation uncertainty of the ASTER DEMs ( $\sim 50$  m) (Fujisada *et al.*, 2005) means that the best elevation match is not always at the pixel location prescribed by the coordinates of the GPS site. The GPS to DEM elevation differences can be minimized by searching for better elevation matches in pixels within 50 m of the original pixel (i.e., within the range of geolocation uncertainty of the GPS site on the image) (noted with a '\*' in Figure 2.4). The results show

an rms difference of 9.56 m for the August 25 DEM, and 25.52 m for the August 30 DEM (Table 2.1).

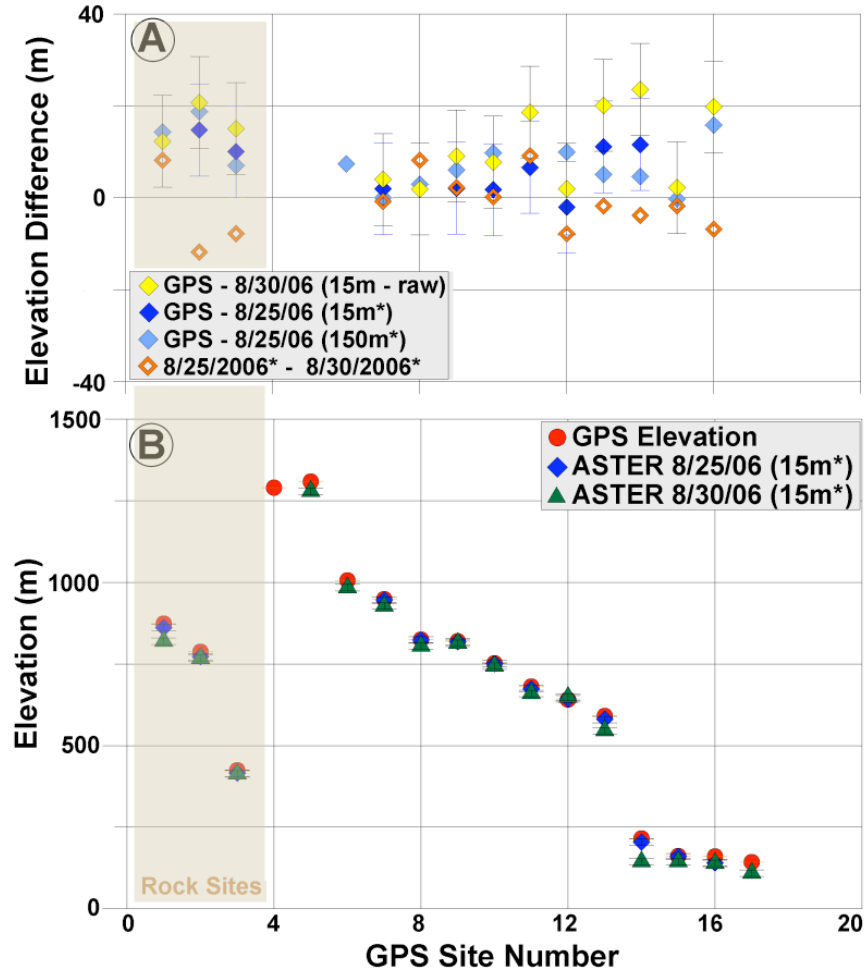


Figure 2.4. Elevation results from GPS and two ASTER-derived DEMs. A) Elevation differences between GPS data and the ASTER DEMs. “Raw” elevations are the values for pixels nominally-containing each GPS site. The ‘\*’ indicates that better elevation matches were obtained from neighboring pixels (within 50 m). The 8/25 – 8/30/2006 comparison is done with bias-corrected values for the 8/30/2006 DEM. ASTER elevation uncertainties are  $\pm 10$  m, as described in the text. B) GPS results, and ASTER elevations from a DEM with 15 m pixel post-spacing.

When comparing glacier surface elevations over time, the accuracy of each DEM relative to other DEMs is more important than the absolute accuracy of an individual DEM. We detect a systematic bias between the two DEMs, in which the August 30 DEM yields elevations consistently lower than the August 25 DEM by an rms of  $-17.79$  m. The bias

was quantified by measuring the elevation difference over static bedrock regions on the two images, in 5 km x 5 km boxes. The bias accounts for most of the rms difference of 22.94 m between the two DEMs (at each GPS location). When the August 30 DEM is corrected for the bias, the rms difference drops to 6.52 m. Most of the remaining difference is due to "noise". The 15 m DEMs are "noisy" products, as a result of the crevassed and rugged surface of Helheim. *Stearns and Hamilton* (2007) smoothed much of this noise by resampling the DEMs to 150 m using a bicubic spline. By carrying out a similar smoothing of the August 25 and August 30 DEMs, we obtain rms differences of 10.53 m (Table 2.1).

DEM description	August 25 , Absolute DEM	August 30, Absolute DEM	Relative DEM
15 m	12.56 m	33.71 m	17.31 m
15 m*	9.56 m	25.52 m	22.94 m
150 m*	9.37 m	16.86 m	10.53 m

Table 2.1. Summary of errors for absolute and relative DEMs of different post-spacings. The '\*' indicates that elevations from neighboring pixels (within 50 m) were considered. The absolute DEM rms quantifies the difference between the GPS elevations and the elevations derived from ASTER DEMs on August 25 and August 30. The relative DEM describes the rms difference between the two DEMs at each site.

### 2.3.2 Velocity

Velocities were derived from the two ASTER scenes using several different IMCORR input parameters and grid sizes. The grid interval determines the spacing of the reference chips, and therefore the number of velocity vectors. A small grid interval will increase the number of vectors, but can lead to over-sampling because the individual vectors are not statistically independent (*Wuite*, 2006). The results, shown in Figure 2.5, suggest that different grid spacings produce slightly different velocities. An IMCORR grid spacing of 5 grid cells, which results in a post-spacing of 75 m (because the image resolution is 15 m), generates slightly faster velocities, probably because of the over-sampling issue mentioned above.

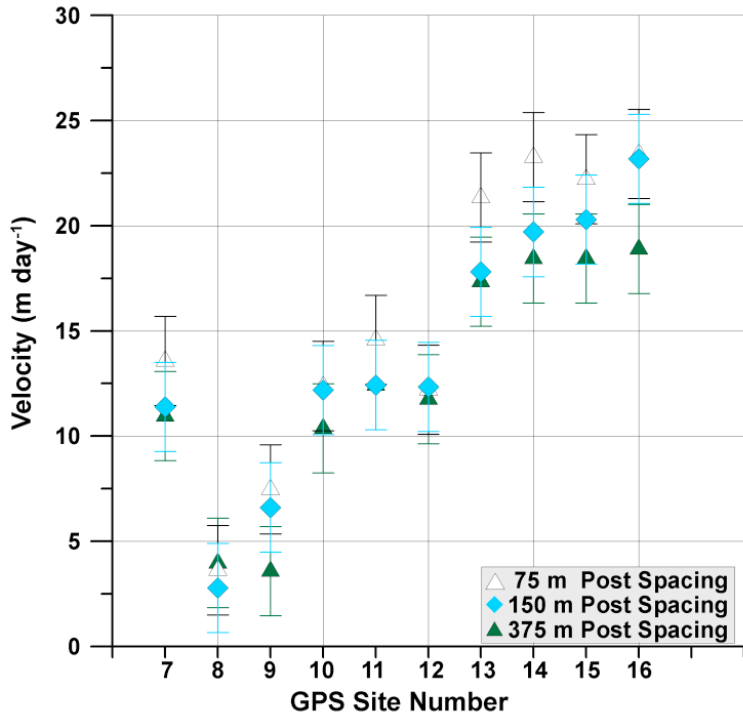


Figure 2.5. The influence of different IMCORR grid spacings on derived velocities.

Overall, the ASTER-derived velocities are consistent with the GPS measurements (Figure 2.6). The rms difference between the GPS and the ASTER velocities (gridded to 150 m) is  $\pm 0.89 \text{ m d}^{-1}$ , well within the errors assigned to the ASTER results. The offset is higher using velocities gridded to 375 m ( $\pm 2.46 \text{ m d}^{-1}$ ) and 75 m ( $\pm 1.53 \text{ m d}^{-1}$ ). For Helheim Glacier, a fast-flowing glacier, gridding the feature tracking results to 150 m seems to generate flow speeds which best match the GPS observations. Depending on the gridding routine, individual point measurements have an rms difference of between 0.89 and 2.46  $\text{m d}^{-1}$ , or 6 – 17% of the flow speed.

The IMCORR software outputs the displacements in X and Y components, which are used to determine the direction of flow (Figure 2.7). The ASTER flow azimuths are compared with the GPS results in Figure 2.7. The rms difference of the azimuths is  $\pm 8.60^\circ$ . This small difference shows that the feature tracking results duplicate both the magnitude and direction of flow, even with a very short time separation between the image pairs.

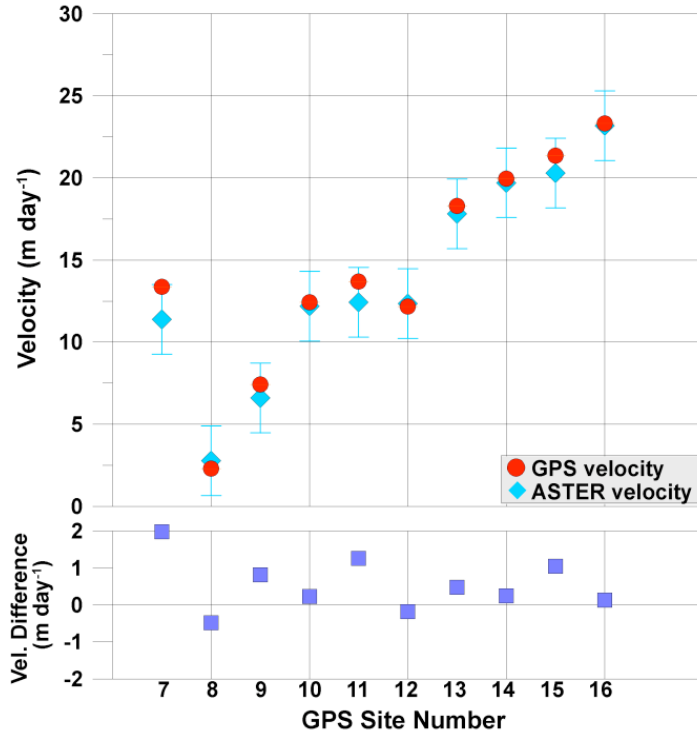


Figure 2.6. Velocity results from GPS and ASTER-derived velocity measurements.

## 2.4 Discussion and Conclusion

A direct comparison of satellite data and terrestrial measurements shows that ASTER imagery is well-suited for applications in glacier dynamics. Velocity measurements derived from ASTER images capture the magnitude and direction of ice flow. The rms difference between the ASTER DEMs and the GPS elevations ranges from 9.37 – 12.56 m (for the DEM with no systematic bias), depending on whether smoothed or unsmoothed DEMs are used. Most of the elevation errors arise from the geolocation error of individual images, with the remaining difference probably being due to GPS sites being placed on locally high terrain to improve satellite visibility. The two ASTER DEMs demonstrate good repeatability over the glacier surface, especially at a grid spacing of 150 m, and after biases are removed.

Finally, while ASTER imagery usually generates good DEMs and velocity maps, images should be scrutinized before use. Images with clouds, low sun elevations, high

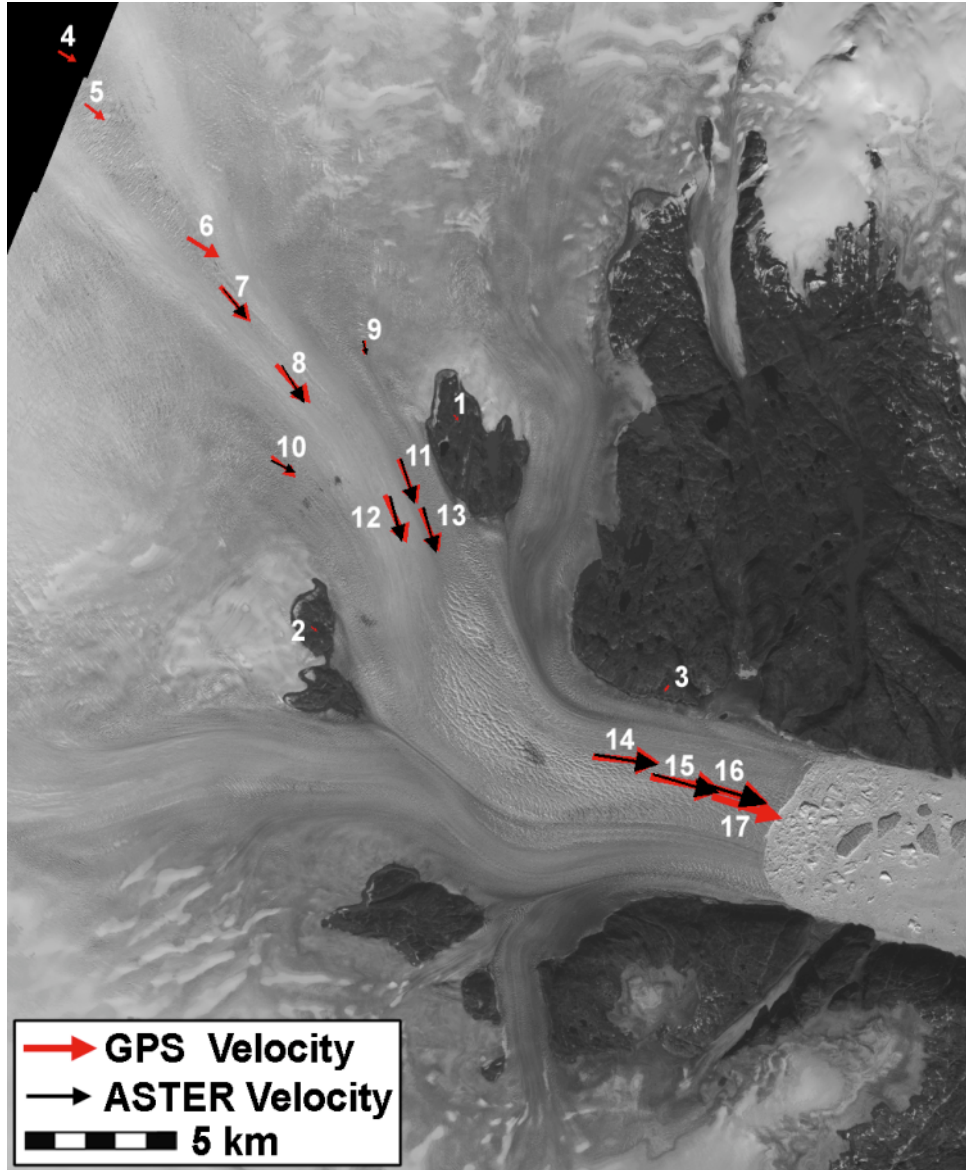


Figure 2.7. The velocity vectors of GPS (red) and ASTER-derived (black) data. ASTER velocities for sites 4 – 6 and 17 are not available. Sites 1 – 3 are rock sites.

pointing angles, or poor radiation balances will not produce good results. Systematic biases between DEMs do occur, and DEMs should be validated over static points (e.g., bedrock) to test their relative geo-location and elevations. This is especially true when using ASTER DEMs to detect changes in elevation on glaciers. Given the error budget, ASTER DEMs are probably only valid when glacier elevation changes are greater than  $\sim 25$  m over 5 years.

## Chapter 3

# RECENT DYNAMICS OF FOUR LARGE EAST ANTARCTIC OUTLET GLACIERS

### 3.1 Introduction

Large outlet glaciers and ice streams are the primary means by which ice is transported from the interior of Antarctica to the ocean (*Rignot and Thomas*, 2002). Changes in the flow configuration of these outlet glaciers control ice sheet mass balance and sea level. Several recent studies (e.g., *Payne et al.*, 2004; *Rignot and Kanagaratnam*, 2006; *Thomas*, 2004) have highlighted rapid increases in outlet glacier speeds in both Greenland and Antarctica, implying that the near-term contribution to sea level from ice sheets is underestimated by current models.

Outlet glaciers are known to change speed on a range of timescales. Some of the best studied examples are ice streams in West Antarctica, which change speed on timescales ranging from days (*Bindschadler et al.*, 2003) to decades (e.g., *Joughin et al.*, 2003; *Stearns et al.*, 2005b) to centuries (e.g., *Retzlaff et al.*, 1993). Rapid increases in the flow speed of outlet glaciers draining the Greenland Ice Sheet have also been observed in the last four years. The occurrence of similar types of behavior on large outlet glaciers of the East Antarctic Ice Sheet (EAIS) south of  $\sim 81.5^{\circ}\text{S}$  is largely unknown because most satellite sensors cannot image that far south. In the absence of observations, these glaciers are often assumed to be in steady state flow regimes (e.g., *Rignot and Thomas*, 2002).

Here, we study the ice dynamics of four glaciers draining ice from the East Antarctic Ice Sheet through the Transantarctic Mountains into the Ross Embayment: David Glacier ( $75.3^{\circ}\text{S}, 162^{\circ}\text{E}$ ), Mulock Glacier ( $79^{\circ}\text{S}, 160.5^{\circ}\text{E}$ ), Byrd Glacier ( $80^{\circ}\text{S}, 160^{\circ}\text{E}$ ), and Nimrod Glacier ( $82.5^{\circ}\text{S}, 160.2^{\circ}\text{E}$ ) (Figure 3.1). Together, these glaciers drain  $\sim 1,500,000 \text{ km}^2$ , or  $\sim 12\%$  of the entire Antarctic Ice Sheet. We quantify changes in ice velocity, surface elevation and mass balance to assess their stability, and examine force balance characteristics to understand the controls on their flow.

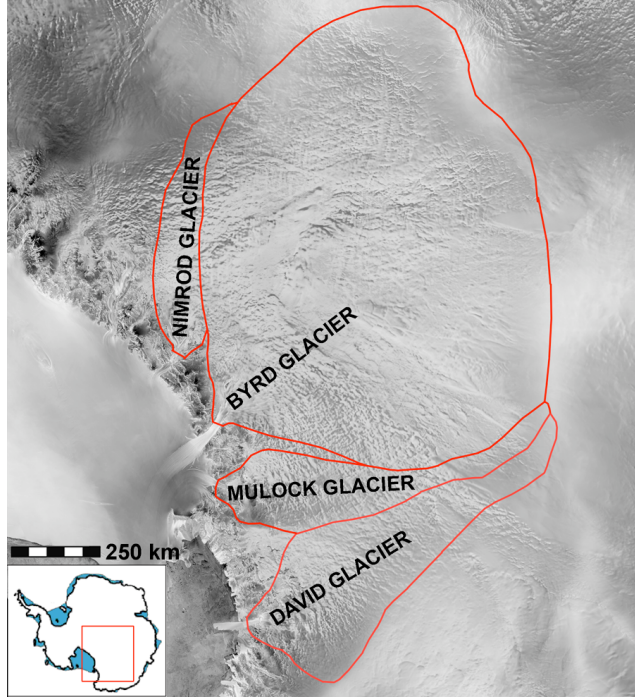


Figure 3.1. Catchment boundaries for East Antarctic outlet glaciers studied in this paper, overlaid on a portion of the Radarsat mosaic.

## 3.2 Data

For each glacier, we determine ice velocities and surface elevations using remote sensing techniques. Temporal changes in velocity and elevation are quantified using repeat satellite images and, where available, archival field data.

### 3.2.1 Velocity

Spatially extensive and multi-temporal ice velocity data do not exist for these outlet glaciers (Figure 3.1) due to challenging field logistics and limited satellite coverage south of  $\sim 81.5^{\circ}\text{S}$ . Here, we use Advanced Spaceborne Thermal Emission and Reflection Radiometer (ASTER) imagery to derive new surface velocity measurements of four glaciers draining from the East Antarctic Ice Sheet into the Ross Embayment (Figure 3.1). The ASTER sensor is well-suited for mapping glaciers at high latitudes because it images at high resolution (15m ground resolution in the VNIR bands) with coverage to  $\sim 84^{\circ}\text{N/S}$ .

We also use Landsat TM and ETM+ imagery, where available, to extract velocity measurements on glaciers north of  $\sim 81.5^{\circ}\text{S}$ .

To obtain ice velocities, we apply a cross-correlation technique (*Scambos et al.*, 1992) to sequential images to track the displacement of surface features such as crevasses. Cloud-free, co-registered and ortho-rectified image pairs are input into the cross-correlation software, and operator-controlled settings allow for a range of displacement patterns. The technique is described in detail in Chapter 2.

Uncertainties in the feature tracking technique originate from errors in ortho-rectification, co-registration, and the cross-correlation technique. These errors are usually small and well-constrained for the application to ASTER imagery. Velocity errors are variable because of the different time separation of each image pair. In all cases, combined errors are small compared with the observed speeds.

Archival velocity measurements exist for some of the glaciers in this study. In 1960 – 1962, *Swithinbank* (1963) measured surface displacement on Mulock, Byrd and Nimrod glaciers, using traditional theodolite measurements. Surveys of each glacier consist of one transverse profile, with 6 – 21 surveyed points. *Brecher* (1982) used repeat aerial photographs of Byrd Glacier, acquired on December 6, 1978 and January 31, 1979, to calculate the displacement of 472 points on the trunk of Byrd Glacier. Velocity measurements, derived from remote-sensing and field-based GPS, on David Glacier were collected between 1990 – 1994 by *Frezzotti et al.* (1998). Synthetic aperture radar interferometry (InSAR) was also used to measure ice velocities of David, Byrd, and Mulock glaciers in 1996 (*Rignot*, 2002; *Rignot and Thomas*, 2002).

### 3.2.2 Elevation Data

Surface elevation maps are produced from stereo ASTER imagery using the Japanese ASTER Science Team procedure described by *Fujisada et al.* (2005) and *Stearns and Hamilton* (2007). The ASTER sensor collects a stereo image-pair using two telescopes in visible band 3: a nadir-viewing telescope (3N), and a backward-looking telescope (3B). The individual ASTER scenes are converted to digital elevation models (DEMs) through process-

ing of the stereo bands to epipolar geometry, and parallax-matching using commercial software (*Fujisada et al.*, 2005). The final DEM product is referenced to the EGM96 geoid, and has a grid spacing of 15 m.

DEM uncertainties are from a combination of systematic errors, and random errors due to satellite positioning, image acquisition geometry, and atmospheric conditions. Each DEM was tested for a systematic bias with respect to the other DEMs of the same glacier. Those with a bias of more than  $\pm 10$  m were discarded. For the remaining DEMs, random errors contribute an elevation uncertainty of 20 m.

### 3.2.3 Bed Topography

Bed topography surveys are scarce along the Transantarctic Mountain outlet glaciers, and existing models (e.g., BEDMAP) rely on a linear interpolation of ice thickness at the grounding line to the closest measurement of bed topography in the upper basin (*Lythe et al.*, 2001). The resolution (5 km grid spacing), horizontal accuracy (200 m) and vertical accuracy (332 m) of the BEDMAP data along these glaciers is too coarse to be useful for mass balance and force budget calculations (*Liu et al.*, 1999; *Lythe et al.*, 2001). As a solution to this problem, we fit a 4th order polynomial to cross-sections of the valley-walls, extracted from the ASTER DEMs. The cross-sections were spaced at 1 – 2 km intervals along each glacier. Fitting a polynomial to the slope of the valley walls is a geomorphological technique used to characterize glaciated U-shaped troughs and fjords (e.g., *Graf*, 1970). Where ice thickness data exist from airborne radio-echo sounding (e.g., Byrd Glacier), the polynomials are constrained by the measured bed elevations. Where ice thickness measurements do not exist, the minimas of the polynomials are constrained by BEDMAP estimates. These derived bed topographies are rough approximations of the glaciated fjords gridded at 1 km spacing, but are probably more realistic than existing models (e.g. BEDMAP) for this part of East Antarctica.

Ice thickness is calculated as the difference between surface elevations derived from ASTER DEMs and the derived bed topography. An uncertainty of 20 m is applied to the

elevation data and an uncertainty of 100 m is applied to the ice thickness data (*Bamber et al.*, 2000).

### 3.2.4 Accumulation Rates

Snow accumulation is probably one of the most difficult mass balance parameters to constrain. There are roughly 2000 surface mass balance measurements over the whole 13 million km<sup>2</sup> Antarctic Ice Sheet (*Magand et al.*, 2007), or approximately one measurement every 6,500 km<sup>2</sup>. Several continental-scale compilations have been produced (e.g., *Arthern et al.*, 2006; *Giovinetto and Zwally*, 2000; *Van de Berg et al.*, 2006; *Vaughan et al.*, 1999), using field measurements and atmospheric re-analyses models or remote sensing data.

For our mass balance estimates, we are interested in extracting from these compilations the amount of accumulation per catchment basin. Catchment basins are delineated by mapping changes in surface slope on the OSU DEM of Antarctica (*Jezek et al.*, 1999; *Liu et al.*, 1999) and tracing flow lines and stripes on Radarsat imagery. *Price and Whillans* (1998) assign an uncertainty of 9% to catchment basin areas, using traditional surveying techniques. Using higher-resolution satellite-derived DEMs and imagery, we estimate an uncertainty of 5% in our catchment basin areas.

## 3.3 Spatial and Temporal Changes in Ice Velocity and Surface Elevation

Mapping glacier velocities and surface elevations is an important first step in assessing glacier stability and mass balance conditions. In Greenland and West Antarctica, large and rapid changes in flow dynamics are often preceded by long-term thinning (*Krabill et al.*, 2004; *Shepherd et al.*, 2001; *Thomas et al.*, 2003). Baseline data—sets of surface elevation and flow velocity are required to accurately detect future changes and interpret their causes. In East Antarctica, like most of the polar regions, baseline datasets are rare. These records are constructed for the first time for several large outlet glaciers.

### 3.3.1 David Glacier

David Glacier ( $75.3^{\circ}\text{S}$ ,  $162^{\circ}\text{E}$ ) drains ice from northern Victoria Land through the Transantarctic Mountains and into the Ross Sea (Figure 3.2A). It is the only glacier in this study that is not buttressed by the Ross Ice Shelf, but rather feeds into the Drygalski Ice Tongue. The ice tongue extends  $\sim 90$  km into a polynya in Terra Nova Bay, which is kept free of sea ice by the force and persistence of katabatic winds (Kurtz and Bromwich, 1983). Previous analyses of flow speeds on David Glacier show that they increase, almost linearly, from the grounding line to the edge of the Drygalski Ice Tongue (Frezzotti, 1993; Wuite, 2006).

The trunk of David Glacier begins as ice flows over David Cauldron, a bedrock step that is evident in both satellite imagery (Figure 3.2A) and surface topography (Figure 3.2B). The glacier loses  $400 - 500$  m of elevation in David Cauldron, which causes rapid, but isolated, flow acceleration (Figure 3.2C). Down-flow of David Cauldron, the surface slope flattens and ice flow decreases. The glacier accelerates again as the tributary at  $x = 10,000$  m joins the main trunk. Throughout the main trunk of David Glacier, flow speed is much slower at the lateral margins, indicating lateral drag from the rock walls.

Frezzotti *et al.* (1998) identify the grounding line of David Glacier (Figure 3.3A) from an analysis of tidal cycles in high-rate GPS measurements carried out at eight locations along the glacier and the Drygalski Ice Tongue. Rignot (2002) located the grounding line  $\sim 15$  km up-flow, based on tidal flexure detected using interferometry; these results place the grounding line at the base of the David Cauldron (Figure 3.3A).

Existing mass budget estimates for David Glacier indicate that it is close to zero balance (Frezzotti, 1993; Rignot, 2002), with small differences in the estimates arising from variability between the available accumulation maps. Satellite radar altimetry maps for the period 1992 – 2003 show slight thickening ( $2.1 \pm 0.4$  mm yr $^{-1}$  (Davis *et al.*, 2005) and  $1 \pm 2$  mm yr $^{-1}$  (Wingham *et al.*, 2006)) averaged throughout the whole catchment. However, thinning of  $2 - 4$  mm yr $^{-1}$  is detected over the trunk of David Glacier during this time period (Davis *et al.*, 2005). Our analysis of repeat ASTER DEMs yields results (Figure 3.3) that are consistent with the altimetry, although the uncertainties are larger.

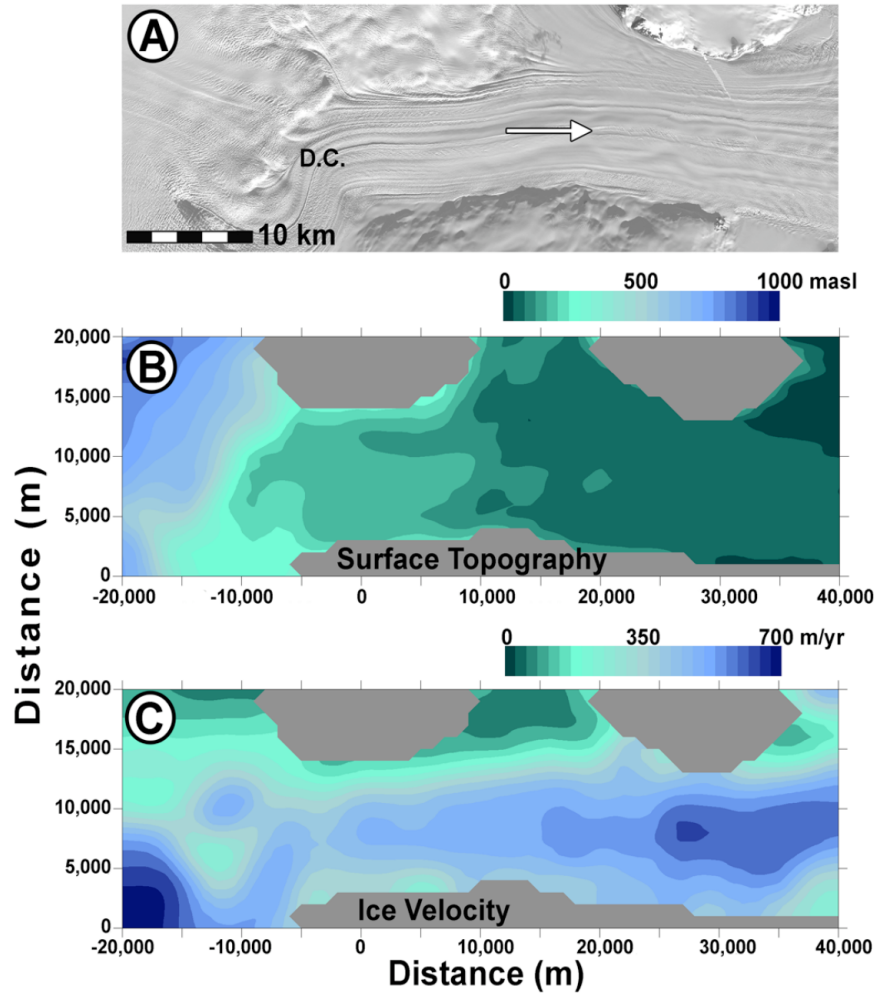


Figure 3.2. David Glacier: A) ASTER satellite image from 12/12/2004. The David Cauldron (D.C.) is the steep drop to the left of the image. The arrow indicates the direction of ice flow. B) Surface topography derived from the ASTER image in panel A) and gridded to 1 km. The valley walls have been masked, and are represented by grey shading. C) Ice velocity determined from an ASTER image pair (01/17/2001 – 10/14/2001) and gridded to 1 km.

We compare our ASTER-derived velocities (2001 – 2006) with earlier results from Landsat TM images (*Frezzotti et al.*, 1998), radar imagery from 1991 – 2000 (*Wuite*, 2006), and several GPS sites surveyed in 1991 and 1994 (*Frezzotti et al.*, 1998). Flow speeds are within 15% of each other (Figure 3.3B) and generally within the respective errors, suggesting no significant changes in speed over the 16 year period. Ice velocity in 1990 seems slightly higher (Figure 3.3B) than in subsequent years, but with the current timeseries it

is difficult to assess if this is measurement error, or the end of a period of faster flow. Overall, the steady flow conditions are consistent with zero mass balance inferred from altimetry (*Davis et al.*, 2005; *Wingham et al.*, 2006).

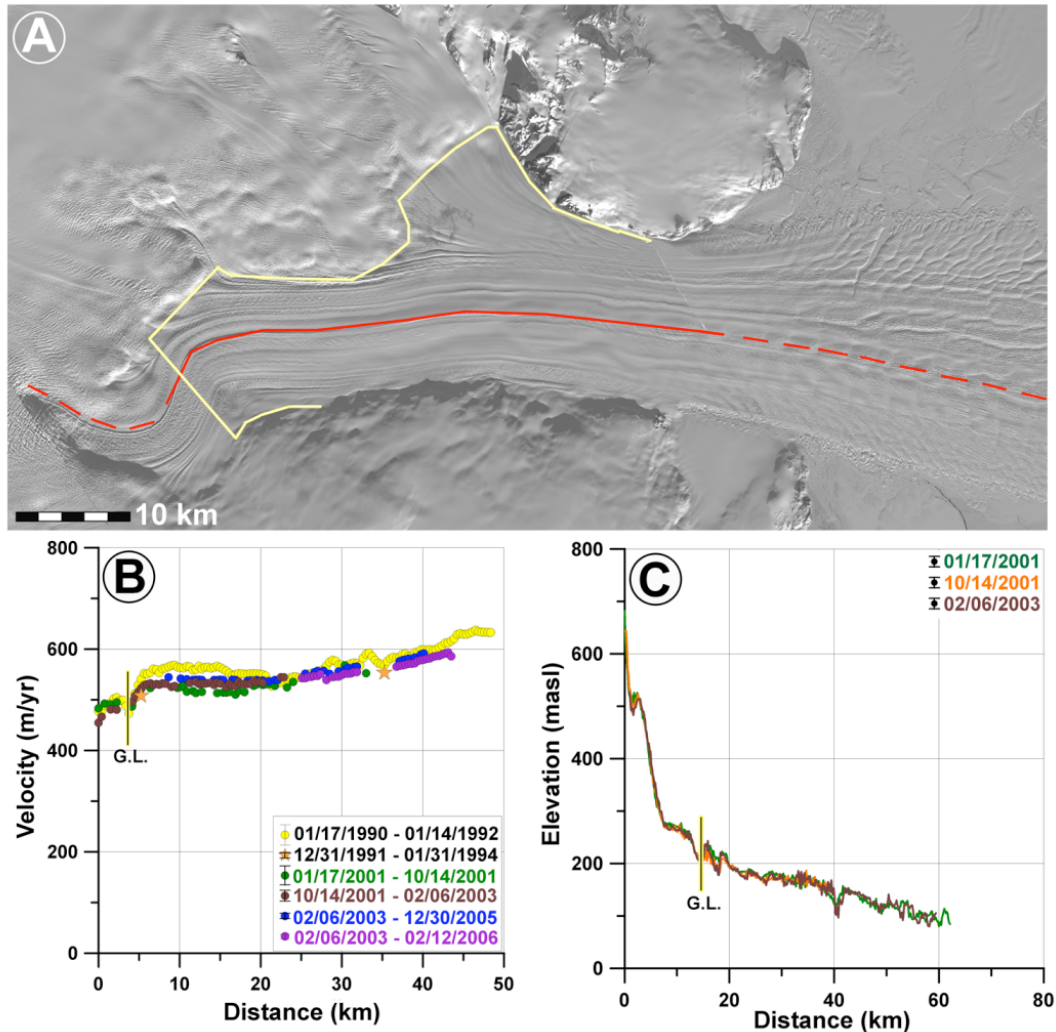


Figure 3.3. David Glacier: A) ASTER satellite image from 12/12/2004. The yellow line represents the grounding line (G.L.) determined by *Rignot* (2002). B) Ice velocity derived from field surveys and repeat Landsat (*Frezzotti et al.*, 1998) and ASTER images for three epochs along the solid red line in panel A. Orange stars represent 1991 – 1994 GPS velocities from *Frezzotti et al.* (1998). C) Surface elevation from ASTER DEMs, along the dashed red line in panel A.

### 3.3.2 Mulock Glacier

Mulock Glacier ( $79^{\circ}\text{S}$ ,  $160.5^{\circ}\text{E}$ ) drains the largest catchment basin between David Glacier and Byrd Glacier. It is buttressed by the Ross Ice Shelf, and drains  $8.2 \pm 7.6 \text{ km}^3 \text{ yr}^{-1}$  of ice from East Antarctica into the ice shelf (Rignot and Thomas, 2002). The geometry of Mulock Glacier is shown in Figure 3.4. Here, the glacier has been rotated  $40^{\circ}$  to orient ice flow along the  $x$ -axis, and to isolate the along- and across-flow components of ice motion, which simplifies subsequent strain rate and force balance calculations.

The main trunk of Mulock Glacier is  $\sim 60 \text{ km}$  long (Figure 3.4A) and undergoes a  $\sim 1000 \text{ m}$  drop in elevation from the edge of the East Antarctic Ice Sheet to the grounding line where it enters the Ross Ice Shelf (Figure 3.4B). The ASTER-derived DEM shows large changes in surface concavity, most notably at  $x = 0$  and  $20,000 \text{ m}$  (Figure 3.4B). These changes in surface profile are most likely a function of flow across the over-deepened basin at  $x = -10,000 \text{ m}$  (Figure 3.4C). Ice flow accelerates to accommodate discharge through a constriction in the fjord, and again as ice flows over a step (at  $x = \sim 25,000 \text{ m}$ ) into the Ross Ice Shelf (Figures 3.4D). The sharp peak in velocity  $\sim 50 \text{ km}$  down the flowline (Figure 3.5B) is most likely due to the increase in surface slope that is visible on the satellite image (Figure 3.5A) and surface elevation profile (Figure 3.5C). The location of the grounding line (at  $x = 50,000 \text{ m}$ ) is determined on the basis of crevasse patterns (Figure 3.5A), ice-flow (Figure 3.5B) and surface elevation changes (Figure 3.5C).

Geodetic measurements from 1960 – 1961 yielded ice velocities of  $\sim 387 \text{ m yr}^{-1}$  along the grounded centerline of the glacier (Figure 3.5B) (Swithinbank, 1963). Results from repeat feature tracking, while not overlapping the same location, infer comparable ice speeds, 40 years after the Swithinbank (1963) study (Figure 3.5B). The more recent pattern of velocities, mapped using satellite imagery, seems to show a gradual acceleration at the grounding line from  $457 \pm 10 \text{ m yr}^{-1}$  (from images on 10/20/2001 and 11/23/2002) to  $481 \pm 8 \text{ m yr}^{-1}$  (from images on 01/26/2003 and 12/31/2005), to  $493 \pm 20 \text{ m yr}^{-1}$  (from images on 04/05/2006 and /3/08/2007). The average acceleration along the trunk of the glacier is  $11.2 \pm 4.9 \text{ m yr}^{-2}$  between 2001 and 2003, and  $6.0 \pm 4.6 \text{ m yr}^{-2}$  between image pairs in 2005 and 2006.

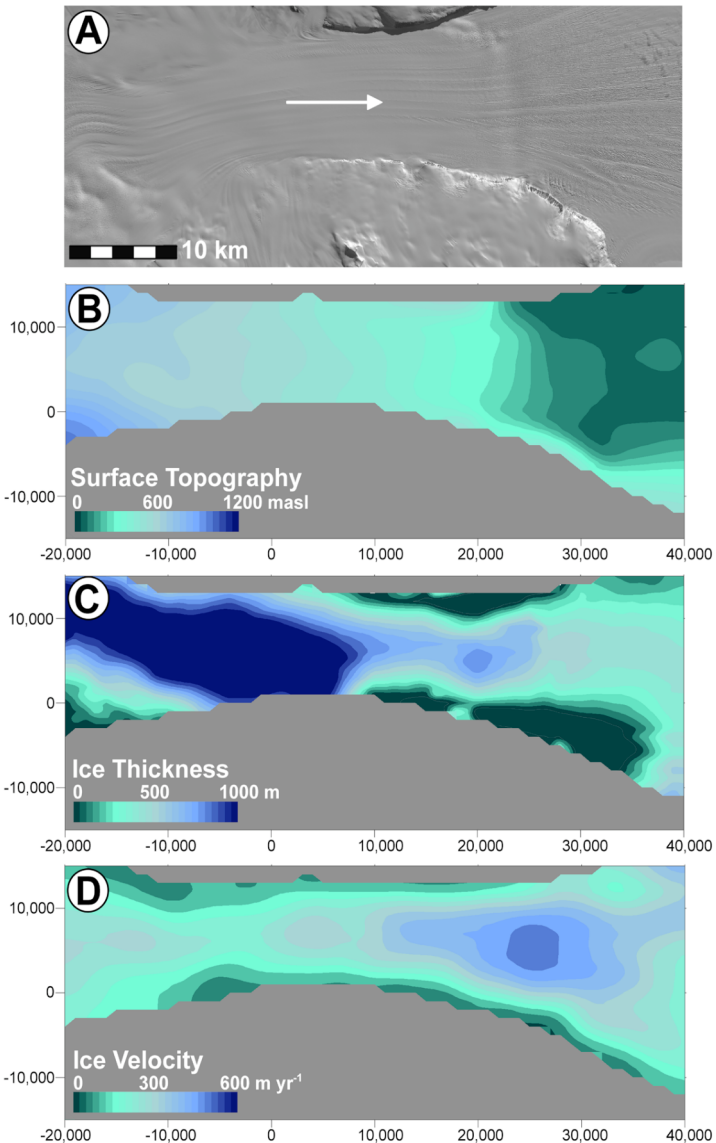


Figure 3.4. Mulock Glacier. A) ASTER satellite image from 11/23/2002, rotated by 40°. Ice flow follows the arrow direction. B) Surface topography derived from the ASTER image in panel A) and gridded to 1 km spacing. C) Ice thickness also gridded to 1 km spacing. D) Ice velocity from an ASTER image pair (10/20/2001 – 11/23/2002), gridded to 1 km spacing.

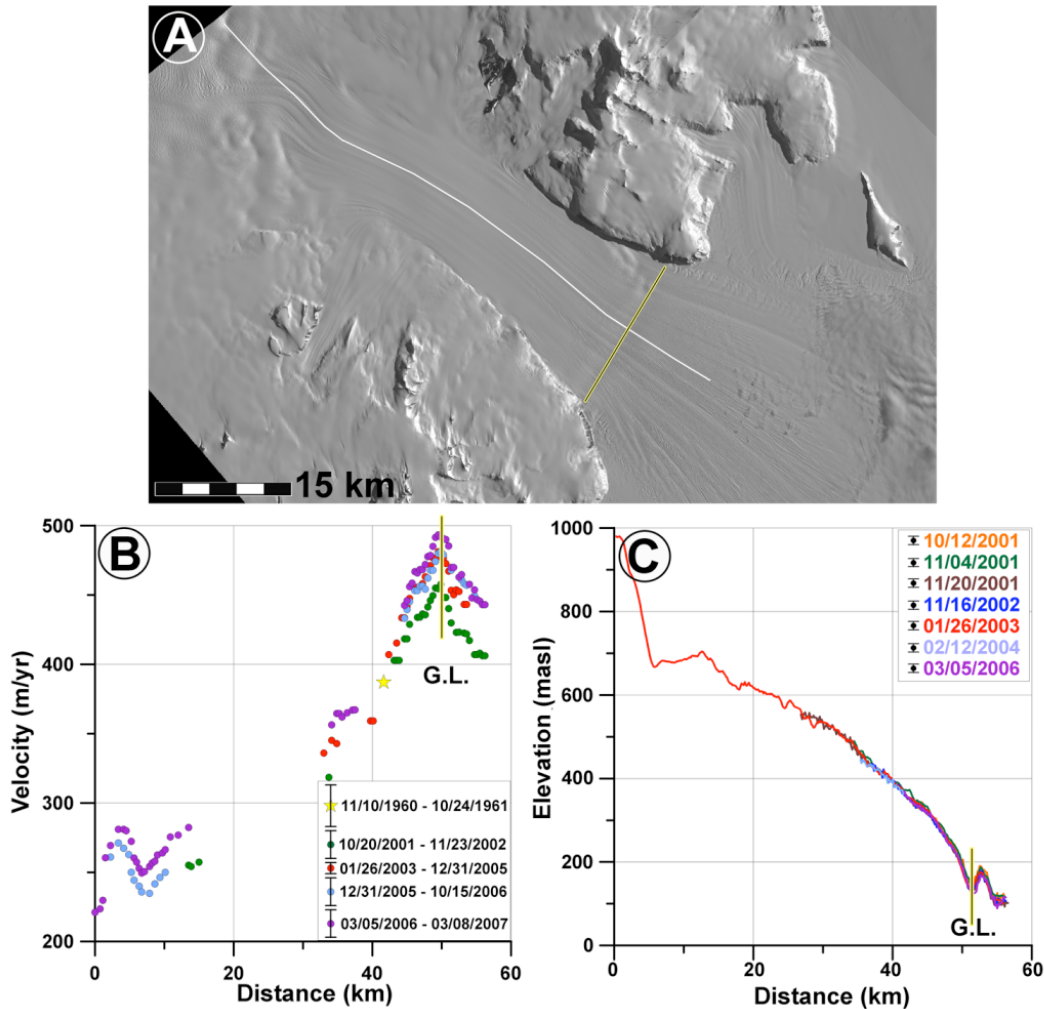


Figure 3.5. Mulock Glacier: A) ASTER satellite image from 11/23/2002. The yellow line represents the grounding line (G.L.), inferred from panels B and C. B) Ice velocity derived from repeat ASTER images for four epochs along the white line in panel A. The yellow star denotes repeat geodetic measurements by *Swithinbank* (1963). C) Surface elevation from ASTER DEMs, along the white line in panel A.

Mulock Glacier shows no change in surface elevation from 2001 – 2006 (Figure 3.5C). Multiple profiles are included for 2001 to illustrate the repeatability of ASTER DEMs (Figure 3.5C). If the velocity increases are real, we would expect some dynamic thinning of the glacier, but the uncertainties in DEM elevation are too large to detect this effect.

### 3.3.3 Byrd Glacier

Byrd Glacier has one of the largest catchment basins in Antarctica ( $1,070,400 \text{ km}^2$ ) (*Rignot and Thomas, 2002*), delivers  $23.6 \pm 2 \text{ km}^3 \text{ yr}^{-1}$  of ice into the Ross Ice Shelf (*Rignot and Thomas, 2002*), and sustains rapid flow speeds. Prolonged changes in the flow dynamics of Byrd Glacier will impact the mass balance of East Antarctica and might also affect the stability of the Ross Ice Shelf. Because of its size and importance, Byrd Glacier is one of the few East Antarctic outlet glaciers with a history of study.

Byrd Glacier is shown in Figure 3.6. In these figures, the glacier has been rotated  $-35^\circ$  (counterclockwise) to orient the dominant flow along the  $x$ -axis. The local coordinate system matches Whillans and Van der Veen (1993), so that  $x = 0$  falls approximately where Brecher (1982) located the grounding line. There is a switch in surface profile, from convex to concave, as the glacier approaches the grounding line (Figure 3.6B), which Reusch and Hughes (2003) show occurs  $\sim 1100 \text{ m}$  below sea level. The grounding line might be prone to up-glacier retreat because of high basal melt rates ( $12 - 15 \text{ m yr}^{-1}$ ) along the floating part of Byrd Glacier (*Kenneally and Hughes, 2004*), a process that has been observed on other glaciers with floating tongues (*Rignot, 2001; Rignot and Jacobs, 2002*).

A  $\sim 10 \text{ km}$ -wide grounding zone was first identified by Hughes (1986), who detected tidal fluctuations at 15 surface elevation markers along the centerline of Byrd Glacier, using traditional surveying techniques. Instead of a sharp grounding line, there was a gradual shift from floating to grounded ice (Hughes, 1986). In this study, we identify the grounding line (Figure 3.7A) on the basis of changes in surface velocity and elevations (Figures 3.7B, C). Its location is near the middle of the grounding zone identified by Hughes (1986).

Byrd Glacier is the only glacier in this study that has ice thickness data from airborne surveys conducted along the central flow-line in 1972 (Drewry, 1983). These data are used to constrain the interpolated ice thicknesses, gridded in Figure 3.6C at 1 km spacing. Byrd Glacier has large over-deepenings at  $x = -25,000$  and  $-40,000 \text{ m}$  (Hughes, 1979). Ice velocity peaks near the grounding line, and is concentrated towards the northern

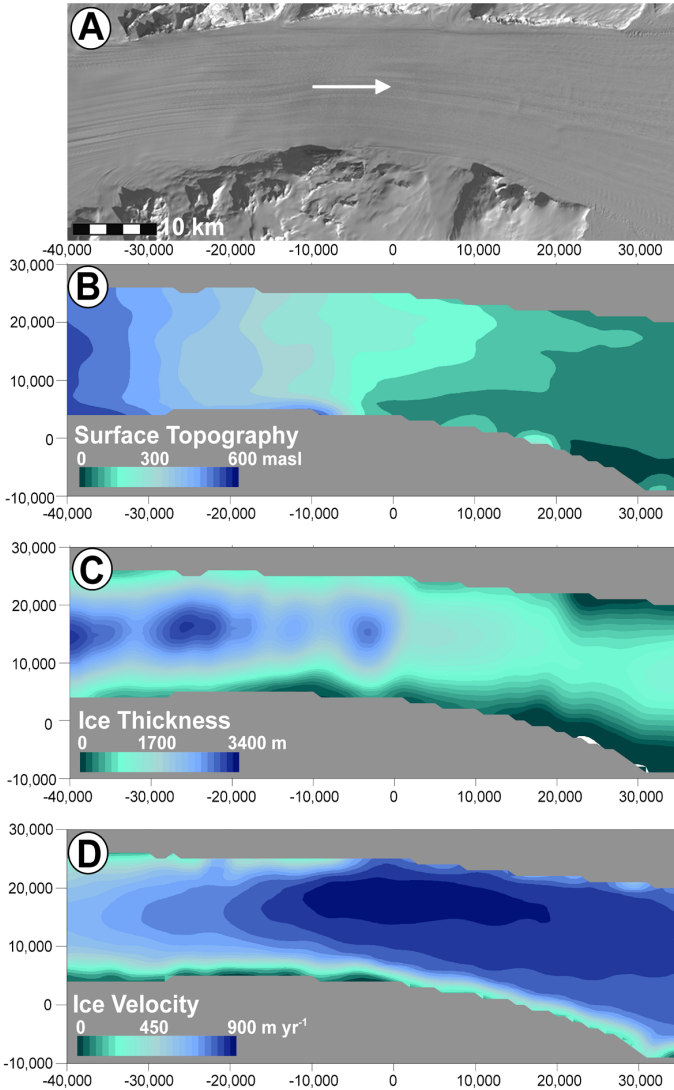


Figure 3.6. Byrd Glacier. A) Landsat satellite image from 01/20/1990, rotated by  $-35^\circ$ . B) Surface topography derived from an ASTER image on 01/29/2001 and gridded to 1 km. C) Ice thickness also gridded to 1 km spacing. D) Ice velocity from an ASTER image pair (12/05/2005 – 01/28/2007), gridded to 1 km spacing.

margin of the glacier (Figure 3.6D). *Swithinbank* (1963) and *Brecher* (1982) describe similar patterns of velocity.

The spatial pattern of ice velocity (Figure 3.7B) can be explained by along-flow changes in surface topography (Figure 3.7C). Ice velocity increases steadily along-flow in response to increases in surface slope (Figure 3.7C), reaching a maximum at the grounding

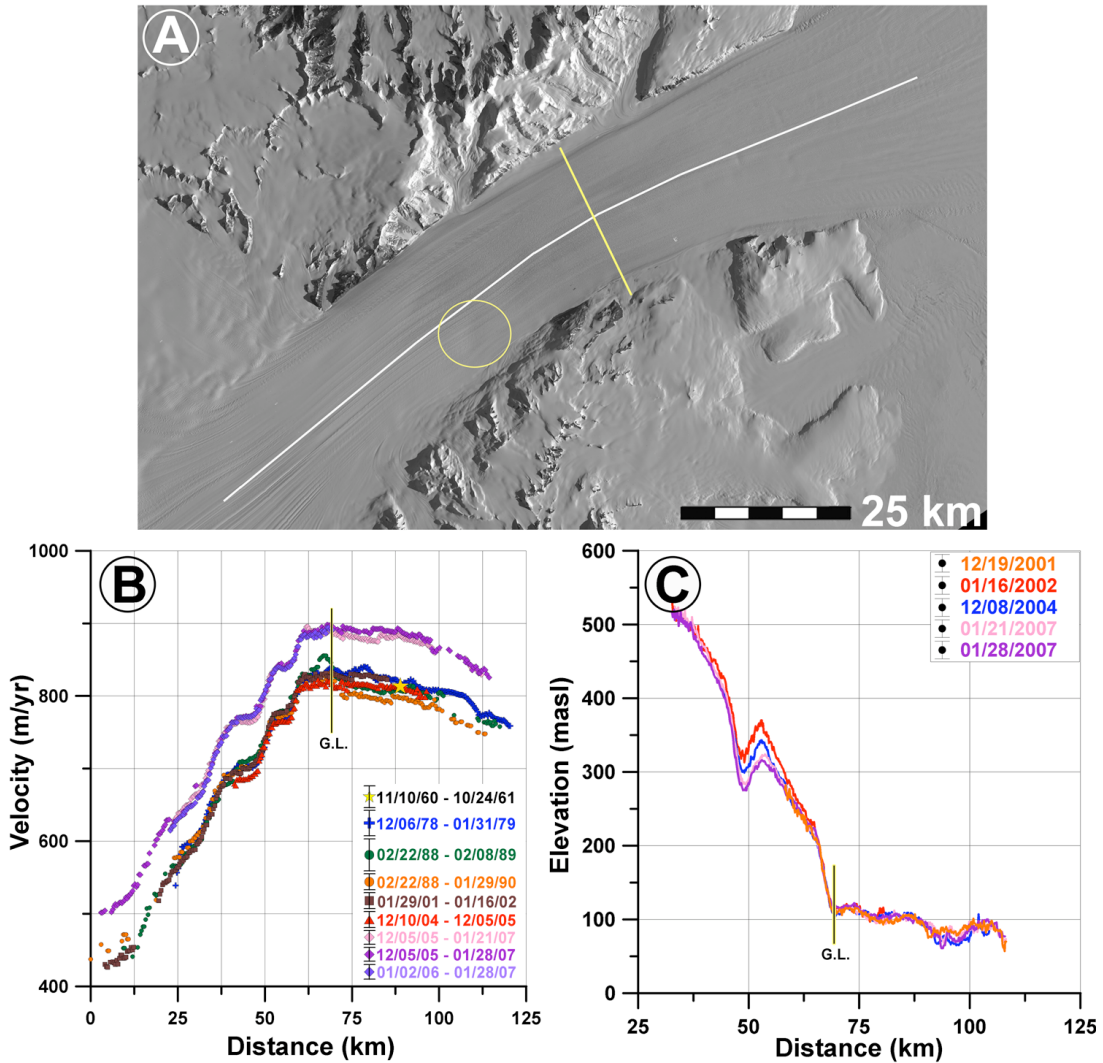


Figure 3.7. Byrd Glacier: A) Landsat satellite image from 01/29/1990. Ice flow is from left to right. The yellow line represents the grounding line (G.L.), located by Brecher (1982). The yellow circle identifies the 'bump' in panel C. B) Ice velocity derived from repeat geodetic measurements in 1960–1961 (Swithinbank, 1963), photogrammetry in 1978–1979 (Brecher, 1982), Landsat (1988–1990) and ASTER images (2001–2007) along the white line in panel A. C) Surface elevation from ASTER DEMs, along the white line in panel A. The 'bump' at  $x = 50$  km, is located in panel A.

line. Ice velocity begins to decrease where linear flow switches to diverging shelf flow as the floating ice enters the Ross Ice Shelf.

There appears to be a recent change in the pattern of flow behavior on Byrd Glacier. Measurements from geodetic surveys (Swithinbank, 1963), repeat photogrammetry (Brecher,

1982), and satellite imaging techniques imply that flow speeds did not change between 1960 and 2005 (Figure 3.7B). Feature tracking performed on ASTER images acquired between December 2005 and January 2007 show accelerated flow speeds. The speed-up extends from the floating tongue to  $> 75$  km inland (Figure 3.7B). The nearly-simultaneous acceleration over a long distance raises the possibility of a systematic bias in one or all of the recent images. No evidence of a bias was found. Moreover, the velocity accelerations are present in independent pairs of images, leading us to conclude that the change in flow speed is real.

Thinning on Byrd Glacier is isolated to a ‘bump’ at  $x = 50$  km at a rate of  $10.8 \pm 4.9$  m  $\text{yr}^{-1}$  between 2002 and 2004, and  $4.2 \pm 6.6$  m  $\text{yr}^{-1}$  between 2004 and 2007 (Figure 3.7C). There does not appear to be thinning downstream of the grounding line between 2001 and 2007 according to our differencing of ASTER DEMs. Schenk *et al.* (2005) detect thinning of 10–30 m on the floating part of the glacier by comparing 1978 elevations from photogrammetry (Brecher, 1982) with 2004 elevations from ICESat. Assuming a constant rate of change, we would expect 2.4–7.2 m of elevation change over the period covered by the ASTER DEMs, which is too small to be detected by our method.

### 3.3.4 Nimrod Glacier

Nimrod Glacier ( $82.5^\circ\text{S}$ ,  $160.2^\circ\text{E}$ ) consists of two tributaries which merge  $\sim 50$  km from the Ross Ice Shelf (Figure 3.8A). Each panel in Figure 3.8 is transformed to a local coordinate system, where the origin is near the grounding line and the  $x$ -axis is horizontal and mainly down-flow (after a rotation of  $-30^\circ$ ). These contour plots show surface elevation and velocity gridded to 1 km. The DEM of Nimrod Glacier reveals steep slopes on the tributaries and flatter gradients farther down-glacier (Figure 3.8B). Valley walls reduce the width of the glacier by  $\sim 45\%$  just below the confluence of the tributaries. This sudden narrowing causes a noticeable increase in velocity from  $\sim 400$  m  $\text{yr}^{-1}$  to almost 800 m  $\text{yr}^{-1}$  (Figure 3.8C). Velocity decreases as the glacier widens (Figure 3.8D) and its slope decreases in the down-flow direction (Figure 3.8B).

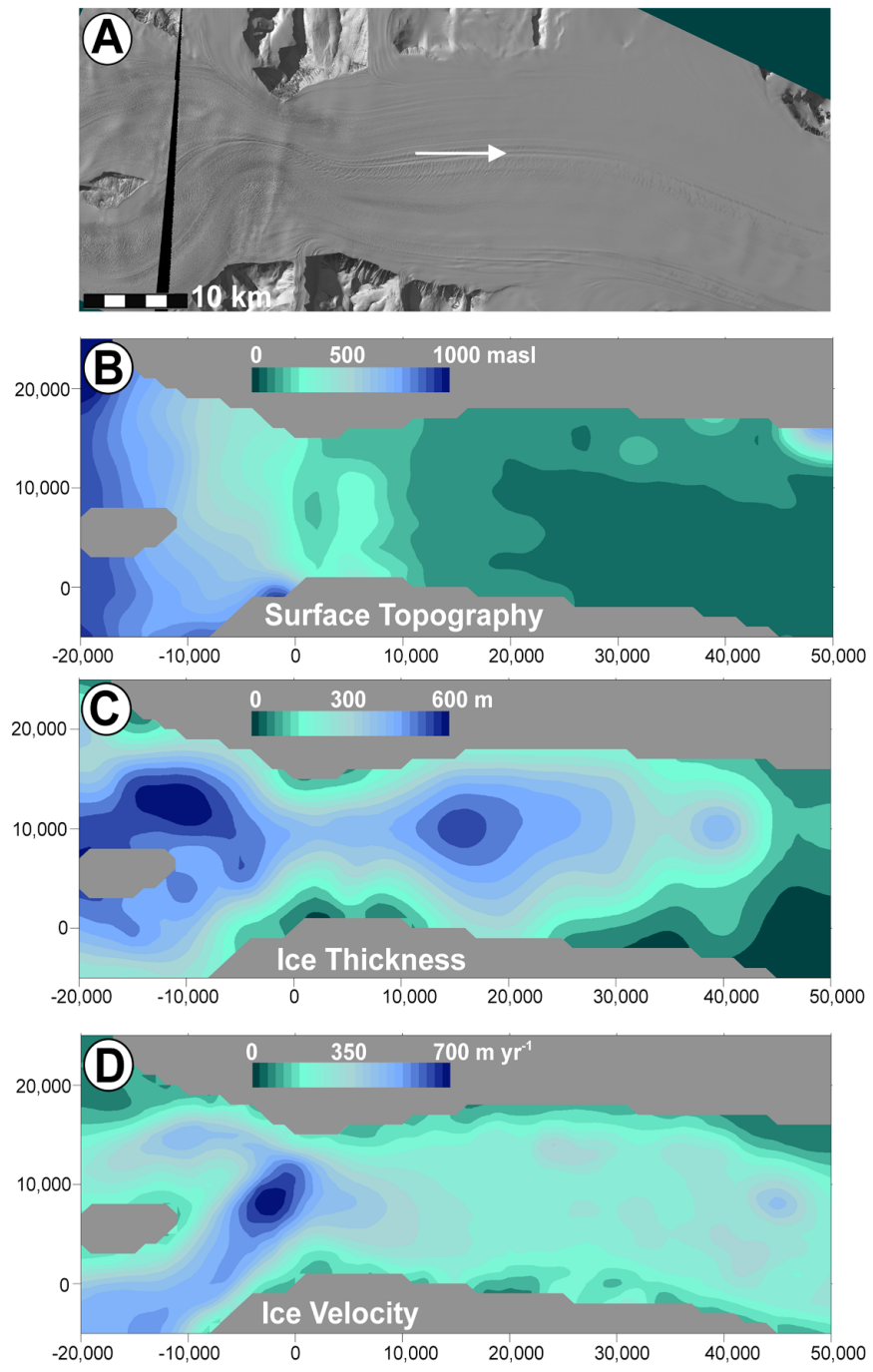


Figure 3.8. Nimrod Glacier. A) ASTER satellite image from 01/21/2001, rotated by  $-30^\circ$ . B) Surface topography derived from the ASTER image in panel A) and gridded to 1 km. C) Ice thickness also gridded to 1 km spacing. D) Ice velocity from an ASTER image pair (01/28/2001 – 11/21/2001), gridded to 1 km.

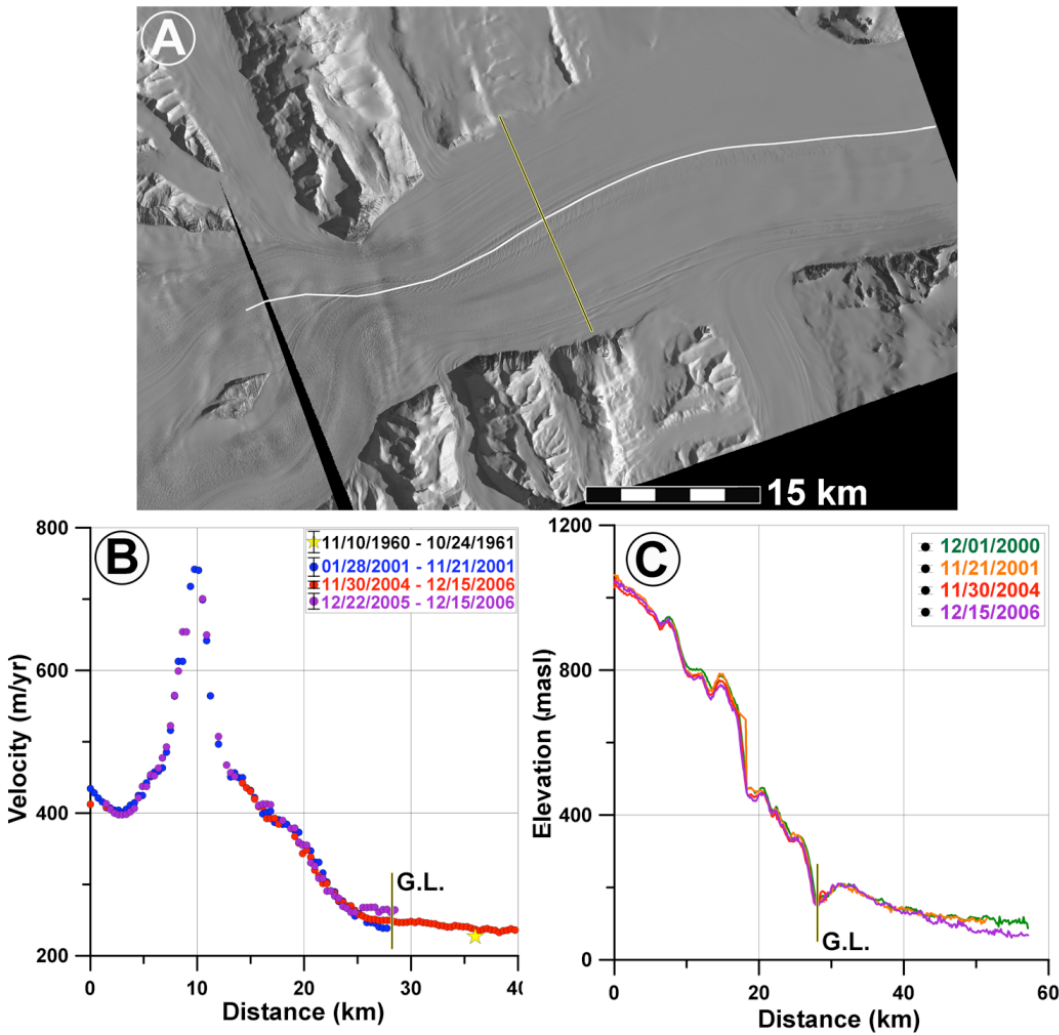


Figure 3.9. Nimrod Glacier: A) Landsat satellite image from 11/21/2001. The yellow line represents the grounding line (G.L.), inferred from velocity and elevation results in panels B and C. B) Ice velocity derived from repeat geodetic measurements in 1960 – 1961 by *Swithinbank* (1963) and ASTER imagery from 2001 to 2006. C) Surface elevation from ASTER DEMs, along the white line in panel A.

Raw data (un-gridded and in a geographic coordinate system) show no temporal changes in ice speed on Nimrod Glacier. *Swithinbank* (1963) conducted geodetic measurements on the floating portion of Nimrod Glacier in 1960 – 1961. His results are not significantly different (Figure 3.9) from velocity measurements derived from an ASTER image pair on 11/30/2004 – 12/15/2006, which is the only pair to overlap with his survey line. Ice velocity does not appear to change between 2001 and 2006, except for a

slight acceleration from  $238 \pm 13 \text{ m yr}^{-1}$  to  $264 \pm 11 \text{ m yr}^{-1}$  at the grounding line (Figure 3.9B).

The surface elevation of the ground portion of Nimrod Glacier did not change in the past 6 years (Figure 3.9C). Past the grounding line, there appears to be slight ( $12.6 \pm 4.7 \text{ m yr}^{-1}$ ) thinning between 2000 and 2006. The available DEM data do not allow us to conclude whether the thinning initiated or resulted from the observed flow acceleration.

## 3.4 Force Budget

### 3.4.1 Theory

Insight into the large-scale mechanisms controlling glacier motion can be obtained from calculations of the stresses that drive and resist flow. Resistance can come from the bed, the sides, or from along-flow obstacles. Changes over time in the velocity field of a glacier should be explained by a subsequent change in the balance of forces controlling the flow.

We employ the force budget technique described by *Van der Veen and Whillans* (1989) to calculate forces at depth using measurements of surface velocity and estimates for surface slope and ice thickness. In the following analysis, it is convenient to align the  $x$ -axis so it is positive down-flow (right), the  $y$ -axis is positive across-flow (up) and the  $z$ -axis is vertically up. We first calculate the strain rate for each of three components of the strain rate tensor,  $\dot{\varepsilon}_{xx}$ ,  $\dot{\varepsilon}_{yy}$ ,  $\dot{\varepsilon}_{xy}$ , which describe longitudinal stretching, lateral spreading and shearing at the glacier surface, respectively. Vertical strain,  $\dot{\varepsilon}_{zz}$ , is deduced from the condition of incompressibility, in which

$$\dot{\varepsilon}_{xx} + \dot{\varepsilon}_{yy} + \dot{\varepsilon}_{zz} = 0 . \quad (3.1)$$

Vertical shear strain rates,  $\dot{\varepsilon}_{xz}$ ,  $\dot{\varepsilon}_{yz}$ , are ignored because we assume the stresses are independent of depth. The effective strain rate,

$$\dot{\varepsilon}_e^2 = \frac{1}{2}(\dot{\varepsilon}_{xx}^2 + \dot{\varepsilon}_{yy}^2 + \dot{\varepsilon}_{zz}^2) + \dot{\varepsilon}_{xy}^2 + \dot{\varepsilon}_{xz}^2 + \dot{\varepsilon}_{xy}^2 \quad (3.2)$$

describes the general pattern of deformation over the glacier.

Surface velocity gradients are related to deviatoric stresses,  $\sigma'_{ij}$ , by using Glen's flow law, which states

$$\sigma'_{ij} = B\dot{\varepsilon}_e^{(\frac{1}{n})-1}\dot{\varepsilon}_{ij}. \quad (3.3)$$

where  $n = 3$ , and the stiffness parameter,  $B$ , is set to  $500 \text{ kPa yr}^{-1/3}$ , appropriate for ice at  $-15^\circ\text{C}$  (*Hooke*, 1981), the integrated ice-temperature for Byrd Glacier (*Whillans et al.*, 1989). Resistive forces are calculated from the deviatoric stresses, such that

$$\begin{aligned} R_{xx} &= 2\sigma'_{xx} + \sigma'_{yy}, \\ R_{yy} &= 2\sigma'_{yy} + \sigma'_{xx}, \\ R_{zz} &= 0, \\ R_{xy} &= \sigma'_{xy}. \end{aligned} \quad (3.4)$$

The driving stress,  $\tau_{dx}$ , is given by the usual formula

$$\tau_{dx} = -\rho g H \frac{\partial h}{\partial x} \quad (3.5)$$

where the density of ice,  $\rho$ , is held constant at  $917 \text{ kg m}^{-3}$ , gravitational acceleration,  $g$ , is  $9.8 \text{ m s}^{-2}$ , ice thickness is  $H$ , and surface elevation is  $h$ .

Resistive stresses can come from the bed (basal drag), from the sides (lateral drag), or from along-flow obstacles (longitudinal gradients). Our procedure is to use a simple block-flow model (*Van der Veen and Whillans*, 1989) to resolve the stress gradients across the glacier. The force balance equation

$$\tau_{dx} = \tau_{bx} - \left( \frac{\partial}{\partial_x} HR_{xx} \right) - \left( \frac{\partial}{\partial_y} HR_{xy} \right) \quad (3.6)$$

shows that driving stress is balanced by basal drag, and by gradients in longitudinal stress and lateral drag, hereafter  $F_{long}$  and  $F_{lat}$  respectively. The driving stress,  $F_{lat}$  and  $F_{long}$  are calculated from surface measurements (following Equations 3.2 – 3.5) while basal drag is the residual needed to balance Equation 3.6. Evaluating Equation 3.6 allows us to identify the fraction of the driving stress that is resisted dynamically by the glacier (expressed as gradients in depth-averaged lateral and longitudinal drag) as opposed to friction at the bed of the glacier.

The local coordinate system places the  $x$ -axis along the southern (bottom) margin of each glacier, positive in the main direction of flow. The driving stress is always positive, as is basal drag. (Negative values for basal drag are not realistic and are likely a function of the simple block flow model. Similar artifacts of reverse basal drag are also noted in force balance calculations on Whillans Ice Stream (*Whillans and Van der Veen, 1993*), Bindschadler Ice Stream (*Price et al., 2002*), and Byrd Glacier (*Whillans et al., 1989*).) Variations in lateral drag,  $\frac{\partial}{\partial_y} HR_{xy}$ , stem from lateral shearing,  $\frac{\partial u_x}{\partial y}$ , or flow turning,  $\frac{\partial u_y}{\partial x}$ . Lateral stresses are negative when they are resisting flow. In a few isolated cases, lateral drag is positive, usually because of flowline turning. Similarly, longitudinal stresses can either resist ( $F_{long} < 0$ ) or enhance ( $F_{long} > 0$ ) flow.

### 3.4.2 Application

The force balance equations are applied to gridded datasets of surface velocity and ice thickness for David, Mulock, Byrd and Nimrod glaciers. The feature tracking technique yields at least 10,000 velocity data points per image pair, once obvious blunders (mostly due to clouds or seams in image mosaics) are removed. These vectors are irregularly distributed and so we use kriging to map them onto a regular 1 km grid. Surface elevation and ice thickness data are kriged to the same grids.

Glacier	Image 1	Image 2
David Glacier	01/17/2001	10/14/2001
Mulock Glacier	10/20/2001	11/23/2002
Byrd Glacier	12/06/1978 02/22/1988 01/29/2001 12/05/2005	01/31/1979 01/29/1990 01/16/2002 01/28/2007
Nimrod Glacier	01/28/2001	11/21/2001

Table 3.1. Velocity pairs used for the force balance study in section 3.5.

Data is transformed to local coordinate systems for each glacier, to simplify the force balance results. The origin and rotation of the coordinate system is listed in Table 3.2.

Glacier Name	Latitude	Longitude	Rotation
Byrd Glacier	80.50°S	159.00°E	-35°
David Glacier	75.40°S	161.20°E	0°
Mulock Glacier	79.00°S	159.50°E	+40°
Nimrod Glacier	82.55°S	161.00°E	-30°

Table 3.2. Origin and rotation angles of glaciers used in the force balance analysis.

### 3.4.3 Errors

Uncertainties in the force budget technique derive from measurement errors, gridding errors, and simplifying assumptions in the force balance equations (*Price et al., 2002*). Uncertainties in measured and derived quantities are listed in Table 3.3. In particular, large uncertainties in ice thickness, arising from sparse bed elevation measurements along East Antarctic outlet glacier troughs, propagate through many equations. Velocity errors are specific to individual image pairs, but are generally unimportant, being less than  $30 \text{ m yr}^{-1}$ . Surface slope, strain rate and driving stress uncertainties are calculated using measurement errors for surface elevation, velocity and ice thickness, respectively.

The simplifying assumptions inherent in the force balance method are an additional source of uncertainty. Equation 3.6 is valid only if surface velocities are constant through the whole ice thickness. This assumption is reasonable because the high velocities of

Variable	Symbol	$1\sigma$
Surface Elevation (m)	$h$	20
Ice Thickness (m)	$H$	100
Velocity ( $\text{m yr}^{-1}$ )	$U$	$\leq 30$
Surface Slope ( $\text{m m}^{-1}$ )	$\alpha$	$\leq .002$
Strain Rate ( $\text{yr}^{-1}$ )	$\varepsilon_{ij}$	$\leq .042$
Driving Stress (kPa)	$\tau_d$	$\leq 30$
Rate Factor ( $\text{kPa yr}^{1/3}$ )	$B$	105

Table 3.3.  $1\sigma$  uncertainties for variables used in the force balance calculation. The maximum uncertainty of the four glaciers is displayed (values may be lower for individual glaciers).

the EAIS outlet glaciers imply that basal sliding is large, and that the depth-averaged velocities are similar to surface velocities (*Price et al.*, 2002).

Converting surface strain rates to deviatoric stresses (Equation 3.3) requires an estimate for  $B$ , the temperature-dependent ice stiffness parameter. Here, we use a rate factor for a depth-averaged temperature of  $-15^\circ\text{C}$ , based on an approximated surface temperature of  $-25^\circ\text{C}$  (*Scofield et al.*, 1991; *Whillans et al.*, 1989). We assign an uncertainty of 30% to the value for  $B$ , after *Price et al.* (2002). An inaccurate value for  $B$  will not affect the spatial distribution of stresses, but it will affect the overall magnitude.

### 3.5 Spatial and Temporal Changes in Force Balance

#### 3.5.1 David Glacier

David Glacier sustains high driving stresses of  $300 \pm 30 \text{ kPa}$  as it flows down the steep gradient of David Cauldron (Figure 3.10). Here, over 90% of the driving stress is resisted by basal drag, with slight (5 – 10 kPa) resistance from lateral and longitudinal stress gradients. Peaks in lateral drag occur near where the southern tributary flows into David Glacier, narrowing the main trunk. Large variations in longitudinal stress gradients and basal drag may be due to sticky spots, but could also be artifacts of inaccurate ice thickness along David Glacier. Near the grounding line, all stress components approach zero. These patterns are consistent with force balance maps derived from satellite radar image velocities in 1997 – 2000 (*Wuite*, 2006), indicating no dynamic change in the lower reaches

of David Glacier in the past decade. This result is consistent with the continued presence of the Drygalski Ice Tongue.

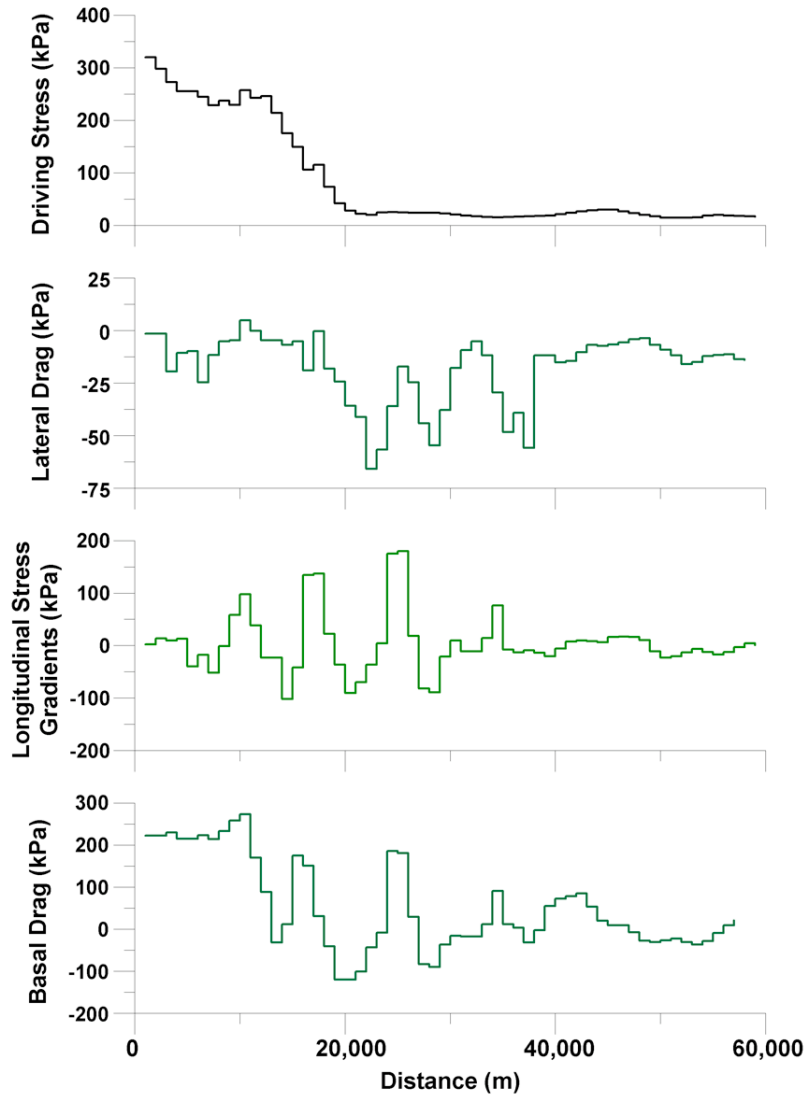


Figure 3.10. David Glacier. Components of the force balance equation derived from 2001 velocities and plotted at 1 km spacing.

### 3.5.2 Mulock Glacier

On Mulock Glacier, the driving stress reaches three maxima of  $\geq 100$  kPa, corresponding to locations where surface slope and ice thickness are both large (Figure 3.11A). Driving stresses on Mulock Glacier are lower than the other glaciers in this study, probably

because of prescribed ice thicknesses. No direct measurements of ice thickness exist and our inferred ice thickness values may be too low, which would affect the magnitude of the stresses. Gradients in lateral drag,  $F_{lat}$ , are negative along the centerline and positive at the margins (Figure 3.11B), typical for a glacier that is undergoing shearing in the across-flow direction (e.g., *Price et al.*, 2002; *Whillans et al.*, 1989).  $F_{lat}$  provides  $\sim 25$  kPa of resistance along most of the glacier, except where the glacier narrows by  $\geq 5$  km and  $F_{lat}$  reaches  $\sim 50$  kPa. As Mulock Glacier floats and flow diverges into the Ross Ice Shelf,  $F_{lat}$  approaches zero (Figure 3.11B).

Longitudinal stress gradients,  $F_{long}$ , are generally small ( $\sim 25$  kPa), except at the bulls-eye features near  $x = 0$  (Figure 3.11C). Here, changes in ice thickness and along-flow ice velocity form a pattern of extension and compression. The variability of  $F_{long}$  is closely correlated to perturbations in surface slope and driving stress. The bulls-eye features of extension and compression (Figure 3.11C) are probably due to bedrock bumps (cf., *Price et al.*, 2002; *Whillans et al.*, 1989). As ice flows over a bump, the surface slope and driving stress are high, causing longitudinal stretching ( $F_{long} > 0$ ). Downstream of a bump there is compression ( $F_{long} < 0$ ). Since variations in  $F_{long}$  mirror those of the driving stress (high values of both occur on bedrock bumps),  $F_{long}$  essentially dampens variations in basal drag (*Budd*, 1970).  $F_{long}$  is much reduced over the floating portion of Mulock Glacier, but still exists due to buttressing forces from the Ross Ice Shelf (Figure 3.11C).

Basal drag is the residual needed to balance the sum of the driving stress and gradients in lateral and longitudinal stress. Most of the trunk of Mulock Glacier experiences 50 – 100 kPa of basal drag. Basal drag peaks in areas where there is a reverse bed slope (e.g.,  $x = 7,000$  m and  $x = 20,000$  m). The overall force balance of Mulock Glacier suggests that basal drag is the dominant resistive force (50 – 100 kPa), while gradients in lateral (15 – 25 kPa) and longitudinal stress (15 – 25 kPa) provide additional, but smaller, amounts of resistance to flow.

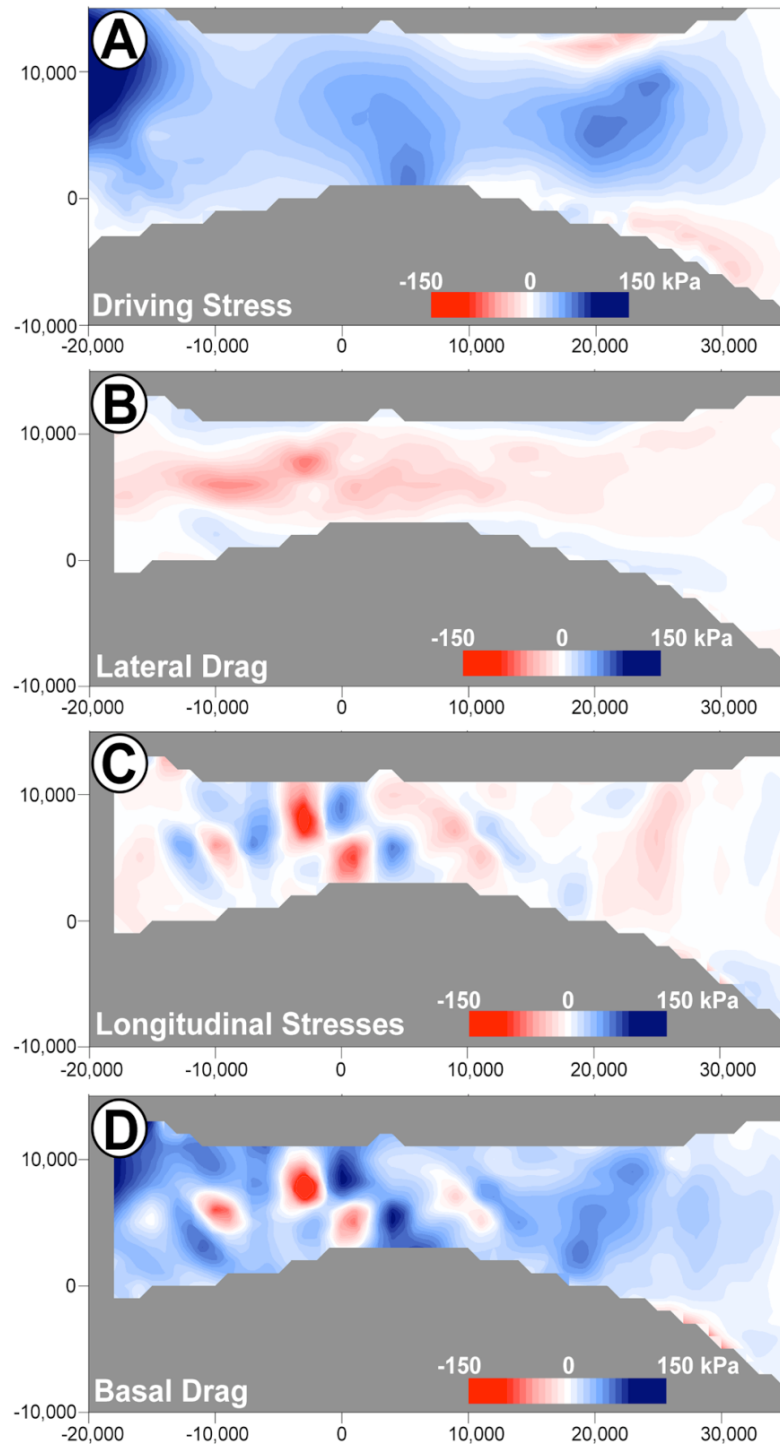


Figure 3.11. Mulock Glacier. Components of the force balance equation 3.6, gridded to 1 km. A) Driving stress, B) gradients in lateral drag, C) gradients in longitudinal stresses, D) basal drag.

### 3.5.3 Byrd Glacier

Driving stresses on Byrd Glacier reach values  $>200$  kPa on the upper portions of the glacier and directly up-flow of the grounding line (Figure 3.12A). These high values are primarily the result of a bedrock over-deepening (e.g., *Scofield et al.*, 1991) and high surface slopes (Figure 3.6). The driving stress remains below 20 kPa on the floating portion of the glacier, because of low surface slopes. Values of negative driving stress ( $\sim -10$  kPa) are probably artifacts of the ice thickness data, and are within the error estimate. The large scale patterns of driving stress are consistent with those mapped by *Whillans et al.* (1989).

Gradients in lateral drag on Byrd Glacier present minimal resistance to flow. Lateral drag throughout most of the glacier trunk ranges from  $-25$  to  $-50$  kPa, with isolated peaks of  $-100$  kPa (Figure 3.12B). A small amount of lateral drag ( $\sim -10$  kPa) persists beyond the grounding line, probably because the trunk is still confined by the valley walls.

Longitudinal stresses range from  $-100$  to  $50$  kPa on Byrd Glacier, indicating both compressional and extensional flow (Figure 3.12C). Prominent 'bulls-eye' features, ranging from  $\pm 100$  kPa, occur throughout the trunk, especially where surface slope gradients are high. A steep surface slope will cause the local driving stress to be higher than in areas with gentler slopes. This causes increased stretching upstream from the bump, essentially "pulling" the ice in the downstream direction ( $F_{long} > 0$ ) (e.g., *Price et al.*, 2002). When the surface slope decreases, compression ( $F_{long} < 0$ ) occurs. We see high extensional stresses up-stream of the surface 'bumps' at  $x = 25,000$  m and  $x = 35,000$  m in Figure 3.13. This variability in  $F_{long}$  implies that flow on Byrd Glacier is affected by variations in bed topography. Alternatively, *Reusch and Hughes* (2003) suggest that the wave-like pattern of longitudinal stress gradients has no clear relationship to the bed topography and represents regular variations in ice–bed coupling. Unfortunately the bed topography data are not continuous and gaps in the dataset prohibit further analysis of the ice–bed relationship.

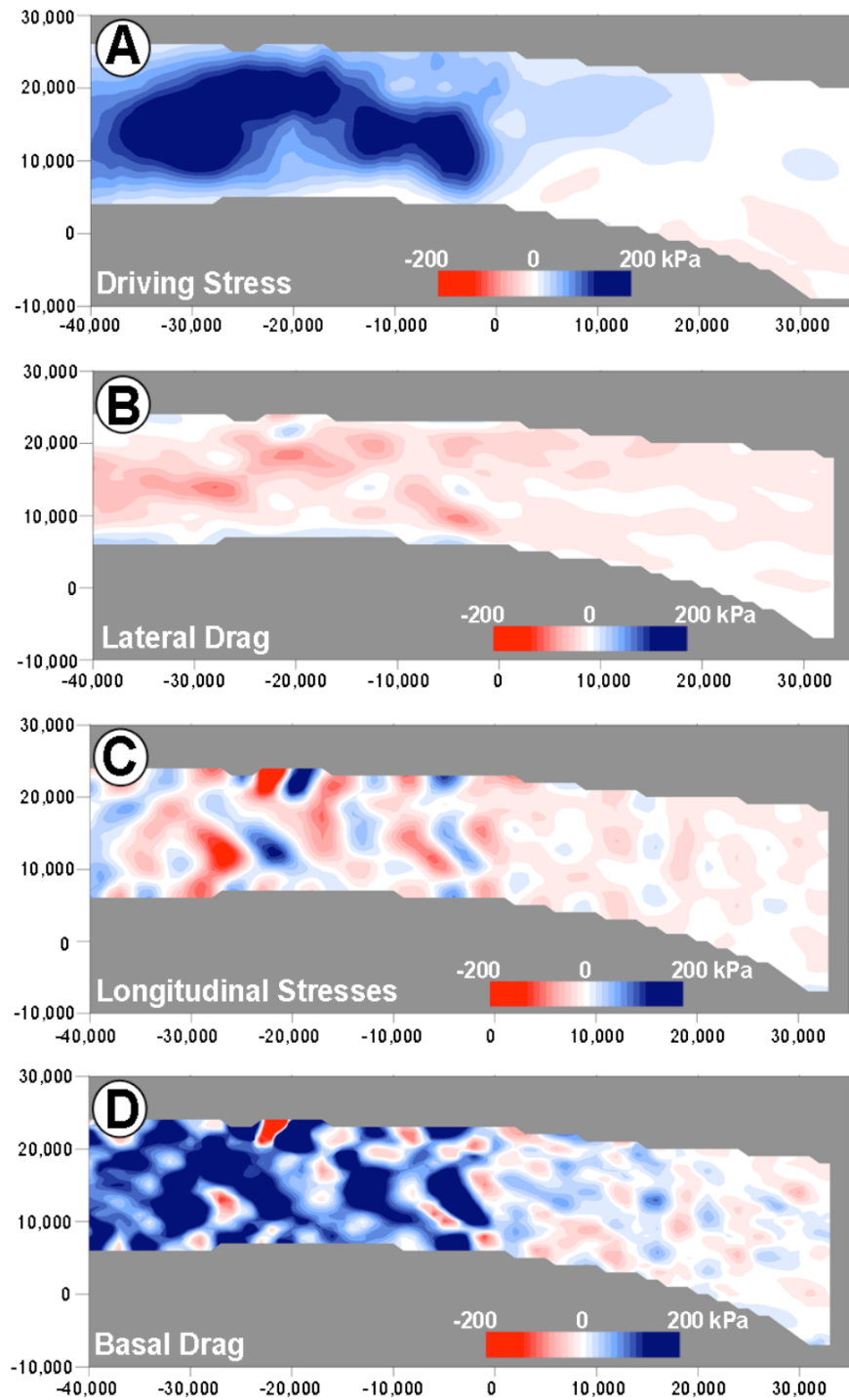


Figure 3.12. Byrd Glacier. Components of the force balance equation (Equation 3.6), gridded to 1 km. A) Driving stress, B) gradients in lateral drag, C) gradients in longitudinal stresses D) basal drag.

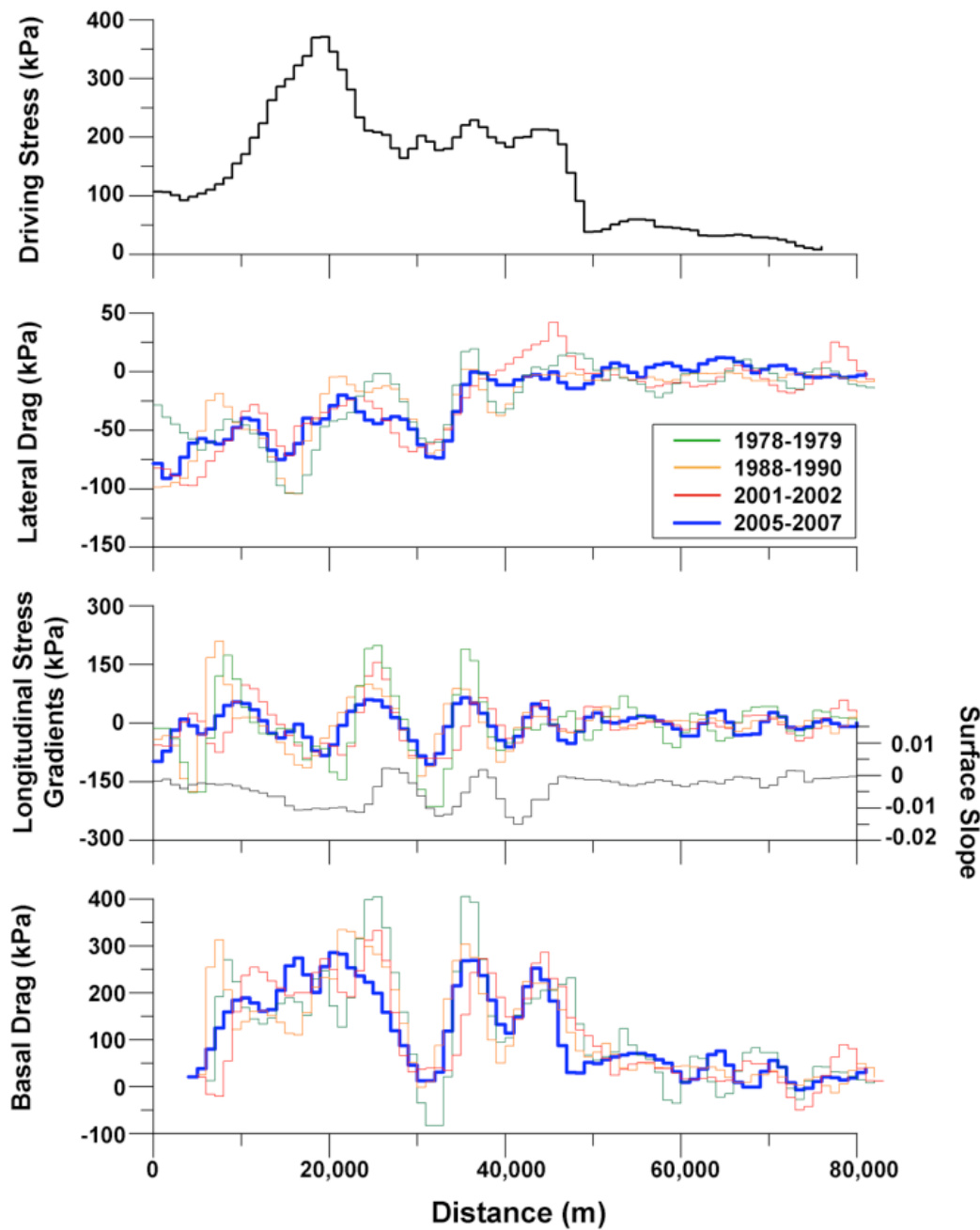


Figure 3.13. Individual forces for Byrd Glacier along an 80 km profile (flowing from left to right), for four velocity epochs.

Basal drag is  $\sim 150$  kPa along most of the trunk of Byrd Glacier (Figure 3.12D). Again, isolated areas of negative basal drag arise as a likely consequence of uncertain ice thickness estimates. The patchy character of basal drag suggests that there are isolated sticky

spots, a conclusion first reached by Whillans *et al.* (1989). Our results are similar in magnitude and pattern to those of Whillans *et al.* (1989), implying no change in the location of flow-resisting sticky spots from 1978 – 2005. Basal drag is the dominant resistant stress on Byrd Glacier, providing at least 70% of the resistance;  $F_{lat}$  provides  $\leq 20\%$  of resistance throughout the trunk of Byrd Glacier, while the contribution from  $F_{long}$  is variable, but averages  $\sim 10\%$ .

The force balance analysis was performed using four velocity epochs: 1978 – 1979 photogrammetry (Brecher, 1982), 1988 – 1990 (Landsat TM), 2001 – 2002 (ASTER) and 2005 – 2007 (ASTER). In all cases, driving stresses were derived from a 2005 ASTER DEM (for slope), and ice thickness obtained from a single flightline in 1972 (Drewry, 1983). While the calculations are not wholly independent of each other, we can use the results to search for temporal changes in the patterns of force balance. The results suggest a slight reduction in longitudinal stress gradients and basal drag in the 2005 – 2007 profile, compared with previous years (Figure 3.13). However, the stresses are derived from surface measurements, so acceleration requires the resistant forces to diminish to some degree.

The fast flow speeds of Byrd Glacier imply large basal velocities,  $u_b$ , and a substantial amount of water production at the ice–bed interface. Lubrication of the bed does not negate the contribution of basal drag, but supports the idea that basal drag is concentrated at isolated 'sticky spots'. Neglecting the effect of basal drag, a simple approximation for basal velocity is

$$u_b = u_s - \frac{2}{(n+1)} \left( \frac{\rho g \sin \alpha}{B} \right)^n H^{n+1}, \quad (3.7)$$

in which  $\alpha = \frac{\partial h}{\partial x}$ . We can then solve for the basal melt rate,

$$\dot{m} = \frac{G + \tau_b u_b - k_i \Theta_b}{L_i \rho_{ice}} \quad (3.8)$$

(Hooke, 2005, p. 190) where  $L_i$  is the latent heat of fusion ( $3.34 \times 10^5 \text{ J kg}^{-1}$ ) and  $k_i$  is the thermal conductivity for ice. The regional geothermal heat flux,  $G$ , is estimated to be between  $50 - 75 \text{ mW m}^{-2}$  (Maule *et al.*, 2005), which is three orders of magnitude smaller than the shear heating term,  $\tau_b u_b$ , and is thus omitted for simplicity. The basal temperature gradient,  $\Theta_b$ , is unknown and therefore neglected, meaning the numerator simplifies to  $\tau_b u_b$ , thus providing a maximum value for basal melt.

Calculated values of  $\dot{m}$  are shown in Figure 3.14. Basal melt rate averages  $0.26 \text{ m yr}^{-1}$  over the modeled region of the trunk, but isolated peaks of up to  $1.0 \text{ m yr}^{-1}$  occur in regions where basal drag and ice velocity are large. Negative values of basal melt are blunders that have propagated from falsely negative values in basal drag.

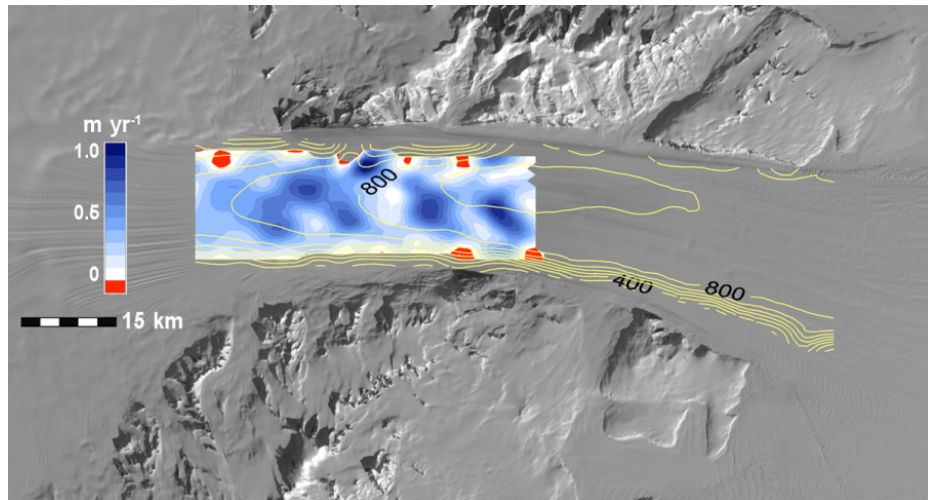


Figure 3.14. Calculated frictional melt rates ( $\text{m yr}^{-1}$ ) for Byrd Glacier, overlaid with velocity contours (each contour =  $100 \text{ m yr}^{-1}$ ).

### 3.5.4 Nimrod Glacier

Nimrod Glacier simultaneously narrows and flows down a steep gradient, leading to high ( $\sim 200 \text{ kPa}$ ) values of driving stresses (Figure 3.15). These stresses are resisted predominantly by basal drag, which resists  $\geq 90\%$  of the driving stress in the first 10 km of the flowline (Figure 3.15). Lateral drag provides  $\sim 10 - 20 \text{ kPa}$  of resistance throughout most of the glacier profile. Positive  $F_{lat}$  values past the grounding line indicate lateral spreading or flowline turning as the glacier enters the Ross Ice Shelf. Longitudinal

stresses alternate between extension and compression ( $F_{long} \pm 150$  kPa) across the steep gradient in the upper reaches of the glacier (at  $x = 0 - 20,000$  m), and approach zero past the grounding line (Figure 3.15). The large values of basal drag and longitudinal stress suggest that Nimrod Glacier, like the other Transantarctic Mountain glaciers, is flowing over a hard rock or non-deformable sediment bed.

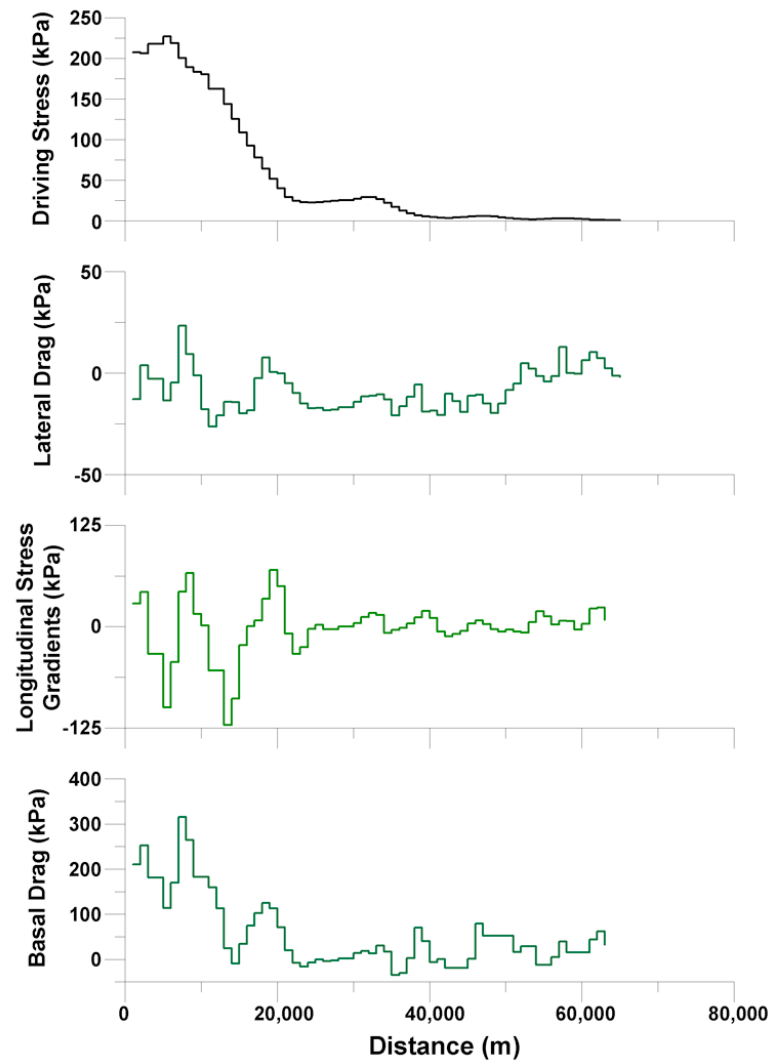


Figure 3.15. Components of the force balance equation, along an 80 km profile (flowing from left to right) for Nimrod Glacier, using velocity data from 2001.

### 3.5.5 Discussion

A force budget analysis reveals several common characteristics of the Transantarctic Mountain outlet glaciers. High driving stresses (100 – 300 kPa) cause fast flow as ice flows from the EAIS through the mountains. *Cooper et al.* (1982) were the first to note that driving stresses along East Antarctic outlet glaciers peak ~50 km from the grounding line, which coincides with steepening surface slopes and thickening ice. The dominant resistive stress in all studied cases is basal drag, suggesting that these glaciers are probably flowing over a rigid bed consisting of hard rock or non-deforming sediments. Additional resistance comes from lateral and longitudinal compression. Driving stresses reduce to ~10 kPa on the floating portions of the glaciers because of low surface gradients. Resistive stresses approach zero after the grounding line. Small values of lateral drag exist if the glacier is still bound by rock walls, or there is flowline turning as the glacier enters the Ross Ice Shelf. Longitudinal stresses are intermittently extensional (because of zero basal drag) and compressional components (because of buttressing from the Ross Ice Shelf), but the magnitude of these stresses is  $\leq 10$  kPa.

The glaciers investigated in this study have high driving stresses (~250 kPa), strong resistance from basal drag (~150 kPa), and minimal resistance from lateral drag (~50 kPa) and longitudinal compression (~50 kPa). Recent modeling by *Dupont* (2004) shows that glaciers with these characteristics are particularly sensitive to ice shelf (or ice tongue) perturbations. A force perturbation model by *Thomas* (2004) also suggests that these "quintessential outlet glaciers" (*Bentley*, 1987) are more sensitive to small force perturbations than the more active glaciers in Greenland. The sensitivity is partly due to the low longitudinal strain rates on the EAIS glaciers, which would allow perturbations to extend far inland, rather than adjusting the hydrostatic driving stress (through thickness and slope changes) to accommodate a change in velocity (*Thomas*, 2004).

## 3.6 Mass Balance

### 3.6.1 Application

The mass budget approach compares catchment-wide accumulation rates with ice flux across the grounding line. For a glacier in balance

$$\dot{M} = (\dot{b} * A_{catch}) - \dot{m} - (\bar{u} * A_{gl}) = 0 \quad (3.9)$$

in which  $\dot{b}$  is snow accumulation,  $A_{catch}$  is the catchment area,  $\dot{m}$  is the basal melt rate (from Equation 3.8),  $\bar{u}$  is the depth-averaged velocity, and  $A_{gl}$  is the cross-sectional area of the flux gate, usually taken to be at the grounding line.

Ice thickness at the grounding line, which is needed to determine  $A_{gl}$ , is calculated from hydrostatic equilibrium

$$h = (1 - \frac{\rho_{ice}}{\rho_{water}})H \quad (3.10)$$

in which  $h$  is the ice surface elevation above sea level, and  $\rho_{water}$  is the density of sea water, taken to be  $1,030 \text{ kg m}^{-3}$ .

We expect  $u_s \approx \bar{u}$ , at the grounding line because basal drag is zero. Our force balance analyses (Figure ??) show non-zero values for basal drag at the grounding lines. These non-zero values are largely the result of error in input parameters. Depth-averaged velocities calculated using these small values of basal drag are not significantly different from  $u_s$ , so our assumption of  $u_s \approx \bar{u}$ , is valid.

Mass loss from basal melting is an important balance term for fast-moving outlet glaciers where frictional energy dissipation at the bed can be significant (see Section 3.5.3). Calculated basal melt rates (from Equation 3.8) range from an average of  $6 \text{ mm yr}^{-1}$  w.e. for Mulock Glacier to  $260 \text{ mm yr}^{-1}$  w.e. for Byrd Glacier. The large variability between glaciers is a function of different flow speeds, and magnitudes of driving stress and basal drag (Mulock Glacier has a comparatively low driving stress). We compute  $\dot{m}$  only for the part of each glacier covered by our velocity maps, and only for the

grounded portions of the trunk. Melting underneath the floating portions of these outlet glaciers can be large ( $15 \pm 4 \text{ m yr}^{-1}$  for Byrd Glacier, and  $29 \pm 5 \text{ m yr}^{-1}$  for David Glacier) (Rignot and Jacobs, 2002), but are not relevant to our computations of mass balance because they occur downstream of the flux gates. We are not able to calculate melting in the upper accumulation area because it is outside the bounds of our velocity maps.

### 3.6.2 Results

The mass balance results for each glacier basin are listed in Table 3.4. Accumulation rates,  $\dot{b}$ , are from the surface mass balance compilation of *Van de Berg et al.* (2006). Basal melt rates are calculated following Equation 3.8. These are maximum estimates for melt rates, and errors are difficult to quantify. The mass balance results for David, Mulock and Nimrod glaciers all seem reasonable, given the general consistency in flow speed over the past few decades (Frezzotti, 1993; Swithinbank, 1963) and the lack of large elevation changes in the altimetry record (Davis et al., 2005; Wingham et al., 2006). The large positive balance for Byrd Glacier is a surprise; possible explanations are considered in the next section.

Glacier	Catchment (km <sup>2</sup> )	$\dot{b}$ (Gt yr <sup>-1</sup> )	Year	$\dot{m}$ (Gt yr <sup>-1</sup> )	$flux_{out}$ (Gt yr <sup>-1</sup> )	$\dot{M}$ (Gt yr <sup>-1</sup> )
David	$218,325 \pm 10,916$	$11.70 \pm 0.88$	2001	0.004	$9.28 \pm 0.88$	$2.41 \pm 1.31$
Mulock	$123,925 \pm 6,196$	$7.15 \pm 0.54$	2001	0.003	$5.23 \pm 0.59$	$1.91 \pm 0.84$
Byrd	$1,101,725 \pm 55,086$	$44.27 \pm 3.32$	1978	0.239	$20.64 \pm 1.66$	$23.39 \pm 4.02$
Nimrod	$84,775 \pm 4,238$	$4.27 \pm 0.24$	2006	0.291	$22.32 \pm 1.72$	$21.67 \pm 4.04$
			2001	0.047	$3.34 \pm 0.17$	$0.88 \pm 0.39$

Table 3.4. Mass balance results using accumulation estimates from *Van de Berg et al.* (2006). The year refers to the velocity data used to calculate fluxes.

### 3.6.3 Discussion

Mass balance calculations are sensitive to spatial variations in accumulation rate. Antarctic accumulation rate compilations rely on an irregular, low-density distribution of surface mass balance measurements to guide the interpolation of low-resolution model

output (*Van de Berg et al.*, 2006) or remote sensing measurements (*Arthern et al.*, 2006; *Vaughan et al.*, 1999). For the  $\sim 1.5 \times 10^6 \text{ km}^2$  catchment areas of David, Mulock, Byrd and Nimrod glaciers there are fewer than 100 field measurements, and derived accumulation maps show large inter-map variability. We explore the effect of inter-map variability in Table 3.5 by assuming that each glacier is in steady state and then computing balance velocities required to discharge the mass prescribed by different compilations.

Glacier	$flux_{out}$ (Gt yr $^{-1}$ )	Compilation	$\dot{b}$ (Gt yr $^{-1}$ )	$\bar{u}_{balance}$ (m yr $^{-1}$ )	$\bar{u}_{observed}$ (m yr $^{-1}$ )
David	$9.28 \pm 0.88$	<i>Arthern et al.</i> (2006)	$21.32 \pm 1.49$	734	369
		<i>Vaughan et al.</i> (1999)	$19.01 \pm 0.95$	655	
		<i>Van de Berg et al.</i> (2006)	$11.70 \pm 0.88$	403	
Mulock	$5.23 \pm 0.59$	<i>Arthern et al.</i> (2006)	$10.67 \pm 0.75$	557	342
		<i>Vaughan et al.</i> (1999)	$11.46 \pm 0.57$	598	
		<i>Van de Berg et al.</i> (2006)	$7.15 \pm 0.54$	373	
Byrd	$22.32 \pm 1.72$	<i>Arthern et al.</i> (2006)	$59.37 \pm 4.15$	1888	672
		<i>Vaughan et al.</i> (1999)	$57.72 \pm 2.89$	1836	
		<i>Van de Berg et al.</i> (2006)	$44.27 \pm 3.32$	1408	
Nimrod	$3.34 \pm 0.17$	<i>Arthern et al.</i> (2006)	$5.95 \pm 0.42$	386	203
		<i>Vaughan et al.</i> (1999)	$6.32 \pm 0.32$	409	
		<i>Van de Berg et al.</i> (2006)	$4.27 \pm 0.32$	277	

Table 3.5. Catchment-wide accumulation rates derived from three surface mass balance compilations. The  $flux_{out}$  for Byrd Glacier is estimated using velocities derived in 2006.

The results show that balance velocities computed using accumulation rates from *Van de Berg et al.* (2006) consistently come closest to observed velocities (Table 3.5). Balance velocities based on *Arthern et al.* (2006) and *Vaughan et al.* (1999) show similarities to each other, but are consistently higher than observed velocities. The differences in balance velocity are a function of the methods used to produce the compilations. Both *Arthern et al.* (2006) and *Vaughan et al.* (1999) use satellite microwave radiometry (6.9 GHz and 35 GHz respectively) to extend the spatial distribution of surface measurements. *Van de Berg et al.* (2006) use a regional climate model, calibrated by field measurements, to produce their surface mass balance map. For low accumulation regions, such as the East Antarctic Ice Sheet, model-derived surface mass balance estimates seem to be more

realistic than the satellite-derived products, although we do not know if the same is true for high  $\dot{b}$  regions.

Notwithstanding the good agreement between balance velocities using (*Van de Berg et al.*, 2006) and our observations, there remains a large imbalance for Byrd Glacier (Table 3.5). The simplest explanation is that a small over-estimate in accumulation rate from *Van de Berg et al.* (2006) leads to a large error in mass input when scaled to the Byrd Glacier catchment. Another possibility is that the catchment delineation is too large, and therefore the catchment-integrated accumulation estimate is an overestimate. In this study, the Byrd Glacier catchment basin was delineated using a continental DEM (*Liu et al.*, 1999) and Radarsat imagery to map the ice divides and flow directions. The catchment basin area, estimated to be  $1,101,725 \pm 55,086 \text{ km}^2$ , is consistent with an estimate of  $1,070,400 \text{ km}^2$  by *Rignot and Thomas* (2002). Given an average  $\dot{b}$  value of  $400 \text{ mm yr}^{-1}$  (*Van de Berg et al.*, 2006), the Byrd catchment would need to be less than two-thirds its size ( $\sim 600,000 \text{ km}^2$ ) to be in steady state with its calculated  $flux_{out}$ .

Another possible explanation is that we underestimated the  $flux_{out}$  component of the balance equation. Due to the sparsity of ice thickness measurements, it is possible that ice thickness at the grounding line is too low in our calculations. We use surface elevation measurements from *Brecher* (1982), with an uncertainty of less than 2 m, to calculate the ice thickness from hydrostatic equilibrium. The flux gate would need to be almost twice as large ( $71.3 \text{ km}^2$ , and not  $34.3 \text{ km}^2$ ) in order for Byrd Glacier to be in balance with the prescribed accumulation rates; since the fjord walls do not accommodate widening, this would mean 1350 m thicker ice.

Our results show a positive balance for David ( $2.41 \pm 1.31 \text{ Gt yr}^{-1}$ ), Mulock ( $1.91 \pm 0.84 \text{ Gt yr}^{-1}$ ), and Nimrod ( $0.88 \pm 0.39 \text{ Gt yr}^{-1}$ ) glaciers (Table 3.4). Based on mass budget calculations, *Rignot and Thomas* (2002) estimate a positive balance for Mulock and Byrd glaciers, and a negative ( $2 \text{ Gt yr}^{-1}$ ) balance for David Glacier. Repeat satellite altimetry seems to confirm the positive balance for parts of the Byrd Glacier catchment for the period 1992 – 2003, and also shows the Mulock and David catchments to be close to balance, with isolated areas of thinning near the coast, and thickening on the plateau (*Wingham*

*et al.*, 2006). The balance conditions for the entire Byrd Glacier catchment and Nimrod Glacier are currently unknown (*Rignot and Thomas*, 2002) due to a lack of measurements south of  $\sim 81.5^{\circ}\text{S}$ . Our results are mostly consistent with the earlier studies, except for the calculated imbalance of Byrd Glacier.

### 3.7 Conclusions

Outlet glaciers flowing through the Transantarctic Mountains are important pathways for ice to drain from the EAIS into the Ross Ice Shelf. The stability of these glaciers has long been assumed, yet our analysis shows that several of the EAIS glaciers are undergoing changes in flow speed and dynamics. Below is a summary of the observations.

1. David Glacier, which is not buttressed by the Ross Ice Shelf, maintained steady flow speeds from 1990 – 2006.
2. Mulock Glacier accelerated  $11.2 \pm 4.9 \text{ m yr}^{-2}$  between 2001 and 2003, and  $6.0 \pm 4.6 \text{ m yr}^{-2}$  between 2005 and 2006. There is no apparent surface lowering between 2001 and 2006.
3. Byrd Glacier speeds increased by  $\sim 100 \text{ m yr}^{-1}$  between 2005 and 2007. Thinning appears to be isolated to a bedrock bump located  $\sim 15 \text{ km}$  up from the grounding line.
4. Nimrod Glacier maintained a steady flow speed between 1960 – 2006, and constant surface elevation between 2000 – 2006.

Force balance results show a similar partitioning of forces on each glacier, regardless of geometry or presence/absence of the Ross Ice Shelf past the grounding line. Large values of calculated basal drag imply that all four glaciers are hard-bedded.

Mass balance results indicate small positive balances for David, Nimrod and Mulock glaciers. The large imbalance calculated for Byrd Glacier is likely due to over-estimated catchment-wide accumulation rates. In order to improve basin-wide mass balance estimates, additional accumulation and ice thickness measurements are needed.

## Chapter 4

# MULTI-DECadal RECORD OF ICE DYNAMICS ON DAUGAARD JENSEN GLACIER, EAST GREENLAND, FROM SATELLITE IMAGERY AND TERRESTRIAL MEASUREMENTS

### 4.1 Introduction

A recent program to study the mass balance of the Greenland Ice Sheet demonstrated that the largest changes are currently taking place near the ice sheet margins (*Thomas*, 2001). Thinning rates of several meters per year were observed on large outlet glaciers draining the southeastern portion of the ice sheet (*Krabill et al.*, 2000) and grounding line retreats of several kilometers were measured on glaciers in northern Greenland (*Rignot et al.*, 2001). The calving front of Jakobshavn Isbræ, Greenland's largest glacier, recently retreated  $\sim$ 5 km (based on examination of satellite imagery acquired in 2003) after occupying a quasi-stable position for the previous  $\sim$ 30 years (*Sohn et al.*, 1998). Conversely, extensive regions of the high elevation ice sheet interior appear to be close to steady-state conditions (*Thomas et al.*, 2000b). Current research is directed towards explaining the distribution of these observed changes.

*Abdalati et al.* (2001) suggest that the rapid thinning rates observed in southeast Greenland were initiated as recently as the early 1990s. Air temperatures measured at coastal stations show a cooling trend for most of the twentieth century (*Box*, 2002), but temperatures have been warming since the 1980s. However, glacier thinning rates are too large to be explained by variability in climate alone. An alternative explanation is that the observed thinning is a response to changes in ice dynamics, such as an increase in ice velocities. One mechanism that might account for faster ice motion is an increase in the amount of basal lubrication, perhaps as a result of enhanced surface melting (e.g., *Zwally et al.*, 2002). Unfortunately, very few glaciers in Greenland have the long records of ice velocities that are necessary to test this hypothesis.

In this paper, we report the results of a study on Daugaard Jensen Glacier, one of the largest and fastest flowing outlet glaciers in East Greenland (Figure 4.1). We base our analysis on a combination of field measurements conducted in the 1960s, mapping of flow velocities from modern high-resolution ASTER satellite imagery, and an examination of calving front positions from archival image sources acquired since the 1950s. The data are used to test for recent changes in ice flow regime, and to compare ice dynamics with mass balance conditions for the glacier.

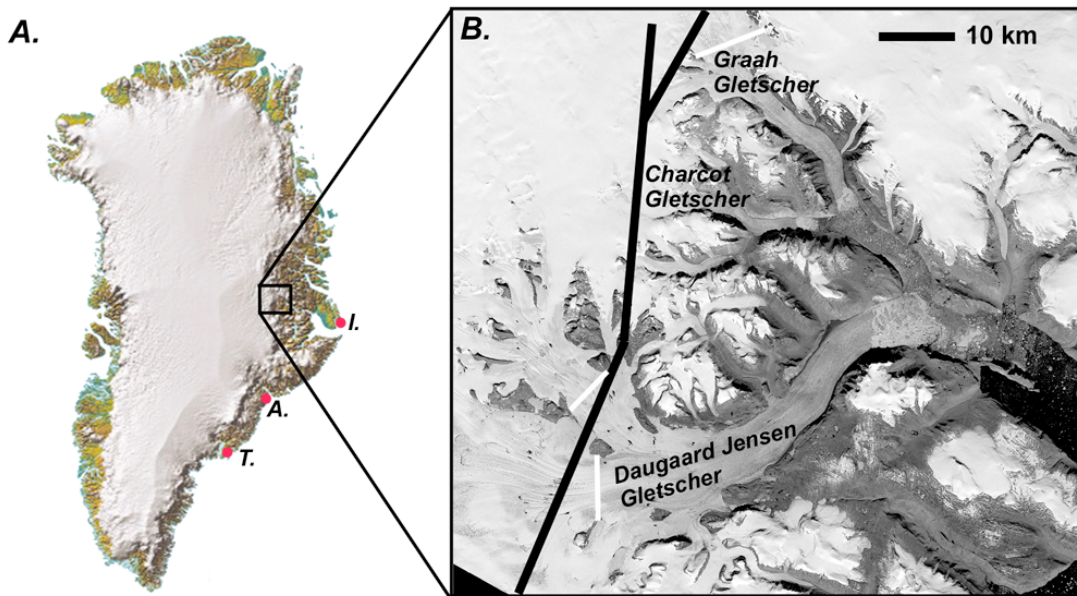


Figure 4.1. A) Map of the study area and nearby automatic weather stations from *Box* (2002). The weather stations are referred to in the text as Ittoqqortoormiit (I), Aputteeq (A), and Tasiilaq (T). B) Landsat-7 scene showing the location of studied glaciers in northwestern Scoresby Sund, East Greenland. Thick black lines show the locations of the airborne radar profiles (*Gogineni et al.*, 2001). Thin white lines show the location of mass balance flux gates.

Daugaard Jensen Glacier terminates in tidewater at the head of Nordvestfjord, the northernmost branch of the Scoresby Sund fjord system (Figure 4.1). Two smaller outlet glaciers from the same catchment basin, Charcot Glacier and Graah Glacier (called F. Graae Glacier on some maps), also terminate at tidewater in tributary fjords. The main glacier drains about 4% of the ice sheet and reaches sustained speeds of  $4 \text{ km yr}^{-1}$  near

its grounding line (*Reeh and Olesen*, 1986). Mass balance estimates for the upstream region of the inland ice sheet indicate a small negative balance to no change (*Thomas et al.*, 2000b; *Krabill et al.*, 2000; *Hamilton and Whillans*, 2002). The availability of ice velocity measurements between 1968 and 2005 makes Daugaard Jensen Glacier a useful location to test for recent changes in ice dynamics, and to examine the effects of ice flow on the ice sheet interior.

The analysis shows that the flow of Daugaard Jensen Glacier did not change between 1968 and 2005. Between 1950 and 2007, the calving front occupied a nearly constant position in the fjord. These results are largely consistent with the mass balance conditions observed on the inland ice sheet. An implication of this work is that the conditions forcing a change in ice dynamics in southeast Greenland are not yet operating this far north.

## 4.2 Data

### 4.2.1 Calving Front Positions: 1950 – 2007

The lower 28 km-long trunk of Daugaard Jensen Glacier is constrained in a 5 – 7 km-wide fjord. The glacier appears to be floating within about 4 km of the calving front, based on the change in crevasse patterns observed in satellite imagery. The inferred grounding line position is taken as the point where crevasses become noticeably wider. Ice thickness at the calving margin is  $\sim$ 500 m from the dimensions of capsized icebergs in the fjord immediately in front of the glacier (*Dowdeswell et al.*, 1992), and from hydrostatic equilibrium based on a measured terminus freeboard height of  $\sim$ 60 m (*Reeh and Olesen*, 1986).

Charcot Glacier and Graah Glacier are constrained in  $\sim$ 2 km-wide fjords, 12 km and 26 km long, respectively. Ice thicknesses for both glaciers are smaller than Daugaard Jensen Glacier. Measurements of terminus freeboard heights yield thicknesses of  $\sim$ 240 m for Charcot Glacier and  $\sim$ 320 m for Graah Glacier (*Olesen and Reeh*, 1969).

A record of calving front positions is reconstructed for each glacier using modern and archival imagery, and survey data. The earliest observations are oblique aerial photographs taken in 1950 (*Weidick*, 1995). Survey measurements were made at the terminus

of each glacier in 1968 (*Reeh and Olesen*, 1986). Additional observations were made using Landsat 3 (1973), Landsat 5 (1991) and Landsat 7 imagery (1999). The most recent calving front positions were mapped using ASTER imagery acquired in 2001 – 2007.

The calving front position of Daugaard Jensen Glacier has remained remarkably constant throughout the 57 years of observation (Figure 4.2). Small variations in position are probably the result of annual or seasonal fluctuations in the rate of iceberg production (*Olesen and Reeh*, 1969). The widening and ~400 m deepening of the fjord a few kilometers in front of the calving margin (*Ó Cofaigh et al.*, 2001) probably limits the forward extension of the glacier. The grounding line position, to the extent that the location of sudden crevasse widening can be mapped in the record, also appears to have been relatively stable (within ~250 m, based on the pixel resolution and geolocation uncertainties of archival imagery). This stability indicates that ice flux to the grounding line has remained constant, and might also be an indication that basal melt rates have not increased in recent decades (cf. *Rignot et al.*, 2001).

The terminus position records for Charcot Glacier and Graah Glacier indicate out-of-phase behavior of the neighboring glaciers. *Olesen and Reeh* (1969) note that Charcot Glacier retreated ~2 km between 1933 and 1950, and retreated another ~1 km between 1950 and 1968. During the same period, Graah Glacier maintained a stable front position. The terminus of Charcot Glacier remained at the same position between 1968 and 2006 (Figure 4.2). Graah Glacier retreated 1 – 2 km between 1991 – 1999 but changed very little in the last seven years of observation (Figure 4.2). It appears that both glaciers are in long-term retreat, although it is interesting to note that retreat events seem to occur episodically during longer stages of front position stability.

#### 4.2.2 Glacier Velocities: 1968 – 2005

The flow pattern of Daugaard Jensen Glacier was first measured in the late 1960s by *Olesen and Reeh* (1969) using terrestrial surveying techniques. Velocities were obtained by repeated theodolite intersections from bedrock stations to natural targets on the glacier surface. Most of the targets were located on the floating portion of the glacier, although

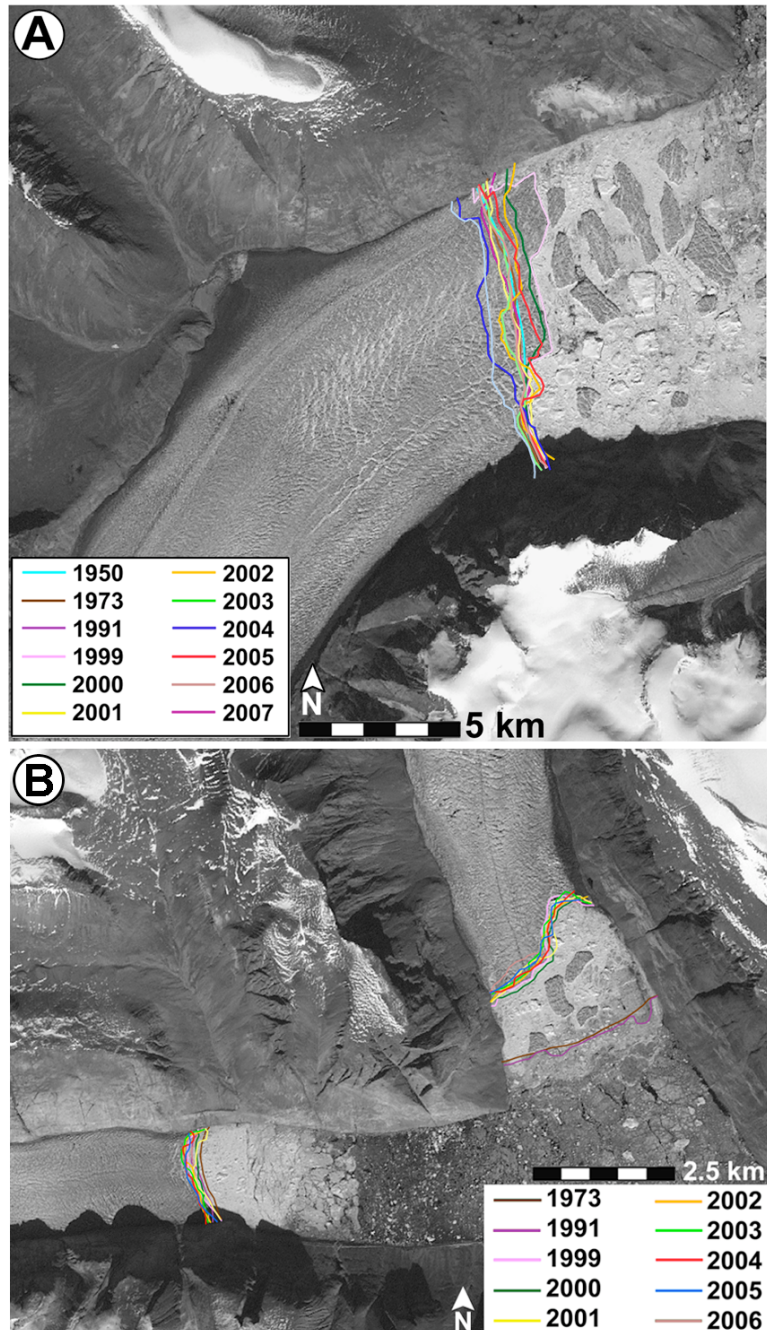


Figure 4.2. Terminus positions for Daugaard Jensen Glacier (A) and for Charcot (panel B, left) and Graah (panel B, right) glaciers. Positions were obtained from aerial photography in 1950; by Landsat 3 in 1973; by Landsat 5 in 1991; by Landsat 7 in 1999 and by ASTER in 2001 – 2007.

some points were measured just upstream of the grounding line. The measurements were made over a period of 32 days and the velocities expressed as annual averages.

*Reeh and Olesen* (1986) noted velocity fluctuations of up to  $2 \text{ m day}^{-1}$ , or 15% of total motion, at the front of the glacier. These velocity fluctuations imply basal lubrication of Daugaard Jensen Glacier. The possibility of these fluctuations being forced by fjord tides, as observed on Jakobshavn Isbræ (*Echelmeyer and Harrison*, 1990), was not supported by the duration and amplitude of the oscillations (*Reeh and Olesen*, 1986).

The presence of basal meltwater from Daugaard Jensen Glacier is also evident from a nearby marine sediment core. The core, drilled 5 km down-fjord from the calving front of Daugaard Jensen, consisted of well-defined, laminated muds (Ó Cofaigh *et al.*, 2001). Laminated muds suggest an abundance of meltwater being delivered into the fjord. Iso-topically light water, sampled at the core site, supports this interpretation (Ó Cofaigh *et al.*, 2001).

The modern flow pattern of the glacier was obtained by applying a feature tracking routine (*Scambos et al.*, 1992) to sequential satellite images acquired by the ASTER sensor in 2001, 2003, 2004 and 2005. High-resolution (15 m pixel size) visible band data were used. The displacement of surface features (crevasses, seracs) was derived by matching patterns of brightness in a reference chip from the first image to identical patterns in a search box from the second image using an automatic cross-correlation technique.

Before implementing the matching routine, the images were geocoded using satellite ephemeris data and co-registered using manual tie points. A principal component filter was applied to both scenes to reduce image noise. *Scambos et al.* (1992) noted that the use of Landsat imagery required additional noise suppression techniques, namely scan-line de-striping, high-pass filtering, and gaussian contrast stretching, but these steps were not necessary for preparing the ASTER images. The feature tracking was performed with a reference chip of  $4 \times 4$  pixels ( $60 \times 60 \text{ m}$ ) and a search box of  $128 \times 32$  pixels ( $1920 \times 480 \text{ m}$ ). The location of the search box and its long axis orientation were based on *a priori* estimates of the glacier flow field.

The selection of the images was based on several considerations. Images were required to be largely cloud-free and have similar illumination characteristics. The ASTER instrument has the capability for across-track off-nadir scene acquisition ( $-8.58^\circ$  to  $+8.58^\circ$

from nadir). This capability unfortunately limits the number of potential matching pairs, because different scene acquisition geometries lead to different image illumination characteristics. *Stearns and Hamilton* (2005) note that, for regions of rugged terrain such as coastal East Greenland, pointing angles of sequential images need to be within  $3^{\circ}$  to maintain common illumination characteristics. An additional consideration was the length of time between scene acquisition dates. The time interval had to be long enough to allow detectable feature displacement, but not so long that features were distorted beyond recognition.

Uncertainties in derived velocities are dominated by errors in image co-registration and the application of the cross-correlation technique. The presence of static features (mountain peaks, rock ridges) was used to minimize image-to-image registration errors to  $\sim 1$  pixel. Uncertainties associated with the cross-correlation technique were quantified by examining the apparent displacement of static features in the images. These displacements never exceeded 1 pixel (15 m). Any matches over the glacier surface with residuals larger than 1 pixel were therefore discarded. Cumulatively, the uncertainties resulting from all error sources ( $\sim 50 \text{ m yr}^{-1}$ ) are unimportant for the fast glacier speeds ( $> 1000 \text{ m yr}^{-1}$ ) being investigated in the current study.

The results show that the speed of Daugaard Jensen Glacier steadily increases with distance along the fjord (Figure 4.3). Peak speeds near the grounding line ( $\sim 4 \text{ km yr}^{-1}$ ) are consistent with field-based measurements by *Reeh and Olesen* (1986) in 1968, suggesting that Daugaard Jensen Glacier has maintained a constant flow field for the past 37 years.

Shadows make feature tracking difficult on Charcot and Graah glaciers, which are both constrained in narrow ( $\sim 2 \text{ km}$ ) fjords with steep walls. Velocities obtained using a Landsat ETM+ image pair reveal that Charcot Glacier reaches speeds of  $500 \text{ m yr}^{-1}$  at the front (Figure 4.4). Velocities increase steadily with distance down the glacier but peak speeds, as expected from the thinner ice, do not reach those of Daugaard Jensen Glacier.

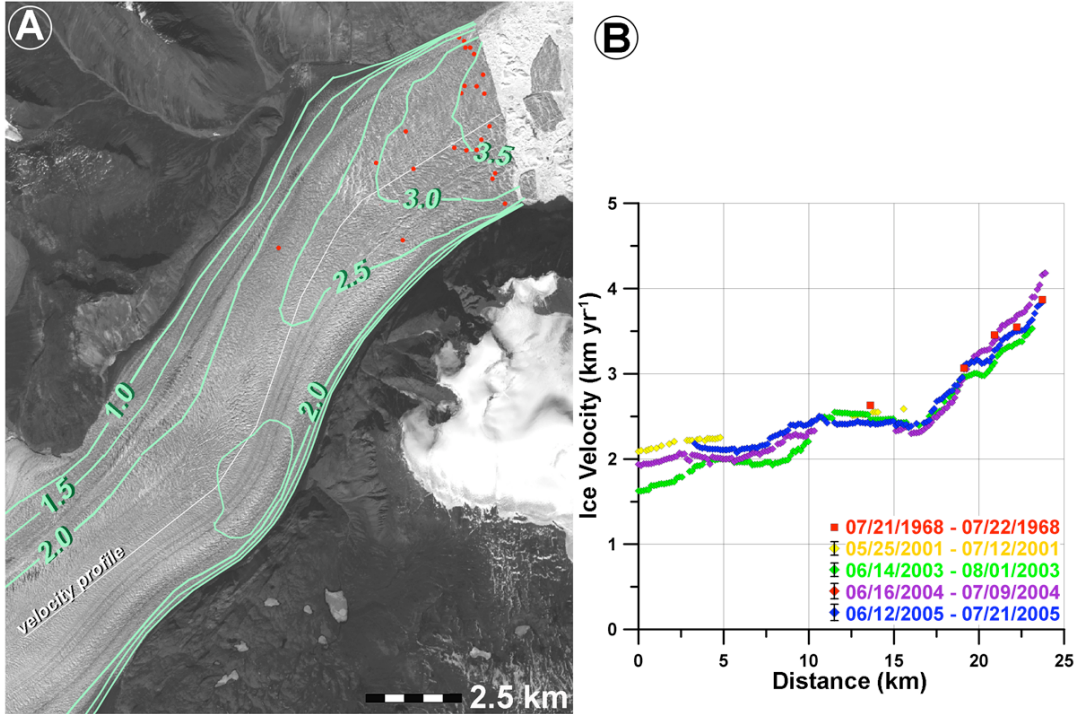


Figure 4.3. Daugaard Jensen Glacier. A) Contoured ice velocity ( $\text{km yr}^{-1}$ ) from feature tracking using 2003 ASTER images. Red circles show the location of survey markers by Reeh and Olesen (1986), overlaid on an ASTER image. B) Ice velocity along the profile in panel A, derived from 2001, 2003, 2004, and 2005 image pairs (diamonds) and field-based measurements (squares) from Reeh and Olesen (1986).

### 4.3 Estimating Mass Balance

The velocity measurements can be combined with accumulation rate maps to estimate the mass balance,  $\dot{M}$ , of the Daugaard Jensen Glacier catchment. Dimensions of the catchment basin,  $A_{\text{catch}}$ , were obtained from a high-resolution elevation model of the ice sheet (Bamber *et al.*, 2001). There are several estimates for snow accumulation rate,  $\dot{b}$ , within the catchment, based on interpolation between numerous isolated ice core records (e.g., Bales *et al.*, 2001; Zwally and Giovinetto, 2001). The mean of these estimates is used to obtain mass added to the catchment,  $flux_{in}$ . The outgoing flux,  $flux_{out}$ , is calculated close to the locations of airborne ice-penetrating radar profiles in the upper trunk of the glacier (Gogineni *et al.*, 2001) (Figure 4.1). Two gates were selected to cover the main tributaries converging at the head of the fjord. Each gate was rotated slightly from the flight line so as to be orthogonal to the measured ice flow vectors.

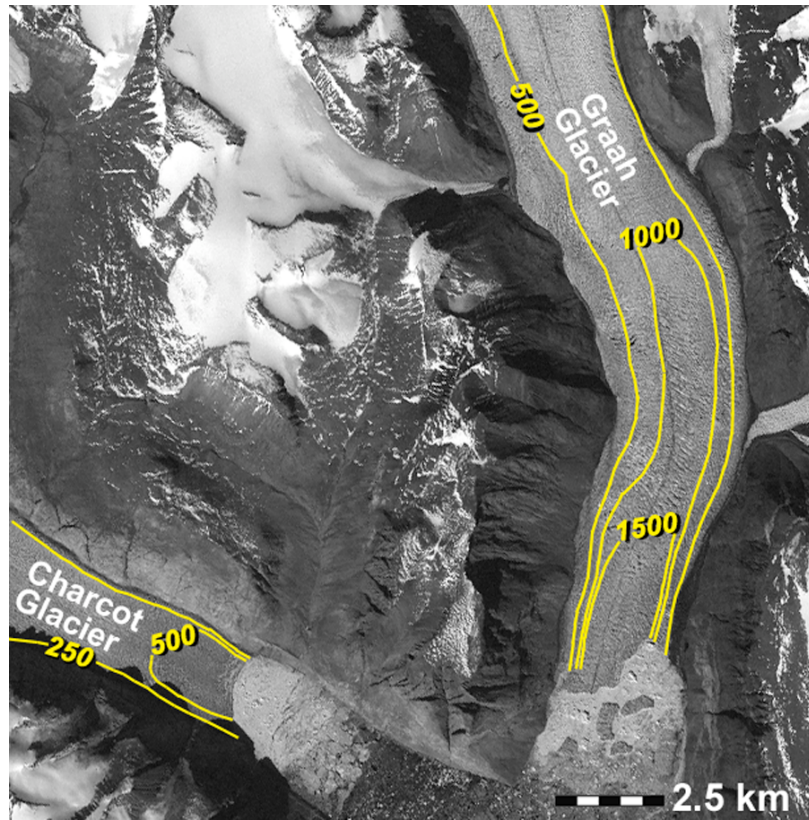


Figure 4.4. Charcot and Graah glaciers. A) Contoured ice velocity ( $\text{m yr}^{-1}$ ) from feature tracking using 2000 – 2001 Landsat ETM+ images.

Similar procedures were followed for Graah Glacier, except for the location of the flux gate. The radar flight lines cross the glacier up-flow of the available satellite image-derived velocities. In order to use the measured velocities, the geometry of a flux gate coinciding with satellite coverage was obtained from an ice thickness compilation of *Bamber et al. (2001)*.

Variable	Symbol	Value
Catchment	$A_{\text{catch}}$	$50,030 \pm 500 \text{ km}^2$
Accumulation	$\dot{b}$	$0.245 \pm 0.07 \text{ m yr}^{-1}$
Flux in	$flux_{in}$	$11.4 \pm 2.6 \text{ km}^3 \text{ yr}^{-1}$
Flux out	$flux_{out}$	$15.2 \pm 0.3 \text{ km}^3 \text{ yr}^{-1}$
Mass Balance	$\dot{M}$	$-3.8 \pm 2.5 \text{ km}^3 \text{ yr}^{-1}$

Table 4.1. Quantities used to estimate mass balance for Daugaard Jensen and Graah glaciers.

Comparing catchment-wide snow accumulation rates with ice fluxes through Daugaard Jensen and Graah glaciers reveals a small negative mass balance equivalent to an average thinning rate of  $-8.24 \pm 5.51 \text{ cm yr}^{-1}$  (Table 4.1). This value is smaller than a local thinning rate of  $-28.1 \pm 20.4 \text{ cm yr}^{-1}$  obtained by *Hamilton and Whillans* (2002) at a site 100 km up-glacier in the catchment area. However, considering the respective uncertainties, both results are statistically similar.

A similar analysis was performed by *Rignot et al.* (2004) using flow velocities obtained by interferometric processing of radar images from 1996 and a slightly different catchment accumulation rate. Their results are consistent with the present analysis, given the uncertainties in each technique.

#### 4.4 Force Balance Distribution

Insight into the large-scale mechanisms controlling glacier motion can be obtained from calculations of the stresses that drive and resist flow. Resistance can come from the bed, the sides, or from along-flow obstacles. Here, we calculate the balance of forces using surface velocity measurements from 2003 ASTER image pairs. The results are difficult to interpret unless the along- and across-flow components of ice flow are isolated, so we partition Daugaard Jensen Glacier into seven sections, and rotate each section to a coordinate system in which the main direction of flow is along the  $x$ -axis. The rotated velocities are interpolated to a 1 km grid, and smoothed to eliminate discontinuities between each section.

The force balance equation,

$$\tau_{dx} = \tau_{bx} - \left( \frac{\partial}{\partial_x} HR_{xx} \right) - \left( \frac{\partial}{\partial_y} HR_{xy} \right), \quad (4.1)$$

described in detail in Chapter 3, identifies the relative contribution of forces driving and resisting glacier flow (*Van der Veen and Whillans*, 1989). The distribution of each component in Equation 4.1 — driving stress ( $\tau_{dx}$ ), lateral drag ( $\frac{\partial}{\partial_x} HR_{xx}$ ), longitudinal stress

gradients ( $\frac{\partial}{\partial y} HR_{xy}$ ), and basal drag ( $\tau_{bx}$ )—are shown in Figure 4.5, overlaid on a Landsat ETM+ image.

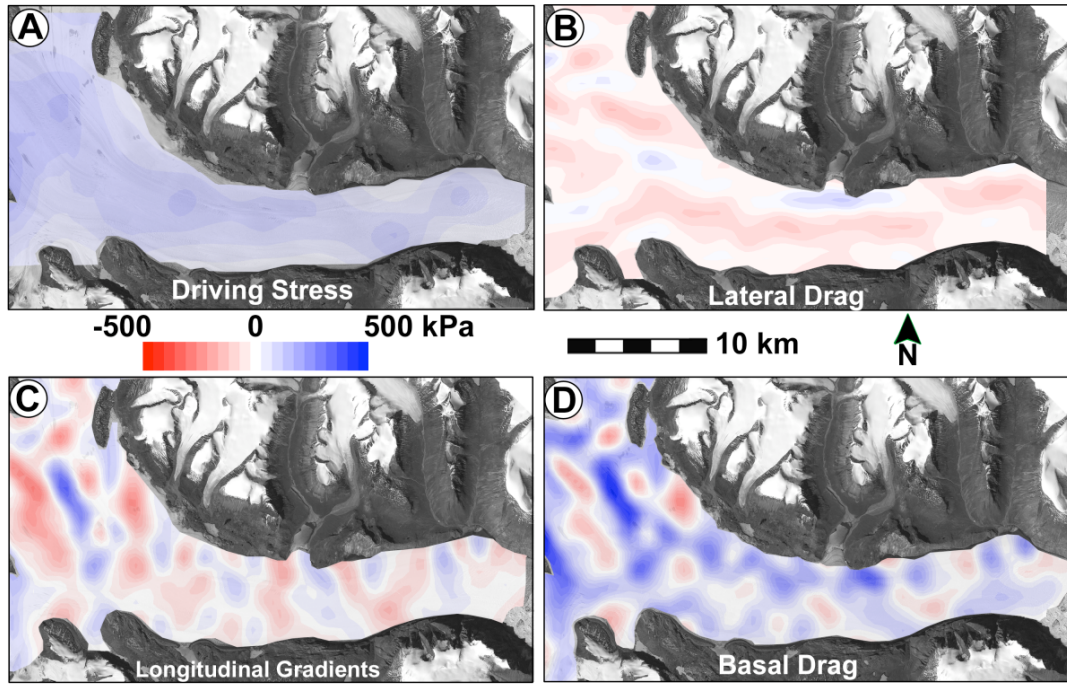


Figure 4.5. Components of the force balance equation of Daugaard Jensen Glacier, gridded to 1 km. A) Driving stress, B) gradients in lateral drag, C) gradients in longitudinal stresses, D) basal drag.

The driving stress,  $\tau_{dx}$ , is a function of surface slope and ice thickness. An ASTER DEM is used to calculate the surface slope averaged over 5 km profiles along the trunk of Daugaard Jensen Glacier. Airborne ice-penetrating radar (data available at [https://www.cresis.ku.edu/research/data/greenland\\_data.html](https://www.cresis.ku.edu/research/data/greenland_data.html)) provides ice thickness measurements in the upper reaches of the glacier (see Figure 4.1); ice thickness at the grounding line is calculated from hydrostatic equilibrium and measured terminus freeboard height. Ice thickness along the trunk is modeled by fitting 4th-order polynomials to cross-sections of the valley-walls (following the technique outlined in section 3.2.3). The minimas of the polynomials are constrained by a linear interpolation of up-stream (radar surveys) and down-stream (hydrostatic equilibrium) ice thicknesses.

The driving stress decreases nearly linearly, from 350 kPa to 50 kPa, along the trunk of Daugaard Jensen Glacier. The increased values at  $x = 20$  and  $x = 27$  km (Figure 4.6) are

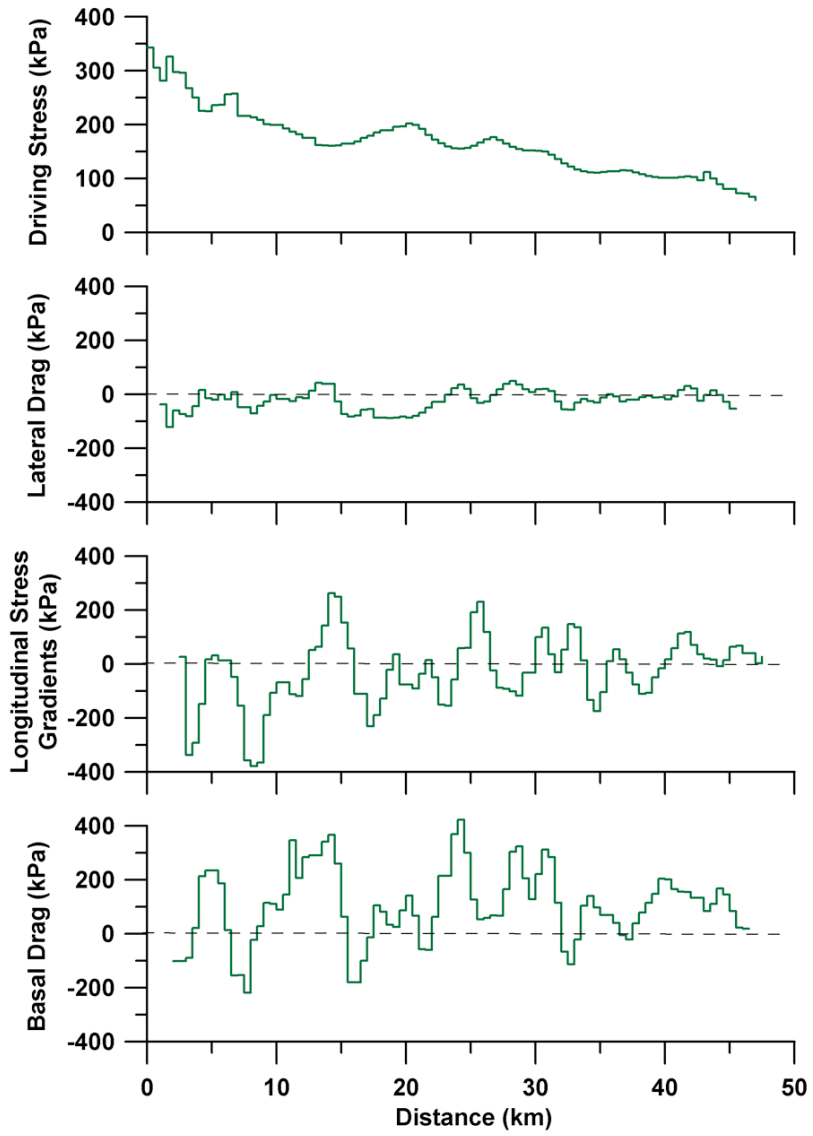


Figure 4.6. Along-flow components of force balance, derived from 2003 velocities and plotted at 1 km spacing. Flow is from left to right.

due to isolated regions of thick ice, as determined from the slope of the adjacent valley walls.

Lateral drag is concentrated along the southern margin of the main trunk (Figure 4.5B). Ice flow is faster along this margin (Figure 4.3), which probably results in increased shearing. Positive values in lateral drag are most likely due to flowline turning,  $\frac{\partial u_y}{\partial x}$ , and are especially evident as a northern tributary enters the main fjord.

The magnitude of lateral drag is surprisingly low along the centerline (rarely exceeding  $-100$  kPa)(Figure 4.6), which could be an artifact of the feature tracking technique. To resolve flow speeds exceeding  $3.0 \text{ km yr}^{-1}$  at the centerline, user-controlled search parameters were selected for large displacements. In doing so, smaller displacements at the glacier margins may have been missed. However, Figure 4.3 shows that fast flow extends very close to the valley walls, supporting the observation that lateral drag is not providing a major component of the overall force balance.

Longitudinal stress gradients provide a significant amount of resistance ( $\sim 400$  kPa) at isolated locations. Along the trunk as a whole, they resist  $\sim 150$  kPa of the driving stress (Figures 4.6 and 4.6). Along-flow extension and compression can be due to changes in ice thickness, surface slope, or merging tributaries. The dominant pattern of compression and extension in the upper reaches of the glacier is due to a surface bump that is also seen in the driving stress contours (Figures 4.5 and 4.6). Merging tributaries cause a local increase in surface slope and ice thickness, which often results in longitudinal extension. Down-flow of merging tributaries are zones of compression (Figures 4.5 and 4.6).

Basal drag resists  $\sim 200$  kPa of the driving stress throughout the trunk of Daugaard Jensen Glacier (Figure 4.5). Basal drag is elevated towards the northern margin of the trunk, where ice flow is slower. Localized areas of high basal drag appear to coincide with changes in surface slope and ice thickness. Negative values of basal drag are not realistic and are probably a function of unreliable ice thickness parameterization. Given the large width/depth ratio of Daugaard Jensen Glacier ( $\sim 4:1$ ), it is not surprising that the majority of flow resistance comes from the bed.

## 4.5 Discussion

Our results of near steady state conditions in the Daugaard Jensen Glacier catchment are quite different from the large thinning rates (several meters per year) observed 500 – 700 km farther south in Greenland, (e.g., Kangerdlugssuaq Glacier) (*Abdalati et al., 2001*). The factors driving rapid thinning of these glaciers do not appear to be acting at the current time in the northwestern Scoresby Sund region. One hypothesis is that increased

surface melt reaching the bed has caused these southeastern glaciers to accelerate and thin (*Abdalati et al.*, 2001; *Krabill et al.*, 2000). This explanation is supported by satellite passive microwave emissivity data revealing a 16% increase in southeast Greenland melt area from 1979 – 2002 (*Abdalati and Steffen*, 2001). While the spatial extent of surface melting fluctuates annually due to weather patterns and volcanic eruptions, there is a consistently larger melt extent in southeastern Greenland (near Kangerdlugssuaq and other rapidly thinning glaciers) than in central East Greenland inland of Scoresby Sund.

Coastal temperature records are consistent with the passive microwave data. From 1961 – 1990, the mean annual temperatures at Aputiteeq and Tasiilaq, the weather stations closest to Kangerdlugssuaq Glacier and other thinning glaciers in southeast, were  $\sim 6^{\circ}\text{C}$  warmer than at Ittoqqortoormiit near the mouth of the Scoresby Sund fjord system (*Box*, 2002). A  $1^{\circ}\text{C}$  warming for 1985 – 2000, with continued warming since 2001, was also recorded at the southeast stations, but not at Ittoqqortoormiit (*Box*, 2002), implying a greater availability of meltwater for basal lubrication of glaciers in that region. No clear warming trend was observed at Ittoqqortoormiit over the last few decades (*Box*, 2002), suggesting that meltwater production on glaciers in the region has not increased.

It is important to note that Daugaard Jensen Glacier is located  $\sim 300$  km from the weather station, and that it is likely that the inner part of the Scoresby Sund fjord system experiences cooler continental conditions. However, the climate record at Illoqqortoormiut is consistent with the stable ice dynamics of Daugaard Jensen Glacier between 1968 and 2007.

## 4.6 Conclusions

An analysis of remote sensing observations and field measurements indicates near steady-state conditions for the last  $\sim 50$  years in the Daugaard Jensen Glacier region of central East Greenland. Ice velocities near the terminus, obtained from terrestrial theodolite surveys in 1968, are similar to those obtained at the same location by tracking surface features in satellite images from 2001 – 2005. The calving front of Daugaard Jensen Glacier remained in approximately the same position throughout the period of observa-

tion from 1950 – 2007. This result is consistent with a constant flux of ice to the grounding line, indicated by the steady velocities. It also suggests that there has been no increase in basal melting beneath the floating section of the glacier tongue, in contrast to observations further south in Greenland (*Rignot et al.*, 2001). The terminus positions of Charcot and Graah glaciers, two smaller glaciers in the same system, show long-term retreat, although most of the retreat occurs episodically between longer phases of stability.

The mass budget of the glacier catchment, estimated using measured velocities, accumulation rates, and surface and bed topographies, indicates a small negative balance. This result is consistent with slow thinning rates calculated for sites inland of the fjord (*Krabill et al.*, 2000; *Hamilton and Whillans*, 2002). The currently stable ice dynamics of the outlet glacier trunk do not appear to be the cause of this small negative balance, although it is not possible to ascertain if glacier speeds increased during an earlier period of warming in the first half of the twentieth century (*Box*, 2002). Alternatively, catchment-wide accumulation rates may under-estimate the actual snowfall.

Force balance analysis shows that basal drag provides most of the resistance to flow of Daugaard Jensen Glacier. Lateral drag and longitudinal stress gradients provide lesser amounts of resistance. This is important because it suggests that Daugaard Jensen Glacier is sensitive to possible increases in melt water penetration to the bed. This may be a key parameter that is overlooked in ice sheet models that predict the rate of ice sheet disintegration under various global warming scenarios.

## Chapter 5

# RAPID VOLUME LOSS FROM TWO EAST GREENLAND OUTLET GLACIERS QUANTIFIED USING REPEAT STEREO SATELLITE IMAGERY

### 5.1 Introduction

The Greenland Ice Sheet's contribution to sea level more than doubled in the past decade, from  $0.23 \text{ mm yr}^{-1}$  in 1996 to  $0.57 \text{ mm yr}^{-1}$  in 2005 (*Rignot and Kanagaratnam, 2006*). Several large outlet glaciers accelerated during this same period (*Howat et al., 2005; Rignot and Kanagaratnam, 2006*). There is no evidence that snow accumulation increased sufficiently to compensate for the enhanced discharge of mass (*Velicogna and Wahr, 2006*), suggesting that ice dynamics are playing a major role in Greenland's sea level contribution.

The largest changes in ice dynamics are observed in Southeast Greenland, where several large outlet glaciers have accelerated and retreated in the past four years (*Rignot and Kanagaratnam, 2006*). Flow acceleration leads to dynamic thinning by increasing longitudinal stretching rates. Several Greenland outlet glaciers have been thinning at rates of  $1 - 10 \text{ m yr}^{-1}$  since the mid-1990s (*Abdalati et al., 2001; Thomas et al., 2000a, 2006*), perhaps as a result of this process. We observed unweathered ice stranded on fjord walls approximately 100 m above the present surfaces of Kangerdlugssuaq and Helheim glaciers during field visits in July 2005, indicating a relatively recent drawdown and a possible increase in the rate of glacier thinning. Here we quantify rates and timings of surface elevation and ice volume change on both glaciers for the period 2001 – 2006 using repeat stereo satellite images, and reconstruct histories of calving front position and ice velocity.

### 5.2 Data

#### 5.2.1 Calving Front Position

Calving front positions are reconstructed for each glacier using field survey data, satellite imagery and aerial photography. Observations range from aerial photographs

taken in the 1930s and 1950s, to satellite images acquired by Landsat 3, Landsat 5, Landsat ETM+ and ASTER from the 1970s onwards. All images were acquired in the summer months of May–September.

### 5.2.2 Ice Velocity

#### 5.2.2.1 Ground-based GPS Surveys

Field surveys were performed in June/July 2005 using dual-frequency phase tracking Trimble 5700 GPS receivers with Zephyr geodetic antennas. The surveys were conducted within a few km of the calving fronts of each glacier (see Figures 5.2A and 5.3A), using a helicopter to access the extremely crevassed surfaces. Metal stakes drilled 1 – 2 m into the glacier surface acted as antenna mounts. 50 – 120 minutes of 15 s data were collected during each occupation and processed relative to a static GPS station located on bedrock at each glacier margin. This data collection and processing strategy is appropriate for the short baselines (<10 km) of our survey networks (*Mader, 1992*).

Each stake was occupied a minimum of three times over a period of 48 – 84 hours. Because of large displacements during each occupation (~1.5 m), we re-processed the data using only the middle 10 minutes of each survey to minimize receiver motion and resulting uncertainties. This choice was based on an analysis of the decay in errors due to baseline processing (in which the uncertainty decreases with increasing occupation time) and inflation of errors arising from receiver motion (in which the uncertainty increases with increasing occupation time). Repeat positions derived from the middle 10 minutes of each occupation were used to calculate velocities for each survey epoch. The results were invariant to the choice of epoch. Here, we report the velocities calculated over the longest survey interval for each stake as scaled to annual averages. The uncertainties were derived from errors in GPS positioning of stakes on the glacier, minimized using the procedure described above. Calculated uncertainties are relatively large (~10 – 35 m yr<sup>-1</sup>) owing to the short observation intervals (~2 – 4 days), but are unimportant for the observed flow speeds.

### 5.2.2.2 Feature Tracking

Ground based GPS surveys provide high precision, but spatially limited, records of ice velocity. We use sequential high-resolution optical satellite imagery to obtain dense and spatially extensive arrays of velocity vectors for each glacier. Displacement vectors are derived by applying an automated feature tracking algorithm (*Scambos et al.*, 1992) to pairs of images acquired by ASTER (Advanced Spaceborne Thermal Emission and Reflection Radiometer) and Landsat ETM+ (Enhanced Thematic Mapper Plus). The application of this technique to ASTER imagery is described by *Howat et al.* (2005) and *Stearns and Hamilton* (2005), and in Chapter 2. The time separation in each image pair varied from 1 – 2 weeks to several months, depending on glacier speed. Faster moving glaciers require short-interval image pairs to avoid the excessive rotation or destruction of trackable features (see *Stearns and Hamilton*, 2005). Uncertainties are largely a function of image co-registration and are quantified using the apparent displacement of static bedrock features (*Stearns and Hamilton*, 2005). Resulting errors in the calculated velocities are variable because of the different time separation of each image pair. In all cases, errors are unimportant to the observed speeds.

We perform the analysis on 1 – 6 suitable image pairs for each glacier obtained between July 2000 and August 2005. Because we use optical imagery, all scenes were acquired during the summer months, broadly defined as May – September. The 2005 GPS derived velocities are consistent, within error bounds, with feature-tracking results from images acquired at nearly identical times, indicating that glacier speeds measured over a few days (GPS surveys) are not biased by short-term transient flow behavior. We are unable to quantify a seasonal pattern in flow speeds because we use only summer data. On Jakobshavn Isbræ, both *Echelmeyer and Harrison* (1990) and *Joughin et al.* (2004) report little seasonal variation in velocity, although *Luckman et al.* (2006) report seasonal fluctuations immediately preceding a phase of rapid retreat. A study involving a larger number of outlet glaciers (*Rignot and Kanagaratnam*, 2006) suggests that summer velocities show a modest 8% increase over winter velocities, but concludes that seasonal variation has a minor effect on annual averages.

### 5.2.3 DEM Extraction Method and Errors

The ASTER (Advanced Spaceborne Thermal Emission and Reflection Radiometer) sensor collects a stereo image-pair using two telescopes in visible band 3: a nadir-viewing telescope (3N) and a backward-looking telescope (3B) (*Yamaguchi et al.*, 1998). The advantage of using the ASTER instrument for stereo mapping over other sensors such as SPOT 1–5 (*Berthier et al.*, 2004) is that the overlapping nadir and backward images are collected at nearly the same time (57 s apart) on the same orbit cycle, minimizing the impacts of image decorrelation.

We generate digital elevation models (DEMs) in-house from stereo imagery of Kangertlugssuaq and Helheim glaciers using the Japanese ASTER Science Team procedure described by *Fujisada et al.* (2005). Products generated using identical procedures can be ordered from the NASA/USGS Land Processes Distributed Active Archive Center (LPDAAC) at <http://edcimswww.cr.usgs.gov/pub/imswelcome>. Suitable images were selected on the basis of minimal cloud cover and small off-nadir image acquisition angles (ASTER can acquire images up to  $\pm 24^\circ$  from nadir in the across-track direction). The 3N and 3B scenes are co-registered using a cross-correlation algorithm which matches brightness values between scenes, and elevation information is extracted using the parallax formed from each stereo pair. To prevent the occurrence of false elevation changes, we manually edit obvious blunders and semi-automatically mask clouds from the processed data.

Each DEM has a post spacing of 15 m, corresponding to the pixel resolution of ASTER's visible bands. Geolocation is entirely on the basis of the satellite ephemeris information contained in the image header file and has an uncertainty of approximately 50 m, which is consistent with the error in spacecraft positioning (*Fujisada et al.*, 2005). We minimize the effect of geolocation errors in the subsequent analysis by manually co-registering sequential DEMs.

The DEM uncertainties are a combination of systematic errors, or bias, and random errors due to satellite positioning, image acquisition geometry, and atmospheric conditions. We did not detect any bias in a pair-wise comparison of elevations of static points

extracted from  $5 \times 5$  km bedrock sections in each DEM, as shown by an arithmetic mean elevation difference of  $-3$  m for all pairs. The random errors contribute a root mean square error in elevation of  $\pm 7.1$  m for all image pairs, based on a comparison of the elevation differences of the static areas. This error is consistent with uncertainties of  $\sim 5\text{--}10$  m reported by *Fujisada et al.* (2005). In the following sections describing thinning and volume change calculations, we assume a conservative elevation uncertainty of  $\pm 10$  m to account for additional possible errors due to DEM extraction over high-elevation parts of each glacier where there is no static ground control.

## 5.3 Observed Changes

### 5.3.1 Calving Front

Kangerdlugssuaq Glacier ( $68.5^{\circ}\text{N}$ ,  $33^{\circ}\text{W}$ ) retreated  $\sim 5$  km between June 2004 and July 2005 (Figure 5.1A). Prior to the rapid retreat, the glacier occupied a quasi-stable front position for  $\sim 30$  years (see also *Thomas et al.*, 2000a). The static front position followed a retreat from the Little Ice Age maximum extent which, on the basis of trimlines observed in the field, was a few km outside the 1933 position.

The large retreat in 2005 left two tributaries, which previously drained into the trunk of Kangerdlugssuaq Glacier, draining directly into the fjord (Figure 5.1). Tributary glacier velocities increased four-fold following the removal of buttressing provided by Kangerdlugssuaq. This response is similar to glacier acceleration following ice shelf collapse observed in the Antarctic Peninsula (*Scambos et al.*, 2004), and highlights the sensitivity of outlet glaciers to perturbations at the calving front.

Helheim Glacier ( $66.5^{\circ}\text{N}$ ,  $38^{\circ}\text{W}$ ) maintained a near-steady front position between September 1972 and July 2002, after which it entered a phase of rapid retreat (Figure 5.1B). The glacier retreated  $\sim 7.3$  km between July 2001 and August 2005, with the largest change ( $\sim 4$  km retreat) taking place between August 2004 and July 2005.

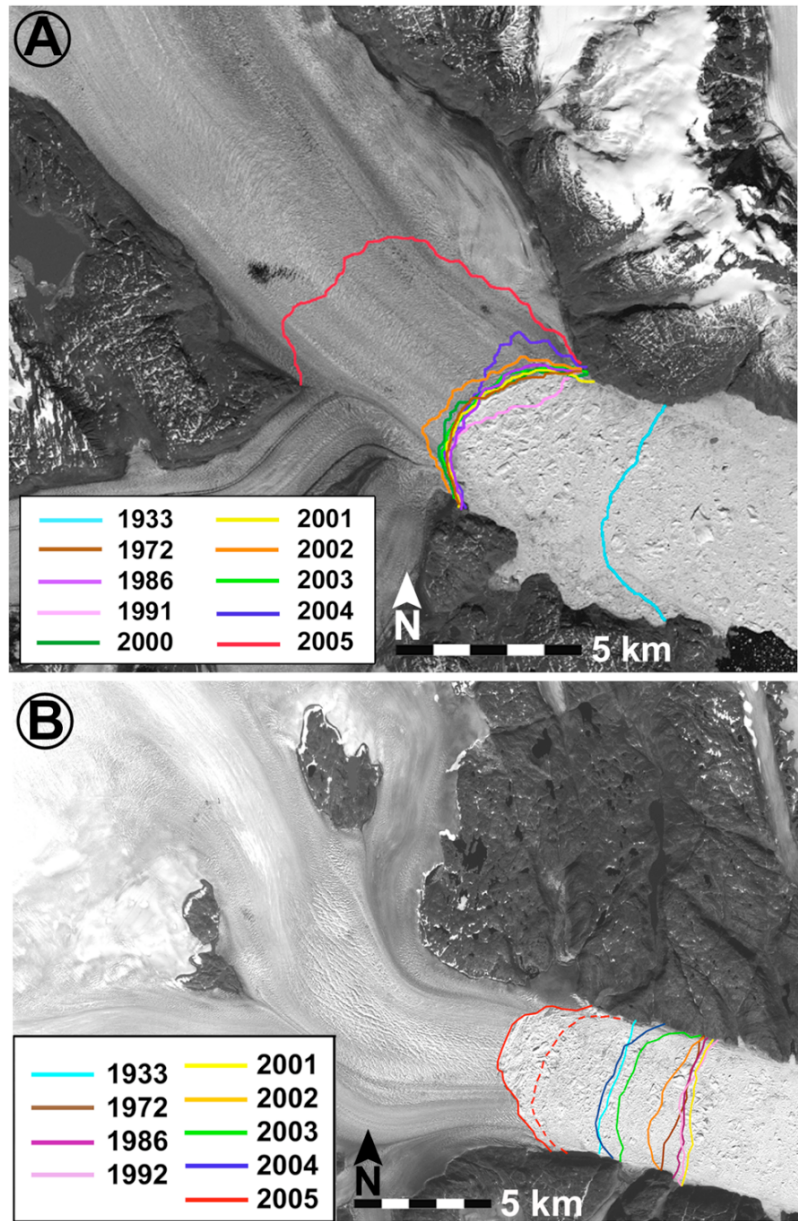


Figure 5.1. Calving front positions for (A) Kangerdlugssuaq Glacier and (B) Helheim Glacier determined from aerial photographs and satellite imagery. The dashed red line in (B) represents the calving front in June, 2005. The solid red line is from August, 2005.

### 5.3.2 Ice Velocity

New measurements of ice velocity reveal large and rapid changes in flow dynamics on both Kangerdlugssuaq and Helheim Glaciers in the past 5 years. Speeds near the terminus of Kangerdlugssuaq in July 2001 were  $5.30 \pm 0.40 \text{ km yr}^{-1}$  based on feature

tracking using a Landsat ETM+ image pair (Figure 5.2). Similar speeds were obtained using data collected in 1966 (*Thomas et al.*, 2000a), 1988 (*Dwyer*, 1995) and 1996 (*Rignot et al.*, 2004). Our feature tracking results show a modest acceleration at the front (to  $6.80 \pm 0.10 \text{ km yr}^{-1}$ ) in 2003 (Figure 5.2B). By June 2005, Kangerdlugssuaq Glacier had accelerated to a velocity maximum of  $14.15 \pm 0.01 \text{ km yr}^{-1}$ , according to GPS measurements, within 1 km of the calving front (Figure 5.2). Remote-sensing measurements are consistent with those derived from GPS, and show a 2005 acceleration that progressed at least 12 km up glacier (Figure 5.2B).

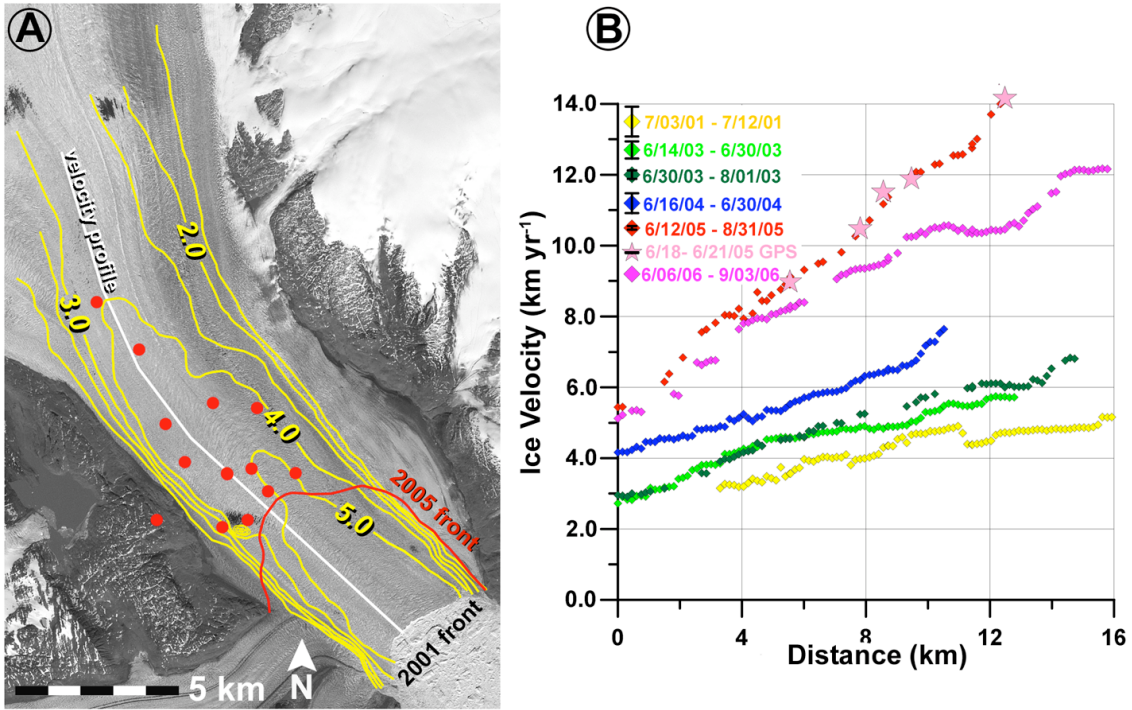


Figure 5.2. Kangerdlugssuaq Glacier. A) Contoured ice velocity ( $\text{km yr}^{-1}$ ) from feature-tracking using 2001 Landsat image pairs. Red circles show the location of GPS surveys conducted in July 2005. B) Ice velocity along the profile in panel A, derived from 2001, 2003, 2004, 2005, 2006 Landsat ETM+ and ASTER image pairs (diamonds), and matching 2005 GPS measurements (stars) along and adjacent to the profile.

Helheim Glacier, located  $\sim 300$  km south of Kangerdlugssuaq Glacier, has undergone similar changes in flow dynamics. In July–August 2001, the terminus region of Hel-

heim Glacier was flowing at  $8.40 \pm 0.20 \text{ km yr}^{-1}$ , based on the results of feature tracking applied to a Landsat ETM+ image pair (Figure 5.3A). *Rignot et al.* (2004) report similar speeds derived from speckle tracking on satellite radar images acquired in 1996. In 2003 the lower glacier accelerated to  $10.30 \pm 0.10 \text{ km yr}^{-1}$ , and by 2005 the glacier was flowing at  $11.30 \pm 0.03 \text{ km yr}^{-1}$  near the terminus (Figure 5.3B). The acceleration was not restricted to the terminus zone. Speeds were  $9.60 \pm 0.03 \text{ km yr}^{-1}$  at a site 5 km from the calving front. These  $\sim 40\%$  increases in flow speed are observed in both the field GPS and ASTER feature tracking results (Figure 5.3B), and are consistent with a separate analysis by *Howat et al.* (2005).

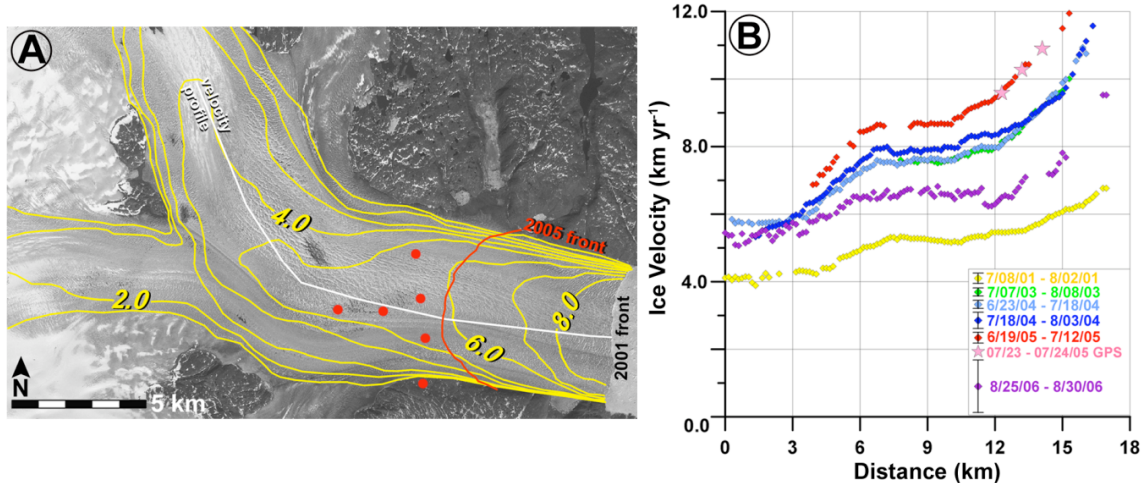


Figure 5.3. Helheim Glacier. A) Contoured ice velocity ( $\text{km yr}^{-1}$ ) from feature-tracking using 2001 Landsat image pairs. Red circles show the location of GPS surveys conducted in July 2005. B) Ice velocity along the profile in panel A, derived from 2001, 2003, 2004, 2005, 2006 Landsat ETM+ and ASTER image pairs (diamonds), and matching 2005 GPS measurements (stars) along and adjacent to the profile.

### 5.3.3 Surface Elevation

For Kangerdlugssuaq Glacier (Figure 5.4A), changes in surface elevation were computed for two profiles along and across the glacier (Figure 5.4B). Between 2001 – 2004, thinning rates were nearly uniform at  $20 \pm 5 \text{ m yr}^{-1}$  along the 20 km profile to the 2005 calving front (Figure 5.4C). The front thinned faster ( $87 \pm 14 \text{ m yr}^{-1}$ ) than the upper part

of the glacier ( $12 \pm 15$  m  $\text{yr}^{-1}$ ) between 2004 - 2005 (Figure 5.4C), coinciding with flow speed acceleration and rapid retreat of the calving front.

Between 2005 – 2006, thinning rates were larger ( $59 \pm 13$  m  $\text{yr}^{-1}$ ) in the upper part of the glacier compared to the terminus region ( $28 \pm 13$  m  $\text{yr}^{-1}$ ), indicating that changes initiated near the front had propagated  $\sim 20$  km upglacier in one year. Thinning extended across the whole width of the glacier near the calving front, as shown by the cross-profile (Figure 5.4D), but were concentrated on the western half of the glacier. Here, thinning rates were  $20 \pm 5$  m  $\text{yr}^{-1}$  between 2001 – 2004. This rate increased to  $87 \pm 14$  m  $\text{yr}^{-1}$  between 2004 – 2005 (Figure 5.4D) but slowed to  $28 \pm 13$  m  $\text{yr}^{-1}$  between 2005 – 2006. Note that in all cases the quoted errors appear relatively large because we adopt a conservative uncertainty (10 m) in elevation determination.

Widespread thinning is also detected on Helheim Glacier (Figure 5.5A). Two profiles along and across the glacier (Figure 5.5B) show that thinning occurred in two episodes. The first episode between 2002 – 2003 resulted in a mean thinning rate of  $44 \pm 21$  m  $\text{yr}^{-1}$  on the 20 km longitudinal profile to the 2005 calving front (Figure 5.5C). Slower thinning rates ( $15 \pm 21$  m  $\text{yr}^{-1}$ ) occurred between 2003 – 2004. The thinning accelerated to  $60 \pm 13$  m  $\text{yr}^{-1}$  between 2004 - 2005, and decreased again between 2005 - 2006 (to  $7 \pm 21$  m  $\text{yr}^{-1}$ ). Similar patterns and rates of surface lowering are measured on a transverse profile near the 2005 calving front (Figure 5.5D).

These thinning rates are much larger than elevation changes measured along earlier repeat laser altimeter flight-lines on the same glaciers. *Abdalati et al.* (2001) report thinning rates near the calving fronts of  $\sim 2 - 10$  m  $\text{yr}^{-1}$  in the late 1990s, and *Krabill et al.* (2004) note continued thinning in excess of 3 m  $\text{yr}^{-1}$  between 1997 – 2003. Both studies detected smaller but still significant amounts of thinning up 70 km inland from the calving fronts, which is consistent with the pattern derived from our repeat DEM analysis. We attribute the overall difference in thinning rates to a switch from gradual thinning in the 1990s to rapid thinning since 2000.

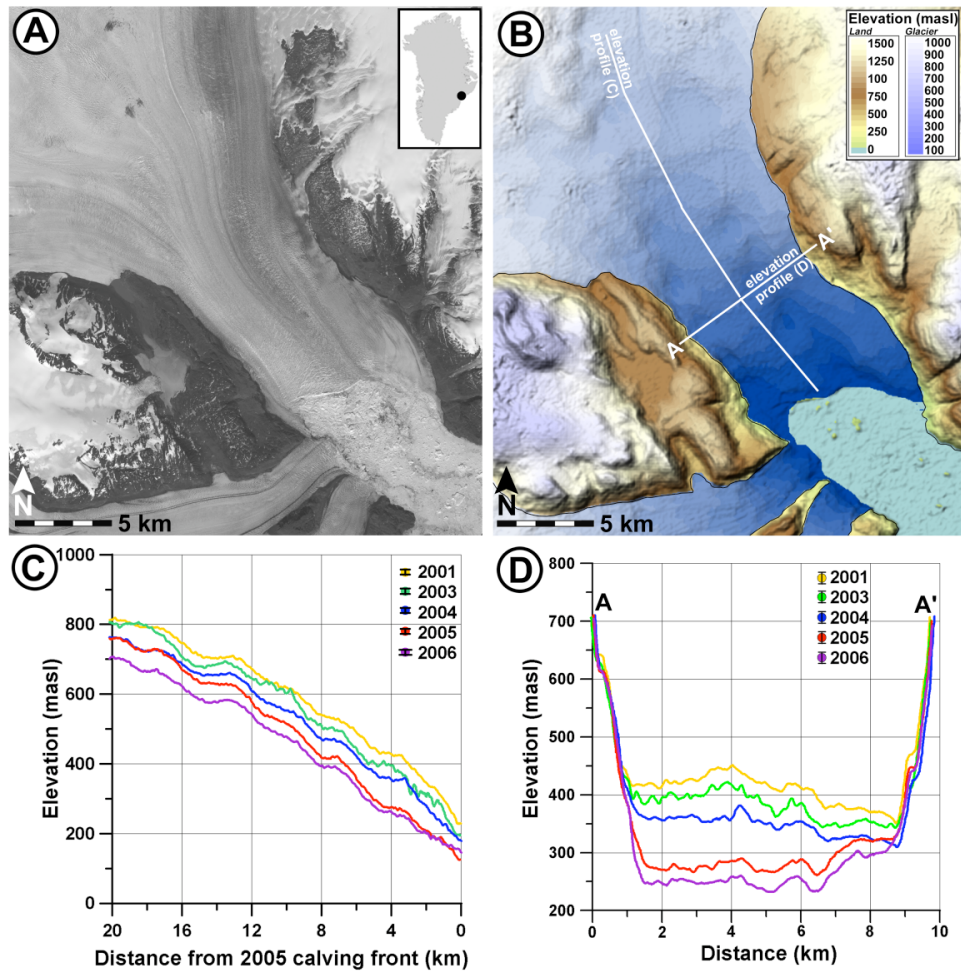


Figure 5.4. Kangerdlugssuaq Glacier. A) ASTER image acquired June 21, 2005. B) Surface topography derived from the image in panel A. C) Surface elevation change on the along-flow profile labeled in panel B (0 km is the terminus). D) Surface elevation change on the across-flow elevation profile labeled in panel B. Note the consistent elevation profiles on the steep fjord walls on either side of the glacier, indicating the good quality of the sequential DEMs.

### 5.3.4 Volume Change

By producing DEMs for two different years and differencing them, we are able to derive estimates of volume change across extensive regions within  $\sim 50$  km of the coast on both glaciers. Images of this larger region are available only for 2001 and 2006 for Kangerdlugssuaq Glacier, and 2002 and 2005 for Helheim Glacier (nearly-annual DEM coverage is available for the lower portions of each glacier). Our analysis shows that Kangerdlugssuaq Glacier lost  $\sim 119 \pm 17$   $\text{km}^3$  of ice within a  $1,750 \text{ km}^2$  region (Figure

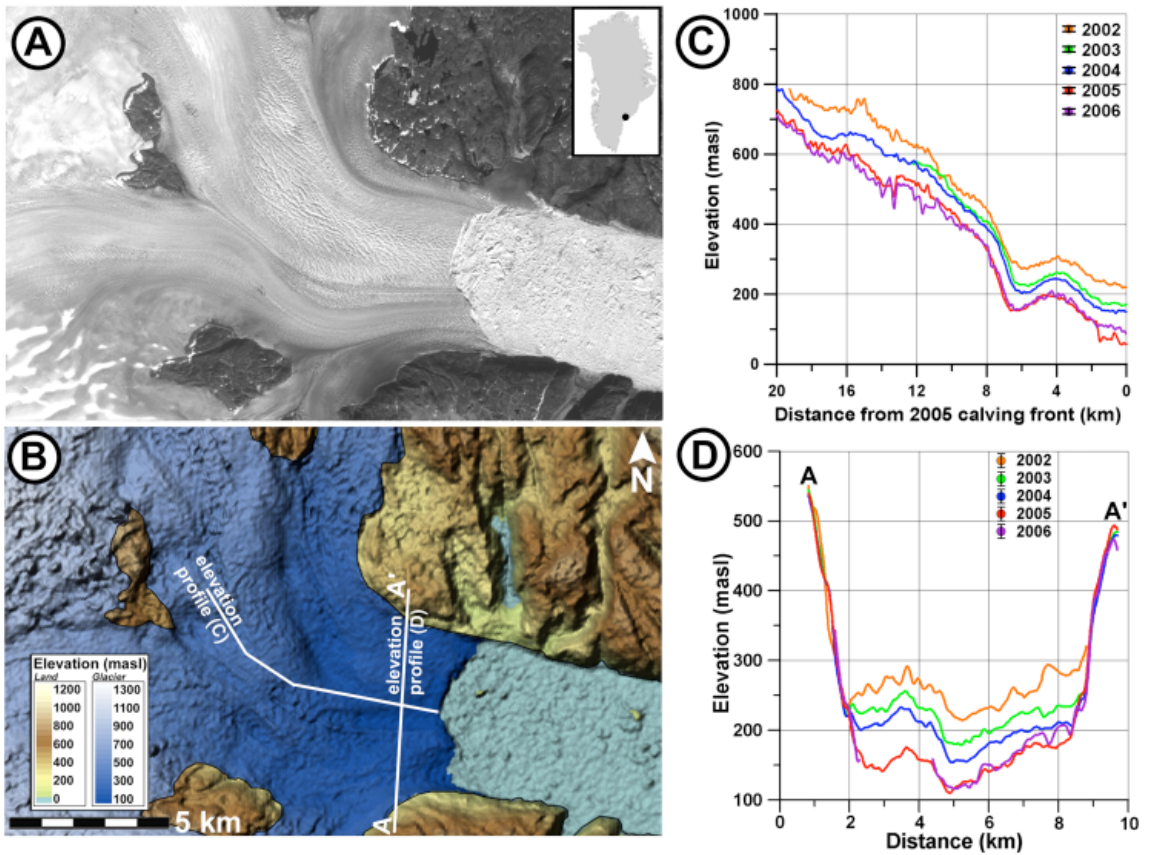


Figure 5.5. Helheim Glacier. A) ASTER image acquired August 29, 2005. B) Surface topography derived from the image in panel A. C) Surface elevation change on the along-flow elevation profile labeled in panel B (0 km is the terminus). D) Surface elevation change on the across-flow elevation profile labeled in panel B.

5.6A) over the period of observation. The retreat of the calving front contributed an additional volume loss which we estimate to be  $\sim 19 \text{ km}^3$ , based on a frontal ice thickness of 700 m (*Thomas et al., 2000a*). A  $1,040 \text{ km}^2$  region of Helheim Glacier (Figure 5.6B) lost  $\sim 52 \pm 9 \text{ km}^3$  between 2002 and 2005, with an additional  $\sim 18 \text{ km}^3$  of ice loss being attributed to calving front retreat. Expressed in terms of annual loss, these estimates suggest that the coastal portions of Kangerdlugssuaq and Helheim glaciers together lost  $\sim 51 \pm 8 \text{ km}^3 \text{ yr}^{-1}$  due to thinning and terminus retreat.

Surface elevation changes measured near the coast are extrapolated to higher elevations using fourth-order polynomials (Figure 5.6C-D) to estimate catchment-wide vol-

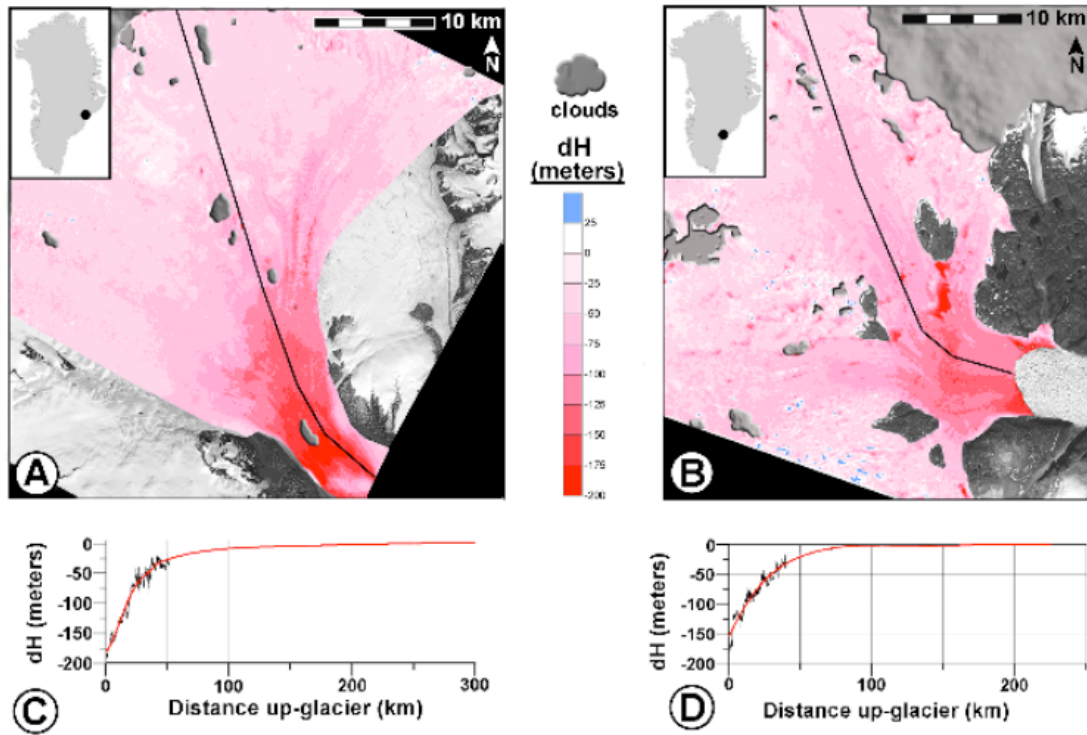


Figure 5.6. A) Map of surface elevation change on Kangerdlugssuaq Glacier, over a 1,750 km<sup>2</sup> area between July 2001 – July 2006. B) Map of surface elevation change on Helheim Glacier over a 1,040 km<sup>2</sup> area between June 2002 – August 2005. C) Fourth-order polynomial fit to measured surface elevation changes on Kangerdlugssuaq Glacier and extrapolated to the ice divide along the black line in panel A. D) Fourth-order polynomial fit to measured surface elevation changes on Helheim Glacier and extrapolated to the ice divide along the black line in panel B.

ume losses for both glaciers (cf., Arendt *et al.*, 2002; Rignot *et al.*, 2003). We constrain the polynomial fit at the ice divides with a thickening rate of 0.1 m yr<sup>-1</sup> (Krabill *et al.*, 2004; Thomas, 2004; Thomas *et al.*, 2006; Zwally *et al.*, 2005). A coarse-resolution DEM (Bamber *et al.*, 2001) is used to determine the catchment dimensions and the surface area of elevation bands for regions above the DEM coverage, binned at 250 m contour intervals. The mean thinning rate is computed for each bin and multiplied by its surface area, and the results added to the DEM-derived changes to estimate the total catchment volume change. Uncertainties in these estimates are difficult to evaluate for the high elevation regions where independent elevation change data are sparse. As a substitute, we repeat the polynomial analysis using only those regions with DEM coverage and compare the

results with the DEM-derived changes. The results differ by  $\sim 25\%$ , which we take as the uncertainty in estimated catchment-wide volume changes. The  $51,088 \text{ km}^2$  catchment basin of Kangerdlugssuaq Glacier lost a total of  $\sim 310 \pm 77 \text{ km}^3$  between 2001 and 2006, or the equivalent of  $62 \pm 15 \text{ km}^3 \text{ yr}^{-1}$ . Helheim Glacier, with a catchment of  $48,319 \text{ km}^2$ , lost  $\sim 180 \pm 60 \text{ km}^3$  between 2002 and 2005, or the equivalent of  $60 \pm 15 \text{ km}^3 \text{ yr}^{-1}$ . Note that, due to image availability, the thinning rate for Kangerdlugssuaq Glacier is a 5-year average, whereas for Helheim Glacier it is a 3-year average.

These volume loss estimates represent a significant fraction of the total volume loss from the ice sheet. Estimates of mass loss using GRACE satellite gravity data range from  $101\text{--}129 \text{ km}^3 \text{ yr}^{-1}$  (*Luthcke et al.*, 2006; *Ramillien et al.*, 2006) to  $239\text{--}248 \text{ km}^3 \text{ yr}^{-1}$  (*Chen et al.*, 2006; *Velicogna and Wahr*, 2006) for varying periods between 2002 – 2006. All studies reveal similar patterns of mass loss in Southeast Greenland. *Velicogna and Wahr* (2006) attribute  $161 \pm 24 \text{ km}^3 \text{ yr}^{-1}$  to glaciers in south Greenland; our estimate from just two of these southeastern glaciers is  $\sim 122 \pm 30 \text{ km}^3 \text{ yr}^{-1}$  for a nearly-similar time period. While these estimates are close, part of the difference may be a function of the inability to discriminate, in the footprint of the GRACE data, which glaciers are losing mass. A more straightforward comparison can be made between our results and estimates provided by *Rignot and Kanagaratnam* (2006) based on flux calculations. Their reported volume losses for Kangerdlugssuaq and Helheim glaciers ( $\sim 36 \text{ km}^3 \text{ yr}^{-1}$  and  $\sim 12 \text{ km}^3 \text{ yr}^{-1}$  respectively) are significantly smaller than our catchment-wide estimates, although close to our estimates for losses in the coastal regions. One explanation for the discrepancy is an over-estimate of catchment accumulation rate in the flux calculations which would have the effect of reducing the net difference between the outgoing flux and the mass input. An alternative explanation is that our extrapolation of coastal results to the ice divide leads to erroneous thinning in parts of the upper catchment that are gaining mass.

## 5.4 Interpretation

The measured thinning rates of several tens of  $\text{m yr}^{-1}$  far exceed what might reasonably be expected from enhanced surface melting alone. A substantial amount of the

thinning and volume loss must be due to an increase in longitudinal stretching rates caused by the changes in ice dynamics. The continuity equation,

$$\frac{\partial H}{\partial t} + \nabla \cdot HU + \dot{b} = 0, \quad (5.1)$$

defines the width-averaged rate of thickness change  $\frac{\partial H}{\partial t}$  as a function of the gradient in ice velocity  $U$  and the net surface balance  $\dot{b}$ . We make the simplification that the glacier width is constant, which is a reasonable assumption for the studied sections. Averaged cross-sectional ice velocities come from measurements on summertime satellite image pairs (section 4.3.2). The cross-sections are located at the 2005 calving front, and a site up-flow (6 km inland of the calving front for Helheim; 10 km inland for Kangerdlugssuaq). For the case of fast flowing glaciers, the flux terms dominate the surface balance terms, so we omit  $\dot{b}$  from our analysis. Values of  $H$  are available from ice-penetrating radar surveys along the centerlines of both glaciers (*Abdalati et al.*, 2001; *Thomas et al.*, 2000a), but are missing for regions within a few km of the calving fronts and in the across-flow direction. We estimate ice thicknesses at the front using DEM-derived calving face heights and hydrostatic equilibrium, assuming floating tongues. We scale the computed fluxes by a shape factor of 0.75 to account for unknown across-flow variations in  $H$ . Both of these estimates are subject to errors which are difficult to quantify without additional radar surveys, although their effect on the calculated fluxes are unlikely to alter the sense of the solutions to the Equation 5.1, at least to first-order.

Kangerdlugssuaq	Helheim
$H \sim 600 \text{ m}, H' \sim 700 \text{ m}$	$H \sim 850 \text{ m}, H' \sim 700 \text{ m}$
2001: $U = 2.3 \text{ km yr}^{-1}$ $U' = 3.9 \text{ km yr}^{-1}$	2001: $U = 4.5 \text{ km yr}^{-1}$ $U' = 5.5 \text{ km yr}^{-1}$
2005: $U = 7.1 \text{ km yr}^{-1}$ $U' = 12.6 \text{ km yr}^{-1}$	2005: $U = 6.7 \text{ km yr}^{-1}$ $U' = 9.6 \text{ km yr}^{-1}$

Table 5.1. Quantities used to solve equation 5.1.  $U$  denotes average cross-section velocity, and  $H$  denotes the centerline ice thickness at the top of the section (10 km inland for Kangerdlugssuaq, 6 km inland for Helheim).  $U'$  denotes average cross-section velocity, and  $H'$  denotes the centerline ice thickness at the location of the 2005 calving fronts.

We evaluate Equation 5.1 for the lower sections of each glacier using the values in Table 5.4. The calculations yield a total 4-year (2001 – 2005) thinning due to ice dynamics of  $\sim 212$  m for Kangerdlugssuaq Glacier, and  $\sim 130$  m for Helheim Glacier. These estimates are consistent with thinning amounts derived from the repeat DEM analysis (Figures 5.4C and 5.5C). Small differences between the calculated and measured values are to be expected because of assumptions about ice thickness and omission of the surface balance terms, and because of likely transient speed variations not captured in the velocity data. *Rignot and Kanagaratnam* (2006) calculate a similar amount of dynamic thinning for Kangerdlugssuaq Glacier ( $\sim 250$  m), but a slightly smaller amount for Helheim Glacier ( $\sim 75$  m) perhaps because of differences in assumed ice thickness. The overall good agreement between the observations and the amounts of calculated thinning indicates that the recent accelerations of Kangerdlugssuaq and Helheim glaciers are driving the rapid volume losses.

## 5.5 Conclusion

Since 2001, the coastal portions of Helheim and Kangerdlugssuaq glaciers lost a combined  $208 \pm 19$  km $^3$  of ice by thinning and retreat, or the equivalent of  $51 \pm 8$  km $^3$  yr $^{-1}$ . Extrapolation of the measured data to the ice divides yields a total combined catchment volume loss of  $\sim 122 \pm 30$  km $^3$  yr $^{-1}$ . Ice thinning and volume loss rates peaked just after both glaciers underwent rapid flow accelerations, with peak thinning rates reaching  $\sim 90$  m yr $^{-1}$ . Increased longitudinal stretching accounts for nearly all the measured thinning, as shown by a volume continuity analysis.

Assuming the density of the volume loss is that of ice (917 kg m $^{-3}$ ), the five-year average contribution to sea level was  $\sim 0.10 \pm 0.02$  mm yr $^{-1}$  from the coastal portions alone, and  $\sim 0.31 \pm 0.07$  mm yr $^{-1}$  from the catchments as a whole. These estimates, from just two glaciers, are a significant fraction of the estimated total Greenland contribution to sea level rise of  $\sim 0.57$  mm yr $^{-1}$  (*Rignot and Kanagaratnam*, 2006), and confirm that changes in Southeast Greenland are the dominant source of recent accelerations in mass loss from the ice sheet (*Velicogna and Wahr*, 2006).

In addition to the effect on sea level, we expect the rapid rates of volume loss will have two other important impacts. One is to cause a rapid elastic adjustment of the lithosphere which should be detectable by geodetic methods (*Khan et al.*, 2007). The second effect is ongoing changes in the flow dynamics of Kangerdlugssuaq and Helheim glaciers due to changes in glacier geometry, which should be detectable with ongoing monitoring of their flow behavior.

## Chapter 6

### CONCLUSIONS

#### 6.1 Summary

Recent studies have shown that outlet glaciers of the Greenland and Antarctic ice sheets can undergo rapid and sustained changes in flow speed, with potentially important impacts on ice sheet mass balance and sea level rise. Many of these discoveries are new, so an important first step is mapping the spatial extent of the changes (*Which glaciers are affected?*), determining the timing of the changes (*When did glaciers start to change?*), and quantifying the types and rates of change (*What are the changes in speed, geometry, and mass?*). The logistic challenge of conducting field measurements in the polar regions means satellite remote sensing plays a key role in addressing these questions.

In this study, we assess the quality of ASTER satellite image products used to map changes in glacier dynamics. ASTER is one of the few satellite sensors that can image the high latitudes at high-resolution, making it ideal for producing sequential maps of velocity and elevation over remote areas. We compared overlapping measurements of ice velocity and elevation for Helheim Glacier, East Greenland, obtained from field-based GPS surveys and satellite image analysis. These tests are the first direct validation of remote sensing techniques widely applied in glaciology. Our results show that the satellite image products are generally of very good quality. ASTER-derived velocities were within 6 – 17% of observed velocities, and ASTER elevations are within 13.31 – 23.13 m of those measured with high-precision GPS. Results are optimized when the velocities are gridded to 150 m, and the DEMs are smoothed to 150 m.

ASTER imagery has many specifications that make it ideal for glaciology. There are also several ways to optimize results with ASTER products. Sequential images selected for velocity derivation should be cloud-free, with similar illumination characteristics, pointing angles, and snow cover. The time interval between these two images is dependent on the glacier flow speed; the features must be displaced more than the measure-

ment uncertainties, but not so long that features are distorted beyond recognition. Further consideration should be taken when choosing parameters in the cross-correlation routine.

ASTER DEMs provide a good representation of the glacier surface, but can contain systematic biases, and correction for these biases is necessary before quantifying surface elevation changes over glacier surfaces. We check for biases on all image pairs by comparing elevations over static bedrock features in sample  $5 \times 5$  km boxes. GPS elevations may not match well with ASTER DEMs due to geolocation errors in the ASTER products.

Outlet glaciers flowing through the Transantarctic Mountains into the Ross Embayment drain  $\sim 12\%$  of the entire Antarctic Ice Sheet, or a sea level equivalent of  $0.114 \pm 0.001$  mm yr $^{-1}$ . The remote sensing techniques described in Chapter 2 were applied to four of the largest glaciers in this part of East Antarctica: David, Mulock, Byrd and Nimrod glaciers. David Glacier and Nimrod Glacier maintained steady flow speeds from 2001 – 2006. In contrast, Mulock and Byrd glaciers appear to have accelerated in the past 2 – 3 years. Byrd Glacier, in particular, underwent significant changes in its flow structure, accelerating  $\sim 100$  m yr $^{-1}$  along most of its trunk. Archival field measurements allow the remote sensing observations to be placed in a longer-term context. Flow speeds of David and Nimrod glaciers show no change since 1990 and 1960, respectively. The recent accelerations of Mulock and Byrd glaciers are anomalous in the context of 45 year records.

Force balance results show that basal drag is the main control on fast flow of the EAIS glaciers. Lateral drag and longitudinal compression provide additional resistance at varying magnitudes depending on the geometry of the glacier. On Byrd Glacier, where flow speeds have changed in recent years, both longitudinal stress gradients and basal drag have decreased over the same time period.

Mass balance calculations indicate small positive balances for David ( $2.41 \pm 1.31$  Gt yr $^{-1}$ ), Mulock ( $1.91 \pm 0.84$  Gt yr $^{-1}$ ), and Nimrod ( $0.88 \pm 0.39$  Gt yr $^{-1}$ ) glaciers. Similar calculations yield a large positive imbalance for Byrd Glacier ( $22.32 \pm 1.72$  Gt yr $^{-1}$ ). Given that Byrd Glacier maintained a constant flow speed from 1960 – 2005, and a con-

stant surface elevation from 2002 – 2007, we conclude that the calculated mass imbalance is not real. Instead, we argue that the imbalance results from over-estimates in catchment-wide accumulation rate, derived from compiled data sources.

East Greenland outlet glaciers show a latitudinal change in dynamics, probably as a response to recent climate changes. Glaciers in southeast Greenland are changing rapidly, while glaciers north of 70°N appear to be stable. Daugaard Jensen Glacier and its neighboring glaciers are not undergoing any large scale changes in flow dynamics, according to a comparison of recent velocity observations with field measurements from the 1960s. Their calving front positions have also been stable for the past 40 – 50 years. A small negative balance for Daugaard Jensen Glacier ( $-3.8 \pm 2.5 \text{ km yr}^{-1}$ ) might be the result of overestimating the catchment-wide accumulation rate. Force balance results reveal that minimal resistance comes from shearing at the valley walls, but instead is generated from longitudinal compression and basal drag.

Kangerdlugssuaq and Helheim glaciers in southeast Greenland have undergone rapid thinning, terminus retreat and acceleration in the past few years. Our results indicate that up to  $\sim 10\%$  of global sea level rise over the period 2001 – 2006 was contributed by these two glaciers, with the volume loss being driven by dynamic thinning and loss of glacier tongues. These rapid changes highlight the sensitivity of tidewater glaciers to climate thresholds, and challenge the conventional glaciological theory that ice sheets adjust very slowly to external forcings.

## 6.2 Implications and Recommendations for Future Work

Sea level projections do not take into account the dynamic effect of outlet glaciers. Instead, the contribution of ice sheets to sea level rise is based on varying accumulation and surface melt parameters in different climates. However, there is evidence that ice sheet disintegration is driven by highly nonlinear processes and feedbacks. Following the Last Glacial Maximum, when both ice sheets were at least twice as large in area and volume as they are today (Clark and Mix, 2004; Fleming and Lambeck, 2004), a rapid rate of sea level rise (at an average rate of  $10 \text{ mm yr}^{-1}$ ) coincided with warming temperatures.

The majority of mass loss from the ice sheets was through large, fast flowing ice streams and outlet glaciers (e.g. Hudson Strait Ice Stream). Ice flux through the Hudson Strait Ice Stream may have cooled the water in the North Atlantic enough to alter ocean circulation and produce a rapid  $\sim 4^{\circ}\text{C}$  air temperature shift (*Andrews and Barber, 2002*). The characteristics of past ice sheet disintegrations emphasize the short time-scales at which ice sheets can adjust to climate, and the effect that large freshwater fluxes have on our climate system. Thus, it is important that we quantify and understand current changes in ice sheet outlet glaciers.

Several recommendations for future work are made on the basis of results described in this thesis. Continued monitoring of outlet glaciers by remote sensing is a priority. This work should be coupled with detailed field measurement programs on selected outlet glaciers. In particular, we need to gain a better understanding of the mechanisms driving large changes in flow speed, which probably include the interplay between surface melt-water hydrology and subglacial lubrication, and the role of force balance perturbations initiated near calving fronts. Accurate force balance analysis requires better and more complete coverage of ice thicknesses than are currently available. A final recommendation relates to mass balance estimates and is for improved catchment-scale accumulation models. Direct field measurements of accumulation distribution will help, but much can also be gained through improved modelling of snow properties and the effect of snow properties with satellite-based measurements.

## REFERENCES

- Abdalati, W., and K. Steffen (2001), Greenland Ice Sheet melt extent: 1979–1999, *Journal of Geophysical Research*, 106(D24), 33,983–33,988.
- Abdalati, W., W. Krabill, E. Frederick, S. Manizade, C. Martin, J. Sonntag, R. Swift, R. Thomas, W. Wright, and J. Yungel (2001), Outlet glacier and margin elevation changes: Near-coastal thinning of the Greenland Ice Sheet, *Journal of Geophysical Research*, 106(D24), 33,729–33,742.
- Alley, R., and I. Whillans (1991), Changes in the West Antarctic Ice Sheet, *Science*, 254, 959–963.
- Alley, R., P. Clark, P. Huybrechts, and I. Joughin (2005), Ice-sheet and sea-level changes, *Science*, 310(5747), 456–460.
- Alley, R., S. Anandakrishnan, T. Dupont, B. Parizek, and D. Pollard (2007), Effect of sedimentation on ice-sheet grounding-line stability, *Science*, 315(5820), 1838–1843.
- Andrews, J. T., and D. C. Barber (2002), Dansgaard-Oeschger events: Is there a signal off the Hudson Strait Ice Stream?, *Quaternary Science Reviews*, 21, 443–454.
- Aniya, M. (1999), Recent glacier variations of the Hielos Patagonicos, South America, and their contribution to sea-level change, *Arctic, Antarctic, and Alpine Research*, 31(2), 165–173.
- Aniya, M., H. Sato, R. Naruse, P. Skvarca, and G. Casassa (1997), Recent glacier variations in the Southern Patagonia Icefield, South America, *Arctic and Alpine Research*, 29(1), 1–12.
- Arendt, A. A., K. A. Echelmeyer, W. D. Harrison, C. S. Lingle, and V. B. Valentine (2002), Rapid wastage of Alaska glaciers and their contribution to rising sea level, *Science*, 297(5580), 382–386.
- Arthern, R., D. Winebrenner, and D. Vaughan (2006), Antarctic snow accumulation mapped using polarization of 4.3-cm wavelength microwave emission, *Journal of Geophysical Research*, 111(D06107), doi:10.1029/2004JD005,667.
- Bales, R., J. McConnell, E. Mosley-Thompson, and B. Csatho (2001), Accumulation over the Greenland Ice Sheet from historical and recent records, *Journal of Geophysical Research*, 106(D4), 33,813–33,826.
- Bamber, J., S. Ekholm, and W. Krabill (2001), A new, high-resolution digital elevation model of Greenland fully validated with airborne laser altimeter data, *Journal of Geophysical Research*, 106(B4), 6733–6746.
- Bamber, J. L., D. G. Vaughan, and I. Joughin (2000), Widespread complex flow in the interior of the Antarctic Ice Sheet, *Science*, 287, 1248–1251.
- Benn, D. I., C. R. Warren, and R. H. Mottram (2007), Calving processes and the dynamics of calving glaciers, *Earth Science Reviews*, 82, 143–179.

- Bentley, C. (1987), Antarctic Ice Streams: A review, *Journal of Geophysical Research*, 92(8843–8868).
- Berthier, E., Y. Arnaud, D. Baratoux, C. Vincent, and F. Rémy (2004), Recent rapid thinning of the “Mer de Glace” glacier derived from satellite optical images, *Geophysical Research Letters*, 31(L17401), doi:10.1029/2004GL020,706.
- Berthier, E., H. Vadon, D. Baratoux, Y. Arnaud, C. Vincent, K. Feigl, F. Remy, and B. Legresy (2005), Surface motion of mountain glaciers derived from satellite optical imagery, *Remote Sensing of Environment*, 95(1), 14–28.
- Berthier, E., Y. Arnaud, R. Kumar, S. Ahmad, P. Wagnon, and P. Chevallier (2007), Remote sensing estimates of glacier mass balances in the Himachal Pradesh (Western Himalaya, India), *Remote Sensing of Environment*, 108(3), 327–338.
- Bindoff, N., J. Willebrand, V. Artale, A. Cazenave, J. Gregory, S. Gulev, K. Hanawa, C. Le Quéré, S. Levitus, Y. Nojiri, C. Shum, L. Talley, and A. Unnikrishnan (2007), *Observations: Oceanic Climate Change and Sea Level*, Climate Change 2007: The Physical Science Basis. Contribution of Working Group I to the Fourth Assessment Report of the Intergovernmental Panel on Climate Change, Cambridge University Press, Cambridge, UK.
- Bindschadler, R. A., and T. Scambos (1991), Satellite-image-derived velocity field of an Antarctic Ice Stream, *Science*, 252, 242–246.
- Bindschadler, R. A., M. A. King, R. B. Alley, S. Anandakrishnan, and L. Padman (2003), Tidally controlled stick-slip discharge of a West Antarctic Ice Stream, *Science*, 301(5636), 1087–1089.
- Box, J. (2002), Survey of Greenland instrumental temperature records: 1873–2001, *International Journal of Climatology*, 22(15), 1829–1847.
- Box, J. E., D. H. Bromwich, B. A. Veenhuis, L. S. Bai, J. C. Stroeve, J. C. Rogers, K. Steffen, T. Haran, and S. H. Wang (2006), Greenland ice sheet surface mass balance variability (1988–2004) from calibrated Polar MM5 output, *Journal of Climate*, 19(12), 2783–2800.
- Brecher, H. (1982), Photographic determination of surface velocities and elevations on Byrd Glacier, *Antarctic Journal of the United States*, 17(5), 79–81.
- Budd, W. F. (1970), The longitudinal stress and strain-rate gradients in ice mass, *Journal of Glaciology*, 9, 19–27.
- Cazenave, A., and R. S. Nerem (2004), Present-day sea level change observation and causes, *Reviews of Geophysics*, 42, 3001–3021.
- Chapman, W. L., and J. Walsh (2007), A synthesis of Antarctic temperatures, *Journal of Climate*, 20, 4096–4117.
- Chen, J. L., C. R. Wilson, and B. D. Tapley (2006), Satellite gravity measurements confirm accelerated melting of Greenland Ice Sheet, *Science*, 313, 1958–1960.

- Church, J. A., et al. (2001), *Climate Change 2001: The Scientific Basis, IPCC 2001 Report*, chap. Changes in sea level, pp. 359–405, Cambridge: Cambridge University Press.
- Clark, P., and A. C. Mix (2004), Ice sheets and sea level of the Last Glacial Maximum, *Quaternary Science Reviews*, 21(1–3), 1–7.
- Comiso, J. (2000), Variability and trends in Antarctic surface temperatures from in situ and satellite infrared measurements, *Journal of Climate*, 13, 1674–1696.
- Cooper, A., N. McIntyre, and G. d. Q. Robin (1982), Driving stresses in the Antarctic Ice Sheet, *Annals of Glaciology*, 3, 59–63.
- Davis, C. H., Y. Li, J. R. McConnell, M. M. Frey, and E. Hanna (2005), Snowfall-driven growth in East Antarctic Ice Sheet mitigates recent sea-level rise, *Science*, 308, 1,898–1,901.
- de Angelis, H., and P. Skvarca (2003), Glacier Surge after Ice Shelf Collapse, *Science*, 299(1560–1562).
- Dowdeswell, J., R. Whittington, and R. Hodgkins (1992), The sizes, frequencies, and free-boards of East Greenland icebergs observed using ship radar and sextant, *Journal of Geophysical Research*, 97(C3), 3515–3528.
- Drewry, D. (1983), *Antarctica: glaciological and geophysical folio*, University of Cambridge, Scott Polar Research Institute.
- Dupont, T., and R. Alley (2005), Assessment of the importance of ice-shelf buttressing to ice-sheet flow, *Geophysical Research Letters*, 32(L04503), doi:10.1029/2004GL022,024.
- Dupont, T. K. (2004), Abrupt changes in ice shelves and ice streams: model studies, Ph.D. thesis, Pennsylvania State University.
- Dwyer, J. (1995), Mapping tide-water glacier dynamics in East Greenland using Landsat data, *Journal of Glaciology*, 41, 584–595.
- Echelmeyer, K., and W. Harrison (1990), Jakobshavn Isbræ, West Greenland: seasonal variations in velocity—or lack thereof, *Journal of Glaciology*, 36(122), 82–88.
- Ehlers, M., and R. Welch (1987), Stereocorrelation of Landsat TM images, *Photogrammetric Engineering and Remote Sensing*, 53, 1231–1237.
- Eldhuset, K., P. Andersen, S. Hauge, E. Isaksson, and D. Weydahl (2003), ERS tandem In-SAR processing for DEM generation, glacier motion estimation and coherence analysis on Svalbard, *International Journal of Remote Sensing*, 24(7), 1415–1437.
- Elósegui, P., J. L. Davis, J. M. Johansson, and I. Shapiro (1996), Detection of transient motions with the Global Positioning System, *Journal of Geophysical Research*, 101(B5), 11,249–11,262.
- Elósegui, P., J. L. Davis, D. Oberlander, R. Baena, and G. Ekström (2006), Accuracy of high-rate GPS for seismology, *Geophysical Research Letters*, 33(L11308), doi:10.1029/2006GL026,065.

- Ferrigno, J. G., B. K. Lucchitta, K. F. Mullins, A. L. Allison, R. J. Alen, and W. G. Gould (1993), Velocity measurements and changes in position of Thwaites Glacier/iceberg tongue from aerial photography, Landsat images and NOAA AVHRR data, *Annals of Glaciology*, 17, 239–244.
- Fleming, K., and K. Lambeck (2004), Constraints on the Greenland Ice Sheet since the Last Glacial Maximum from sea-level observations and glacial rebound models, *Quaternary Science Reviews*, 23, 1053–1077.
- Frezzotti, M. (1993), Glaciological study in Terra Nova Bay, Antarctica, inferred from remote sensing analysis, *Annals of Glaciology*, 17, 63–71.
- Frezzotti, M., A. Capra, and L. Vittuari (1998), Comparison between glacier ice velocities inferred from GPS and sequential satellite images, *Annals of Glaciology*, 27, 54–60.
- Fujisada, H., G. B. Bailey, G. G. Kelly, S. Hara, and M. J. Abrams (2005), ASTER DEM performance, *IEEE Transactions on Geoscience and Remote Sensing*, 43(12), 2,707–2,714.
- Gille, S. T. (2002), Warming of the Southern Ocean Since the 1950s, *Science*, 295(5558), 1,275–1,277.
- Giovinetto, M., and H. Zwally (2000), Spatial distribution of net surface accumulation on the Antarctic ice sheet, *Annals of Glaciology*, 31, 171–178.
- Gogineni, S., D. Tammana, D. Braaten, C. Leuschen, T. Akins, J. Legarsky, P. Kanagaratnam, J. Stiles, C. Allen, and K. Jezek (2001), Coherent radar ice thickness measurements over the Greenland ice sheet, *Journal of Geophysical Research*, 106(D24), 33,761–33,772.
- Grabmeier, K., T. A. M., and T. H. Verstappen (1998), Stereo mapping with SPOT, *ITC Journal*, 2, 149–154.
- Graf, W. L. (1970), The geomorphology of the glacial valley cross section, *Arctic and Alpine Research*, 2(4), 303–312.
- Gregory, J., P. Huybrechts, and S. Raper (2004), Threatened loss of the Greenland ice-sheet, *Nature*, 428(616), 257–267.
- Hamilton, G., L. Stearns, P. Elósegui, J. Davis, and M. Langer (submitted), Tidal modulation of ice flow on kangerdlugssuaq glacier, east greenland, *Geophysical Research Letters*.
- Hamilton, G. S., and I. M. Whillans (2002), Local rates of ice-sheet thickness change in Greenland, *Annals of Glaciology*, 35(1), 79–83.
- Hanna, E., P. Huybrechts, I. Janssens, J. Cappelen, K. Steffen, and A. Stephens (2005), Runoff and mass balance of the Greenland Ice Sheet: 1958–2003, *Journal of Geophysical Research*, 110(D13108), doi:10.1029/2004JD005,641.
- Hooke, R. (1981), Flow law for polycrystalline ice in glaciers: comparison of theoretical predictions, laboratory data, and field measurements, *Reviews of Geophysics and Space Physics*, 19(4), 664–672.

- Hooke, R. (2005), *Principles of Glacier Mechanics*, 2nd edition ed., 429 pp., Cambridge University Press, Cambridge, UK.
- Howat, I. M., I. Joughin, S. Tulaczyk, and S. Gogineni (2005), Rapid retreat and acceleration of Helheim Glacier, East Greenland, *Geophysical Research Letters*, 32(L22502), doi:10.1029/2005GL024,737.
- Hughes, T. J. (1979), Byrd Glacier, *Antarctic Journal of the United States*, 14(5), 88–91.
- Hughes, T. J. (1986), The Jakobshavn effect, *Geophysical Research Letters*, 13(1), 46–48.
- Humbert, A., R. Greve, and K. Hutter (2005), Parameter sensitivity studies for the ice flow of the Ross Ice Shelf, Antarctica, *Journal of Geophysical Research*, 10(10.1029).
- Huybrechts, P., and J. de Wolde (1999), The dynamic response of the Greenland and Antarctic ice sheets to multiple-century climatic warming, *Journal of Climate*, 12(8), 2169–2188.
- Jacobs, S. (2006), Observations of change in the Southern Ocean, *Philosophical Transactions of the Royal Society A: Mathematical, Physical and Engineering Sciences*, 364(1844), 1657–1681.
- Jacobs, S. S., C. F. Giulivi, and P. A. Mele (2002), Freshening of the Ross Sea During the Late 20th Century, *Science*, 297(5580), 386–389.
- Jezeck, K., H. Liu, Z. Zhao, and B. Li (1999), Improving a digital elevation model of Antarctica using radar remote sensing data and GIS techniques, *Polar Geography*, 23(3), 185–200.
- Johannessen, O. M., K. Khvorostovsky, M. W. Miles, and L. P. Bobylev (2005), Recent ice-sheet growth in the interior of Greenland, *Science*, 310(5750).
- Joughin, I., L. Gray, R. Bindschadler, S. Price, D. Morse, C. Hulbe, K. Mattar, and C. Werner (1999), Tributaries of West Antarctic Ice Streams Revealed by RADARSAT Interferometry, *Science*, 286(5438).
- Joughin, I., E. Rignot, C. Rosanova, B. Lucchitta, and J. Bohlander (2003), Timing of Recent Accelerations of Pine Island Glacier, Antarctica, *Geophysical Research Letters*, 30(13), 39–41.
- Joughin, I., W. Abdalati, and M. Fahnestock (2004), Large fluctuations in speed on Greenland's Jakobshavn Isbræ glacier, *Nature*, 432, 608–610.
- Kääb, A. (2002), Monitoring high-mountain terrain deformation from air- and spaceborne optical data: Examples using digital aerial imagery and ASTER data, *ISPRS Journal of Photogrammetry and Remote Sensing*, 57(1 – 2), 39–52.
- Kääb, A., C. Huggel, F. Paul, R. Wessels, B. Raup, H. Kieffer, and J. Kargel (2002), Glacier monitoring from STER imagery: accuracy and applications, *Proceedings of EARSeL LISSIG-Workshop Observing our Cryosphere from Space*, 43.

- Kenneally, J. P., and T. J. Hughes (2004), Basal melting along the floating part of Byrd Glacier, *Antarctic Science*, 16(3), 355–358.
- Khan, S. A., J. Wahr, L. A. Stearns, G. S. Hamilton, T. van Dam, K. Larson, and O. Francis (2007), Elastic uplift in southeast Greenland due to rapid ice mass loss, *Geophysical Research Letters*, *in press*.
- König, M., J. Winther, and E. Isaksson (2001), Measuring snow and glacier ice properties from satellite, *Reviews of Geophysics*, 39(1), 1–27.
- Krabill, W., W. Abdalati, E. Frederick, S. Manizade, S. Manizade, J. Sonntag, R. Swift, W. Wright, and J. Yungel (2000), Greenland ice sheet: High elevation balance and peripheral thinning, *Science*, 289(428–430).
- Krabill, W., E. Hanna, P. Huybrechts, W. Abdalati, J. Cappelen, B. Csatho, E. Frederick, S. Manizade, C. Martin, and J. Sonntag (2004), Greenland Ice Sheet: Increased coastal thinning, *Geophysical Research Letters*, 31, 24.
- Kurtz, D., and D. Bromwich (1983), Satellite observed behavior of the Terra Nova Bay Polynya, *Journal of Geophysical Research*, 88(C14), 9,717–9,722.
- Lemke, P., J. Ren, R. Alley, I. Allison, J. Carrasco, G. Flato, Y. Fujii, G. Kaser, P. Mote, R. Thomas, and T. Zhang (2007), *Observations: changes in snow, ice and frozen ground*, Climate Change 2007: The Physical Science Basis. Contribution of Working Group I to the Fourth Assessment Report of the Intergovernmental Panel on Climate Change, Cambridge University Press, Cambridge.
- Levitus, S., J. Antonov, and T. Boyer (2005), Warming of the world ocean, 1955–2003, *Geophysical Research Letters*, 32.
- Lichten, S. M., and J. S. Border (1987), Strategies for high-precision global positioning system orbit determination, *Journal of Geophysical Research*, 92, 12,751–12,762.
- Liu, H., K. Jezek, and B. Li (1999), Development of an Antarctic digital elevation model by integrating cartographic and remotely sensed data: a geographic information system based approach, *Journal of Geophysical Research*, 104(23), 23,199–23,213.
- Lucchitta, B. K., and H. M. Ferguson (1986), Antarctica: measuring glacier velocity from satellite images, *Science*, 234, 1105–1108.
- Luckman, A., T. Murray, R. de Lange, and E. Hanna (2006), Rapid and synchronous ice-dynamic changes in East Greenland, *Geophysical Research Letters*, 33, L03,503.
- Luthcke, S. B., H. J. Zwally, W. Abdalati, D. D. Rowlands, R. D. Ray, R. S. Nerem, F. G. Lemoine, J. J. McCarthy, and D. S. Chinn (2006), Recent Greenland ice mass loss by drainage system from satellite gravity observations, *Science*, 314, 1,286 –1,289.
- Lythe, M., D. G. Vaughan, and the BEDMAP consortium (2001), BEDMAP: A new ice thickness and subglacial topographic model of Antarctica, *Journal of Geophysical Research*, 106(B6), 11,335–11,352.

- Macayeal, D. (1989), Ice-shelf response to ice-stream discharge fluctuations: III. The effects of ice-stream imbalance on the Ross Ice Shelf, Antarctica, *Journal of Glaciology*, 35(119), 38–42.
- Mader, G. (1992), Rapid static and kinematic Global Positioning System solutions using the ambiguity function technique, *Journal of Geophysical Research*, 97(B3), 3,271–3,283.
- Magand, O., C. Genthon, M. Fily, G. Krinner, G. Picard, M. Frezzotti, and A. Ekyakin (2007), An up-to-date quality-controlled surface mass balance data set for the 90–180°E Antarctica sector and 1950–2005 period, *Journal of Geophysical Research*, 112(D12).
- Maule, C., M. Purucker, N. Olsen, and K. Mosegaard (2005), Heat flux anomalies in Antarctica revealed by satellite magnetic data, *Science*, 309(5733), 464–467.
- McGranahan, G., D. Balk, and B. Anderson (2007), The rising tide: assessing the risks of climate change and human settlements in low elevation coastal zones, *Environment and Urbanization*, 19(1), 17–37.
- Meier, M., and A. Post (1987), Fast tidewater glaciers, *Journal of Geophysical Research*, 92(B9), 9,051–9,058.
- Meier, M. F. (1997), The iceberg discharge process: observations and inferences drawn from the study of Columbia Glacier, in *BPRC Report*, edited by C. J. van der Veen, 15, pp. 109–114, Byrd Polar Research Center, BPRC Report.
- Mercer, J. H. (1978), West Antarctic Ice Sheet and CO<sub>2</sub> greenhouse effect: A threat of disaster, *Nature*, 271, 321–325.
- Motyka, R., M. Truffer, E. Kuriger, and A. Bucki (2006), Rapid erosion of soft sediments by tidewater glacier advance: Taku Glacier, Alaska, USA, *Geophysical Research Letters*, 33(24), L24,504.
- Naruse, R., M. Aniya, P. Skvarca, and G. Casassa (1995), Recent variations of calving glaciers in Patagonia, South America, revealed by ground surveys, satellite-data analyses and numerical experiments, *Annals of Glaciology*, 21, 297–303.
- Nick, F. M., C. J. van der Veen, and J. Oerlemans (2007), Controls on advance of tidewater glaciers: Results from numerical modeling applied to Columbia Glacier, *Journal of Geophysical Research*, 112(F3).
- Ó Cofaigh, C., J. Dowdeswell, and G. H. (2001), Holocene glacimarine sedimentation, inner Scoresby Sund, East Greenland: the influence of fast-flowing ice-sheet outlet glaciers, *Marine Geology*, 175, 103–129.
- Olesen, O., and N. Reeh (1969), Preliminary report of glacier observations in Nordvestfjord, East Greenland, *Grønlands Geologiske Undersøgelse Rapport*, 21.
- O’Neel, S., K. A. Echelmeyer, and R. J. Motyka (2001), LeConte Glacier, Alaska, USA, *Journal of Glaciology*, 47(159), 567–578.

- Parizek, B. R., and R. B. Alley (2004), Implications of increased Greenland surface melt under global-warming scenarios:ice-sheet simulations, *Quaternary Science Reviews*, 23, 1013–1027.
- Paul, F., C. Huggel, and A. Kääb (2004), Combining satellite multispectral image data and a digital elevation model for mapping debris-covered glaciers, *Remote Sensing of Environment*, 89, 510–518.
- Payne, A. J., A. Vieli, A. P. Shepherd, D. J. Wingham, and E. Rignot (2004), Recent dramatic thinning of largest West Antarctic ice stream triggered by oceans, *Geophysical Research Letters*, 31(L23401), doi:10.1029/2004GL021,284.
- Pfeffer, W. (2007), A simple mechanism for irreversible tidewater retreat, *Journal of Geophysical Research*, 112(F03S25), doi:10.1029/2006JF000,590.
- Pfeffer, W., J. Cohn, M. Meier, and R. M. Krimmel (2000), Accelerated retreat of Columbia Glacier, Alaska, *Eos Trans. AGU*, 81(48), 577–584.
- Post, A. (1975), Preliminary hydrology and historic terminal changes of Columbia Glacier, *U.S. Geol. Surv. Hydrol. Invest. Atlas*.
- Price, S., and I. Whillans (1998), Delineation of a catchment boundary using velocity and elevation measurements, *Annals of Glaciology*, 27, 140–144.
- Price, S., R. Bindschadler, C. Hulbe, and D. Blankenship (2002), Force balance along an inland tributary and onset to Ice Stream D, West Antarctica, *Journal of Glaciology*, 48(160), 20–30.
- Pritchard, H. D., and D. G. Vaughan (2007), Widespread acceleration of tidewater glaciers on the Antarctic Peninsula, *Journal of Geophysical Research*, 112(F03S29), doi:10.1029/2006JF000,597.
- Ramillien, G., A. Lombard, A. Cazenave, E. R. Ivins, M. Llubes, F. Remy, and R. Biancale (2006), Interannual variations of the mass balance of the Antarctica and Greenland ice sheets from GRACE, *Global and Planetary Change*, 53(3), 198–208.
- Rayner, N. A., P. Brohan, D. Parker, C. Folland, J. Kennedy, M. Vanicek, T. Ansell, and S. Tett (2006), Improved analyses of changes and uncertainties in sea surface temperature measured in situ since the mid-nineteenth Century: The HadSST2 dataset, *Journal of Climate*, 19(3), 446–469.
- Reeh, N., and O. Olesen (1986), Velocity measurements on Daugaard-Jensen Glatcher, Scoresby Sund, East Greenland, *Annals of Glaciology*, 8, 146–150.
- Retzlaff, R., N. Lord, and C. Bentley (1993), Airborne-radar studies: Ice Streams A, B and C, West Antarctica, *Journal of Glaciology*, 39(133), 495–506.
- Reusch, D., and T. J. Hughes (2003), Surface "waves" on Byrd Glacier, Antarctica, *Antarctic Science*, 15(04), 547–555.
- Rignot, E. (2001), Evidence for rapid retreat and mass loss of Thwaites Glacier, West Antarctica, *Journal of Glaciology*, 47(157), 213–222.

- Rignot, E. (2002), Mass balance of East Antarctic glaciers and ice shelves from satellite data, *Annals of Glaciology*, 34, 217–227.
- Rignot, E., and S. S. Jacobs (2002), Rapid bottom melting widespread near Antarctic Ice Sheet grounding lines, *Science*, 296(5575), 2,020–2,023.
- Rignot, E., and P. Kanagaratnam (2006), Changes in the velocity structure of the Greenland Ice Sheet, *Science*, 311, 986–990.
- Rignot, E., and R. Thomas (2002), Mass balance of polar ice sheets, *Science*, 297, 1,502–1,507.
- Rignot, E., S. Gogineni, I. Joughin, and W. Krabill (2001), Contribution to the glaciology of northern Greenland from satellite radar interferometry, *Journal of Geophysical Research*, 106(D24), 34,007–34,020.
- Rignot, E., A. Rivera, and G. Casassa (2003), Contribution of the Patagonia icefields of South America to sea level rise, *Science*, 302(5644), 434–437.
- Rignot, E., D. Braaten, S. P. Gogineni, W. Krabill, and J. R. McConnell (2004), Rapid ice discharge from southeast Greenland glaciers, *Geophysical Research Letters*, 31(L10401), doi:10.1029/2004GL019,474.
- Rintoul, S. R. (2007), Rapid freshening of Antarctic Bottom Water formed in the Indian and Pacific oceans, *Geophysical Research Letters*, 34(L06606), doi:10.1029/2006GL028,550.
- Rivera, A., G. Casassa, J. Bamber, and A. Kääb (2005), Ice-elevation changes of Glaciar Chico, southern Patagonia, using ASTER DEMs, aerial photographs and GPS data, *Journal of Glaciology*, 51(172), 105–112.
- Rott, H., W. Rack, P. Skvarca, and H. de Angelis (2002), Northern Larsen Ice Shelf, Antarctica: further retreat after collapse, *Annals of Glaciology*, 34, 277–282.
- Scambos, T., and M. A. Fahnestock (1998), Improving digital elevation models over ice sheets using AVHRR-based photoclinometry, *Journal of Glaciology*, 44(146), 97–103.
- Scambos, T., M. Dutkiewicz, J. Wilson, and R. Bindschadler (1992), Application of image cross-correlation to the measurement of glacier velocity using satellite image data., *Remote Sensing of Environment*, 42(3), 177–186.
- Scambos, T., C. Hulbe, M. A. Fahnestock, and J. Bohlander (2000), The link between climate warming and break-up of ice shelves in the Antarctic Peninsula, *Journal of Glaciology*, 46, 516–530.
- Scambos, T., J. Bohlander, C. Shuman, and P. Skvarca (2004), Glacier acceleration and thinning after ice shelf collapse in the Larsen B embayment, Antarctica, *Geophysical Research Letters*, 31(L18402), doi:10.1029/2004GL020,670.
- Schenk, T., B. Csatho, C. J. van der Veen, H. Brecher, Y. Ahn, and T. Yoon (2005), Registering imagery to ICESat data for measuring elevation changes on Byrd Glacier, Antarctica, *Geophysical Research Letters*, 32(L23S05), doi:10.1029/2005GL024,328.

- Scherer, R., A. Aldahan, S. Tulaczyk, G. Possnert, H. Engelhardt, and B. Kamb (1998), Pleistocene collapse of the West Antarctic Ice Sheet, *Science*, 281(5373), 82–85.
- Scofield, J. P., J. L. Fastook, and T. J. Hughes (1991), Evidence for a frozen bed, Byrd Glacier, Antarctica, *Journal of Geophysical Research*, 96(B7), 11,649–11,655.
- Serreze, M., M. Holland, and J. Stroeve (2007), Perspectives on the arctic's shrinking sea-ice cover, *Science*, 315(5818), 1,533–1,536.
- Shepherd, A., D. J. Wingham, J. Mansley, and H. Corr (2001), Inland thinning of Pine Island Glacier, West Antarctica, *Science*, 291(291), 862–864.
- Shepherd, A., D. Wingham, and E. Rignot (2004), Warm ocean is eroding West Antarctic Ice Sheet, *Geophysical Research Letters*, 31(23), 1–4.
- Shindell, D. T., and G. A. Schmidt (2004), Southern Hemisphere climate response to ozone changes and greenhouse gas increases, *Geophysical Research Letters*, 31(L18209), doi:10.1029/2004GL020,724.
- Sohn, H., K. Jezek, and C. van der Veen (1998), Jakobshavn Glacier, West Greenland: 30 years of spaceborne observations, *Geophysical Research Letters*, 25(14), 2699–2702.
- Stearns, L., and G. Hamilton (2005), A new velocity map for Byrd Glacier, East Antarctica, from sequential ASTER satellite imagery, *Annals of Glaciology*, 41, 71–76.
- Stearns, L., G. Hamilton, and N. Reeh (2005a), Multi-decadal record of ice dynamics on Daugaard Jensen Gletscher, East Greenland, from satellite imagery and terrestrial measurements, *Annals of Glaciology*, 42(1), 53–58.
- Stearns, L., K. Jezek, and C. van der Veen (2005b), Decadal-scale variations in ice flow along Whillans Ice Stream and its tributaries, West Antarctica, *Journal of Glaciology*, 51(172), 147–157.
- Stearns, L. A., and G. S. Hamilton (2007), Rapid volume loss from two east greenland outlet glaciers quantified using repeat stereo satellite imagery, *Geophysical Research Letters*, 34(L05503), doi:10.1029/2006GL028,982.
- Stevens, N., H. Garbeil, and P. Mouginis-Mark (2004), NASA EOS Terra ASTER- Volcanic topographic mapping and capability, *Remote Sensing of Environment*, 90(3), 405–414.
- Swithinbank, C. (1963), Ice Movement of valley glaciers flowing into the Ross Ice Shelf, Antarctica, *Science*, 141(3580), 523–525.
- Thomas, R. (2001), Program for Arctic Regional Climate Assessment(PARCA): Goals, key findings, and future directions: Mass balance of the Greenland ice sheet(PARCA), *Journal of geophysical research*, 106(d 24), 33,691–33,705.
- Thomas, R., W. Abdalati, T. L. Akins, B. M. Csatho, E. B. Frederick, S. P. Gogineni, W. B. Krabill, and S. S. Manizade (2000a), Substantial thinning of a major east Greenland outlet glacier, *Geophysical Research Letters*, 27(9), 1291–1295.

- Thomas, R., T. Akins, B. Csatho, M. Fahnestock, P. Gogineni, C. Kim, and J. Sonntag (2000b), Mass balance of the Greenland Ice Sheet at high elevations, *Science*, 289(5478), 426–428.
- Thomas, R., E. Frederick, W. Krabill, S. Manizade, and C. Martin (2006), Progressive increase in ice loss from Greenland, *Geophysical Research Letters*, 33(L10503), doi:10.1029/2006GL026,075.
- Thomas, R. H. (2004), Force-perturbation analysis of recent thinning and acceleration of Jakobshavn Isbrae, Greenland, *Journal of Glaciology*, 50(168), 57–66.
- Thomas, R. H., and C. Bentley (1978), A model for Holocene retreat of the West Antarctic Ice Sheet, *Quaternary Science Reviews*, 10, 150 – 170.
- Thomas, R. H., and D. R. MacAyeal (1982), Derived characteristics of the Ross Ice Shelf, *Journal of Glaciology*, 28(100), 397 – 412.
- Thomas, R. H., W. Abdalati, E. Frederick, W. B. Krabill, S. Manizade, and K. Steffen (2003), Investigation of surface melting and dynamic thinning on Jakobshavn Isbrae, Greenland, *Journal of Glaciology*, 49(165), 231–239.
- Toutin, T. (2002a), DEM from stereo Landsat 7 ETM+ data over high relief areas, *International Journal of Remote Sensing*, 23(10), 2,133–2,139.
- Toutin, T. (2002b), Three-dimensional topographic mapping with ASTER stereo data in rugged topography, *IEEE Transactions on Geoscience and Remote Sensing*, 40(10), 2,241–2,247.
- Van de Berg, W., M. van den Broeke, C. Reijmer, and E. van Meijgaard (2006), Reassessment of the Antarctic surface mass balance using calibrated output of a regional atmospheric climate model, *Journal of Geophysical Research*, 111(D11), doi:10.1029/2005JD006,495.
- Van der Veen, C. (1996), Tidewater calving, *Journal of Glaciology*, 42(141), 375–385.
- Van der Veen, C. J. (1999), *Fundamentals of Glacier Dynamics*, A.A. Balkema, Rotterdam, Netherlands.
- Van der Veen, C. J. (2002), Calving glaciers, *Progress in Physical Geography*, 26(1), 96.
- Van der Veen, C. J., and I. M. Whillans (1989), Force budget: I. Theory and numerical methods, *Journal of Glaciology*, 35(119), 53–60.
- Vaughan, D., J. Bamber, M. Giovinetto, J. Russell, and A. Cooper (1999), Reassessment of net surface mass balance in Antarctica, *Journal of Climate*, 12(4), 933–946.
- Velicogna, I., and J. Wahr (2006), Acceleration of Greenland ice mass loss in spring 2004, *Nature*, 443(7109), 329–331.
- Venteris, E. R. (1999), Rapid tidewater glacier retreat: a comparison between Columbia Glacier, Alaska and Patagonian calving glaciers, *Global and Planetary Change*, 22, 131–138.

- Vignon, F., Y. Arnaud, and G. Kaser (2003), Quantification of glacier volume change using topographic and ASTER DEMs, *Geoscience and Remote Sensing Symposium, 2003. IGARSS'03. Proceedings. 2003 IEEE International*, 4, 2,605–2,607.
- Warren, C. R., and M. Aniya (1999), The calving glaciers of southern South America, *Global and Planetary Change*, 22, 59–77.
- Weertman, J. (1974), Stability of the junction of an ice sheet and an ice shelf, *Journal of Glaciology*, 13, 3–11.
- Weidick, A. (1995), *Satellite image atlas of glaciers of the world: Greenland*, vol. 1386-C, United States Government Printing Office.
- Whillans, I. M., and Y. H. Tseng (1995), Automatic tracking of crevasses on satellite images, *Cold Regions Science and Technology*, 23(201 – 214).
- Whillans, I. M., and C. J. Van der Veen (1993), Patterns of calculated basal drag on Ice Streams B and C, Antarctica, *Journal of Glaciology*, 39(133), 437–447.
- Whillans, I. M., Y. H. Chen, C. J. Van der Veen, and T. J. Hughes (1989), Force budget: III. Application to the three-dimensional flow of Byrd Glacier, Antarctica, *Journal of Glaciology*, 35(119), 68–80.
- Wingham, D. J., A. Shepherd, A. Muir, and G. J. Marshall (2006), Mass balance of the Antarctic Ice Sheet, *Philosophical Transactions of the Royal Society A: Mathematical, Physical and Engineering Sciences*, 364(1844), 1,627–1,635.
- Wuite, J. (2006), Spatial and temporal dynamics of three East Antarctic outlet glaciers and their floating ice tongues, Ph.D. thesis, The Ohio State University.
- Yamaguchi, Y., A. B. Kahle, H. Tsu, T. Kawakami, and M. Pniel (1998), Overview of Advanced Spaceborne Thermal Emission and Reflection Radiometer (ASTER), *IEEE Transactions on Geoscience and Remote Sensing*, 36(4), 1,062–1,071.
- Yang, L. (2007), Greenland Ice Sheet change: surface climate variability and glacier dynamics, Ph.D. thesis, The Ohio State University.
- Zomer, R. (2002), Using satellite remote sensing for DEM extraction in complex mountainous terrain: landscape analysis of the Makalu Barun National Park of eastern Nepal, *International Journal of Remote Sensing*, 23(1), 125–143.
- Zwally, H., and M. Giovinetto (2001), Balance mass flux and ice velocity across the equilibrium line in drainage systems of Greenland, *Journal of Geophysical Research*, 106(D24), 33,717–33,728.
- Zwally, H. J., W. Abdalati, T. Herring, K. Larson, J. Saba, and K. Steffen (2002), Surface melt-induced acceleration of Greenland Ice-Sheet flow, *Science*, 297(5579), 218–222.
- Zwally, H. J., M. B. Giovinetto, J. Li, H. G. Cornejo, M. A. Beckley, A. C. Brenner, J. L. Saba, and D. Yi (2005), Mass changes of the Greenland and Antarctic ice sheets and shelves and contributions to sea-level rise: 1992–2002, *Journal of Glaciology*, 51(175), 509–527.

**APPENDIX**  
**SATELLITE IMAGE DETAILS**

Glacier	Image Date	Image Type	Scene ID
Helheim Glacier	08/25/2006	ASTER	00308252006141051
	08/30/2006	ASTER	00308302006142904

Table A.1. Images used in Chapter 2.

Glacier Name	Image Date	Image Type	Scene ID
David Glacier	01/17/2001	ASTER	00301172001212608
	10/14/2001	ASTER	00310142001213212
	02/06/2003	ASTER	00302062003212739
	12/30/2005	ASTER	00312302005211258
		ASTER	00312302005211307
	02/12/2006	ASTER	00302122006213736
Mulock Glacier	10/12/2001	ASTER	00310122001200720
	10/20/2001	ASTER	00310202001205606
	11/04/2001	ASTER	00311042001201226
	11/20/2001	ASTER	00311202001201202
	11/16/2002	ASTER	00311162002200231
	11/23/2002	ASTER	00311232002200859
	01/26/2003	ASTER	00301262003200856
	02/12/2004	ASTER	00302122004202043
	12/31/2005	ASTER	00312312005152543
		ASTER	00312312005201849
	10/15/2006	ASTER	00310152006201912
	03/05/2006	ASTER	00303052006201911
	03/08/2007	ASTER	00303082007202023
Byrd Glacier	02/22/1988	Landsat TM	lt4045119120088053
	02/08/1989	Landsat TM	lt4045119120089039
	01/29/1990	Landsat TM	lt4050118119090029
	01/29/2001	ASTER	00301292001201357
		ASTER	00301292001201406
	12/09/2001	ASTER	00312092001204213
		ASTER	00312092001204222
		ASTER	00312092001204231
	01/16/2002	ASTER	00301162002200419
		ASTER	00301162002200428
	12/08/2004	ASTER	00312082004190548
	12/10/2004	ASTER	00312102004185338
	12/05/2005	ASTER	00312052005194240
		ASTER	00312052005194249
	01/02/2006	ASTER	00301022006200650
	01/21/2007	ASTER	00301212007200804
		ASTER	00301212007200813
	01/28/2007	ASTER	00301282007201419
		ASTER	00301282007201428
Nimrod Glacier	12/01/2000	ASTER	00312012000185510
	01/28/2001	ASTER	00301282001193116
	11/21/2001	ASTER	00311212001191727
	11/30/2004	ASTER	00311302004181647
	12/22/2005	ASTER	00312222005184735
	12/15/2006	ASTER	00312152006181117

Table A.2. Images used in Chapter 3.

Glacier	Image Date	Image Type	Scene ID
Daugaard Jensen Glacier	07/26/1973	Landsat MSS	1249009007320790
	06/21/1991	Landsat TM	p231r095t19910621
	07/05/1999	Landsat ETM	p231r097fl19990705
	08/10/2000	ASTER	00308102000141146
	05/25/2001	ASTER	00305252001140639
	07/12/2001	ASTER	00307122001140515
	06/30/2002	ASTER	00306302002224721
	06/14/2003	ASTER	00306142003140936
	08/01/2003	ASTER	00308012003140829
	06/16/2004	ASTER	00306162004140912
	07/09/2004	ASTER	00307092004141509
		ASTER	00307092004141518
	06/12/2005	ASTER	00306122005140221
	07/21/2005	ASTER	00307212005140846
	06/08/2006	ASTER	00306082006135639
	07/29/2007	ASTER	00307292007135727
Charcot and Graah glaciers	07/26/1973	Landsat MSS	1249009007320790
	06/21/1991	Landsat TM	p231r095t19910621
	07/05/1999	Landsat ETM	p231r097fl19990705
	08/10/2000	ASTER	00308102000141138
	07/12/2001	ASTER	0030 7122001140506
	07/31/2002	ASTER	00307312002135837
	06/14/2003	ASTER	00306142003140936
	06/16/2004	ASTER	00306162004140912
	06/12/2005	ASTER	00306122005140221
	06/08/2006	ASTER	00306082006135630

Table A.3. Images used in Chapter 4.

Glacier	Image Date	Image Type	Scene ID
Helheim Glacier	09/06/1972	Landsat MSS	1250014007225090
	07/09/1986	Landsat MSS	5231014008619090
	09/06/1992	Landsat TM	p228r125t19920906
	07/08/2001	Landsat ETM	p233r0137t20010708
	08/02/2001	Landsat ETM	p232r0137t20010802
	06/20/2002	ASTER	00306202002234721
	07/07/2003	ASTER	00307072003141652
	08/08/2003	ASTER	00308082003141620
	06/23/2004	ASTER	00306232004141653
	07/18/2004	ASTER	00307182004141053
	08/03/2004	ASTER	00308032004142301
	06/19/2005	ASTER	00306192005141023
	07/12/2005	ASTER	00307122005141634
	08/29/2005	ASTER	00308292005141621
	08/25/2006	ASTER	00308252006141051
	08/30/2006	ASTER	00308302006142904
Kangerdlugssuaq Glacier	09/06/1972	Landsat MSS	1250014007225090
	07/11/1986	Landsat TM	5229012008619210
	06/21/1991	Landsat TM	p231r125t19910621
	07/16/2000	ASTER	00307162000141924
	07/03/2001	Landsat ETM	p230r0127p20010703
	07/12/2001	Landsat ETM	p229r0127p20010712
	07/12/2001	ASTER	00307122001140608
	07/29/2002	ASTER	00307292002141153
	06/14/2003	ASTER	00306142003141029
	06/30/2003	ASTER	00306302003141009
	08/01/2003	ASTER	00308012003140922
	06/16/2004	ASTER	00306162004141005
	06/25/2004	ASTER	00306252004140355
	06/21/2005	ASTER	00306212005135718
	08/31/2005	ASTER	00308312005140323
	06/08/2006	ASTER	00306082006135732
	09/03/2006	ASTER	00309032006140353

Table A.4. Images used in Chapter 5.

## **BIOGRAPHY OF THE AUTHOR**

Leigh Stearns was born in New York City, New York on May 24, 1977. She attended The Brearley School and graduated in 1995. She majored in geology, with a minor in environmental studies, at Carleton College, receiving her Bachelor's degree in 1999. She became interested in glaciology through her undergraduate thesis on "Water movement through the firm of Storglaciären, Sweden". She continued her glaciology research at The Ohio State University, where she graduated with a Master's degree in Geology in 2002. Her Master's thesis was titled "The dynamic state of Whillans Ice Stream, West Antarctica." She came to the University of Maine in 2002. Leigh is a candidate for the Doctor of Philosophy degree in Earth Sciences from the University of Maine in December, 2007.